Beyond Lipoxygenase: Studying the Initiation of Ferroptosis

&

On the Mechanism Behind α-Eleostearic Acid Autoxidation

By

Spencer Short

Thesis submitted to the University of Ottawa in partial fulfillment
of the requirements for the Master of Science degree in Chemistry

Department of Chemistry and Biomolecular Sciences

Faculty of Science

University of Ottawa

Abstract

Ferroptosis is a recently characterized cell death pathway associated with the iron-dependent accumulation of lipid hydroperoxides in phospholipid bilayers. The origin of these hydroperoxides has been an ongoing topic of debate and many researchers argue for a lipoxygenase (LOX) enzyme-controlled mechanism of initiation, given their known role as dioxygenases of polyunsaturated fatty acids (PUFAs). In response to this, our lab investigated the induction and inhibition of ferroptosis in human embryonic kidney (HEK-293) cells transfected to overexpress the three most prevalent LOX isoforms, 5-LOX, p12-LOX, and 15-LOX-1. These studies did not support a role for LOX in the execution of ferroptosis; LOX inhibition was not associated with ferroptosis suppression and in fact, anti-ferroptotic activity was directly tied to purported LOX inhibitors' ability to act as radical-trapping antioxidants (RTAs). We have investigated the effects of LOX inhibitors on ferroptosis in human fibrosarcoma (HT-1080) cells, the cell line in which ferroptosis was initially characterized, and mouse hippocampal neuronal (HT-22) cells, the cell line in which the closely related cell death modality oxytosis was characterized. In sum, our findings mirror those obtained in HEK-293 cells, and the effectiveness of an inhibitor is tied to its off-target RTA activity, not inhibition of LOX. Moreover, we observed suppression of ferroptosis via necrostatin-1 (Nec-1), a known receptor-interacting serine/threonine-protein kinase 1 (RIPK1) (and necroptosis) inhibitor. Herein, we show that Nec-1 is not an RTA and exerts its effects by a yet unknown mechanism which we investigate in a series of exploratory experiments.

Conjugated fatty acids – particularly α-ESA – have recently been reported to induce ferroptosis by an unclear mechanism. Theorizing this phenomenon was tied to the autoxidation of α-ESA's conjugated trienic unit, we aimed to investigate the kinetic and biological properties of natural α-ESA alongside a deuterated isotopologue. Herein, we report preliminary work to derive biologically relevant rate constants for addition and hydrogen-atom transfer (HAT) of α-ESA. Moreover, we report our progress towards the synthesis of a deuterated α-ESA which will facilitate future study alongside its natural counterpart.

Acknowledgements

First and foremost I would like to thank my supervisor Dr. Derek Pratt for taking me on as a student and mentoring me throughout my graduate work thus far. Over the past two years, your mentorship and guidance has helped shape my competency and effectiveness as a researcher. Your passion for research is inspiring, and pushes me to achieve higher degrees of craftsmanship in both labour and life.

I would like to extend a wholehearted thank you to all members, past and present, in the Pratt Group whom I have had the honour of working (and relaxing) with. Notably, I would like to thank Neill for our rigid morning workout routines, Mel for the wilderness retreats, Luke for (essentially) always coming for convenience store hotdogs, Dmitry for teaching me how to make Ukha, Jannik for eating bacon with me at 3am, Zijun for always being in the lab, as well as Omkar, Ron, Kareem, Jai-Fei, Demar, Anas, and any others I may have missed. I would also like to thank Mark Raycroft for his exceptional mentorship in-lab and Katie Shirley for her excellent co-research and co-presentation skills. Most of all, I want to thank Emily Shaefer for her above-and-beyond guidance throughout my graduate experience (and a lot of coffees). You have all helped make the lab a positive environment, for which I am very grateful. I couldn’t have done it without you guys.

I would also like to extend my thanks to the department. Countless students and professors alike have shaped my experience at UOttawa for the better (special thanks to the Barriault and Ben Groups).

A big thank you is also in order to my family and friends who have supported me throughout. Firstly, my dad for making himself available for endless talks and discussions about work and life, as well as my mom for her positivity and support as I continue to grow and learn. Also, Grandma Marie, Mike, Ken, Tara, Lee, Morgan, Alex (and Xander), Brendan, Dan, Eric (and family), Ewa and all others who listened and supported my efforts. Last but not least, I would extend my gratitude to Corina. Your endless support has helped me endure the past year, a year I hope is the first of many.

I couldn’t have done it alone, thank you all.

Statement of Originality

I hereby certify that all work described in this thesis is the original work of the author, with exception to work performed by collaborators, which has been fully acknowledged within the text. The work in this thesis draws upon a great deal of previously published research. Any published (or unpublished) work by others is cited and fully acknowledged within the references.

Spencer J Short

Table of Contents

List of Figures

List of Schemes

List of Tables

List of Abbreviations

AIBN	azobisisobutyronitrile
AMVN	2,2’-azobis(2,4-dimethylvaleronitrile)
ATP	adenosine triphosphate
BODIPY	4,4-difluoro-4-bora-3*a*,4*a*-diaza-*s*-indacene
BDE	bond dissociation energy
BHT	2,6-di-*tert*-butyl-4-methylphenol
C_{11}-BODIPY	an undecanoic acid-bound BODIPY
CV	cyclic voltammetry
d_4-α-ESA	8,8,15,15-d_4-α-ESA
DMAP	4-dimethylaminopyridine
α-ESA	α-eleostearic acid
β-ESA	β-eleostearic acid
ETC	electron transport chain
Fer-1	ferrostatin-1
GPx	glutathione peroxidase family
GPX4	glutathione peroxidase 4
GSH	glutathione
GSSG	glutathione disulfide
HAT	hydrogen atom transfer
HEK-293	human embryonic kidney
HT-1080	human fibrosarcoma
HT-22	mouse hippocampal neuronal
IC_{50}	median inhibitory concentration
In	initiator
IPA	isopropyl alcohol
k_{add}	propagation rate constant for addition
k_H	propagation rate constant for HAT
k_{inh}	inhibition rate constant

k_P	propagation rate constant
k_{perox}	propagation rate constant for peroxidation
KIE	kinetic isotope effect
LD_{50}	median lethal dose
Lip-1	liproxstatin-1
L-Gln	amino acid L-glutamine
LOX	lipoxygenase
Nec-1	necrostatin-1
NHE	normal hydrogen electrode
MeOAMVN	2,2'-azobis(4-methoxy-2,4-dimethylvaleronitrile)
ML	methyl linoleate
NADPH	nicotinamide adenine dinucleotide phosphate
NDGA	nordihydroguaiaretic acid
Nec-1	necrostatin-1
Nec-1i	necrostatin-1 inactive control
Nec-2	necrostatin-2
PA	preventative antioxidant
PDA	photodiode array detector
Pfa1	mouse embryonic fibroblasts (MEFs)
PMC	pentamethyl-6-chromanol
PPh_3	triphenylphosphene
PUFA	polyunsaturated fatty acid
Q	ubiquinol
RBF	round bottom flask
RIPK1	receptor-interacting serine/threonine-protein kinase 1
ROS	reactive oxygen species
RSL3	(1*S*,3*R*)-2-(2-chloroacetyl)-2,3,4,9-tetrahydro-1-[4(methoxycarbonyl) phenyl]-1*H*-pyrido[3,4-*b*]indole-3-carboxylic acid, methyl ester
RTA	radical-trapping antioxidant
STY-BODIPY	styrene-conjugated BODIPY

TAM	4-OH-tamoxifen
THF	tetrahydrofuran
THN	tetrahydronaphthyrinidol
TNBC	triple-negative breast cancer
TLC	thin-layer chromatography
α-TOH	α-tocopherol
UPLC	ultra performance liquid chromatography
x_c^-	cystine/glutamate antiporter

CHAPTER 1 Autoxidation and Ferroptosis

1.1 Autoxidation

Autoxidation – the oxidation of organic materials with molecular oxygen – is a process integral to both industrial organic applications and biological systems. Rigorously studied throughout the 20th century, regulation of autoxidation has remained of the utmost importance in industry. Autoxidation has been implemented as a means to produce higher-value, oxygen-rich compounds from oil and gas,[1] but can also serve as a key contributor towards product degradation.[2] Over the past 50 years, research has shown that a balance of beneficial and deleterious autoxidative processes is also prevalent in cellular environments.[3] Autoxidation facilitates crucial cellular mechanisms, serving as secondary messengers and contributing to immune cell efficacy, without which cells would cease to function.[4] Although autoxidation is essential in living systems, a surplus of autoxidative activity has been implicated in diseases such as Alzheimer's,[5] atherosclerosis,[6] and cancer.[7,8] The mechanisms which underlie and characterize autoxidation are critical to understanding its role in living systems and disease states.

1.1.1 Mechanism of Action

Autoxidation can be described as a free radical chain process which involves the generation of initial radical species, their exponential propagation, and the termination of these propagating chain reactions. Each of these reactive processes can be accomplished through three distinct mechanistic steps – initiation, propagation, and termination. Individual reactions in an autoxidation mechanism occur at specific rates, which will vary depending on the molecular environment (i.e. solvent, pH, etc.) and the physicochemical properties of the radical species present.[9] As an example, a given rate can increase via solvent-induced acceleration when the reaction products are highly solvated by the surrounding medium.[10] The magnitude of and variance between the rates of each step will define the efficiency and expected product ratios of a given free radical system. **Scheme 1.1** describes a general mechanism for autoxidation, although unique reaction steps may vary with substrate structure.

Scheme 1.1 General mechanism for the step-by-step autoxidation of hydrocarbons given the presence of an initiator and molecular oxygen.

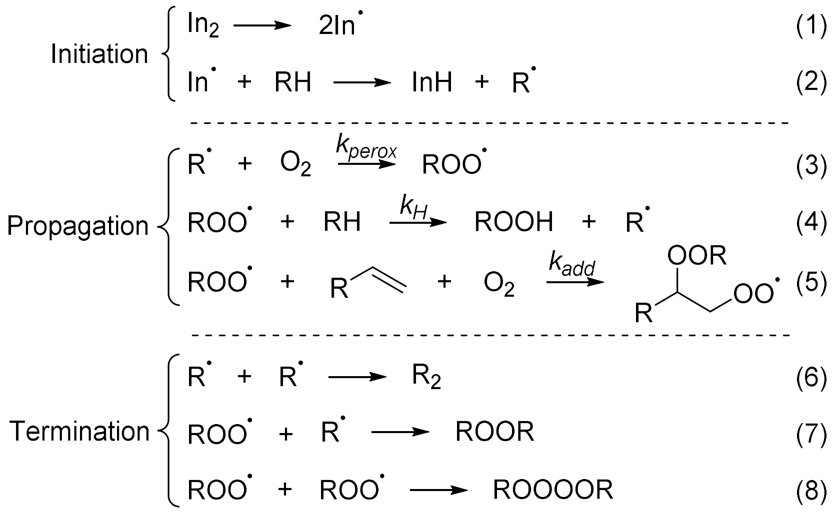

1.1.1.1 Initiation

The generation of an initial radical species is required to catalyze autoxidation. This process is the result of initiators (In), which are capable of producing radical species and promoting radical reactions. Initiators which generate radicals at known and constant rates are necessary for accurate characterization of autoxidation, and are commonly employed for *in vitro* studies. Azo compounds (**Scheme 1.2A**) are an ideal class of initiator as they are safe, easy to handle, and their rate of decomposition and solubility can be tailored by modification of functional groups.[11] Azo compounds such as 2,2'-azobis(2,4-dimethylvaleronitrile) (AIBN) are soluble in organic solution, while 2,2'-azobis(2-amidinopropane) dihydrochloride (AAPH) is soluble in aqueous environments. Alternatively, 2,2'-azobis(4-methoxy-2,4-dimethylvaleronitrile) (MeOAMVN) is advantageous for *in vitro* studies of lipid oxidation in a biological context as it readily incorporates into the hydrophobic region of micelles and membranes.[12] Functionalization aside, these initiators undergo unimolecular thermal or photocatalyzed decomposition to form carbon-centred radicals and molecular nitrogen (**Scheme 1.2B**).[11] Upon formation, the carbon-centred radicals will rapidly react with molecular oxygen to form peroxyl radicals at near diffusion-controlled rates ($k_{perox} = 10^9$ $M^{-1}s^{-1}$).[13] These initiator-derived peroxyl radicals may then react with local hydrocarbons via hydrogen atom transfer (HAT), forming a carbon-centred radical and initiating propagation of the radical chain reaction (**Scheme 1.1**, eq 2).

Scheme 1.2 Structure of common azo initiators AIBN, AAPH, and MeOAMVN (**A**) and the general mechanism for autoxidation initiator AIBN (**B**).

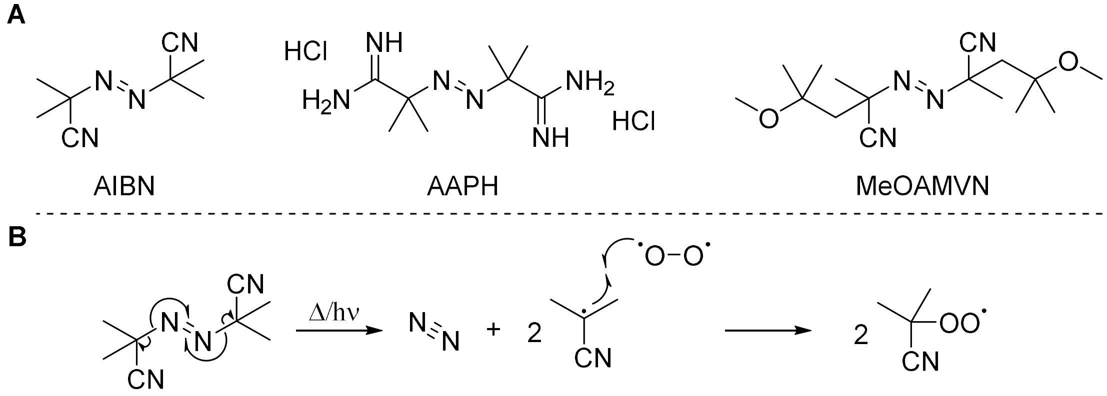

In biological systems the formation of radical initiators is complex, stemming from a wide range of exogenous and endogenous sources. Exogenous sources can be physical or chemical in nature, such as UV light, ionizing radiation, or carcinogenic substances containing reactive oxygen species (ROS) (**Figure 1.1**).[14] Electromagnetic radiation is absorbed by cell constituents, which can result in bond homolysis and ROS production, while exogenous substances contain ROS or precursory structures.

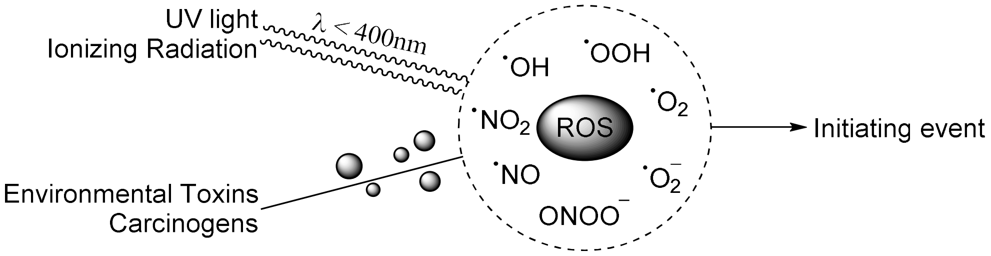

Figure 1.1 Exogenous sources of autoxidation and potential ROS they can produce in biological systems.

Endogenous sources of autoxidation include ROS production from enzymes such as NADPH oxidase and electron leakage from the electron transport chain (ETC) in the mitochondrial membrane. NADPH oxidase is a plasma membrane-bound enzyme complex involved directly in the production of superoxide, largely for host defense against pathogens (**Scheme 1.3A**).[15] However, superoxide production has its drawbacks, and can result in damage to host tissues through autoxidation. Research also indicates the ETC converts 1-2% of consumed O_2 into superoxide, many of which are the result of incorrect electron transfer during the coenzyme Q (Q) cycle. Shown in **Scheme 1.3B**, electrons are transferred from an unstable Q intermediate ($Q^{-\bullet}$) to readily available O_2 generating superoxide in the mitochondrial matrix.[16,17] In either case, an otherwise beneficial cell function exposes the organism to radical initiators, promoting autoxidation in the cellular environment.

Scheme 1.3 Superoxide production by enzymatic complex NADPH (**A**) and by erroneous electron transfer from Q during the Q cycle of oxidative phosphorylation in the inner mitochondrial membrane (**B**).

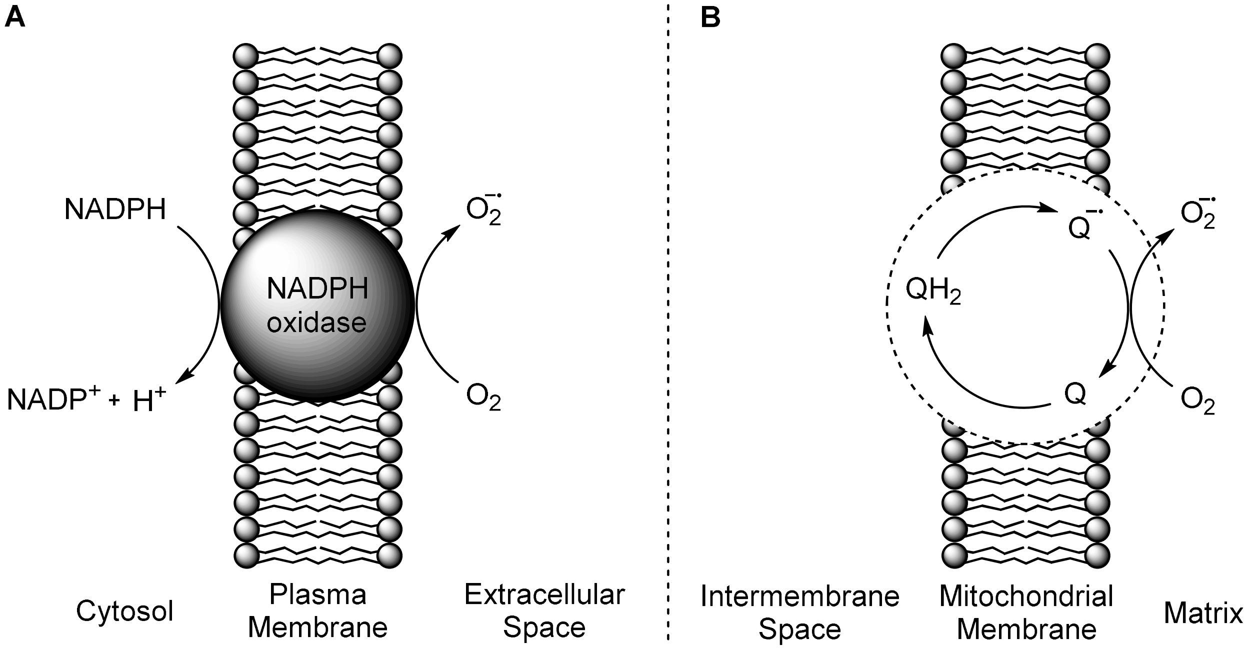

1.1.1.2 Propagation

Propagation of the radical chain occurs by a multi-step mechanism, the elements of which depend on the structural features of the propagating substrate. Newly formed carbon-centred radicals ($R^\bullet$) rapidly react with readily available molecular oxygen to form peroxyl radicals ($ROO^\bullet$) at rates that approach the diffusion-control limit, similar to azo initiators (**Scheme 1.1**, eq 3). Peroxyl radicals constitute the majority of available radical species, as subsequent reactions are relatively slow by comparison.[13] Peroxyl radicals may then abstract an available hydrogen atom from a neighbouring compound, forming a hydroperoxyl species (ROOH) and a new carbon-centred radical (**Scheme 1.1**, eq 4). Alternatively, peroxyl species may undergo addition with an olefin, and subsequently molecular oxygen, to form a dialkylperoxyl radical product (**Scheme 1.1**, eq 5). HAT and addition are common modes of propagation, however fragmentation, rearrangement, and cyclization are also common propagation steps which can occur, contributing to the diversity of product formation (**Scheme 1.4**).[18]

Scheme 1.4 Examples of radical propagation mechanisms. Atom transfer (**A**), addition (**B**), cyclization (**C**), rearrangement (**D**), and fragmentation (**E**) can all occur during autoxidation.

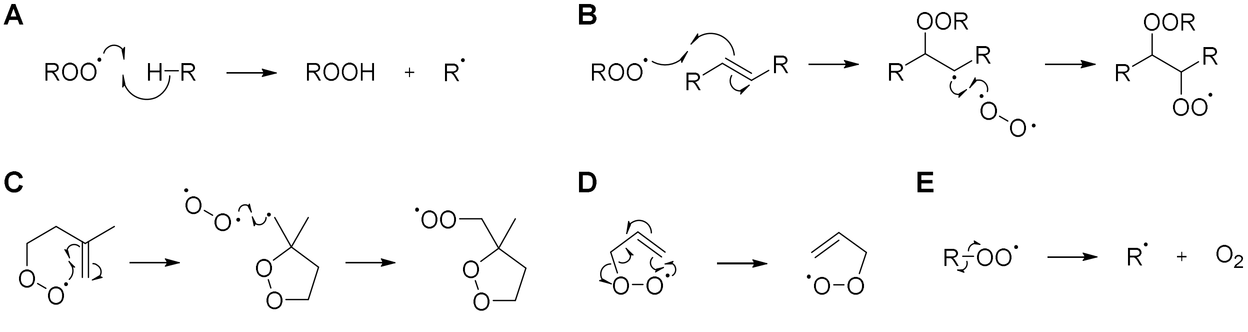

Structural properties of a peroxyl radical will largely determine the dominant mechanism and rate at which autoxidation propagates. These features are both closely related to the relative bond dissociation energies (BDEs) associated with the substrate. Readily abstractable H-atoms (i.e. those that exhibit a low BDE) promote HAT transfer, as shown in **Figure 1.2**. The allylic hydrogen of propene (88.8 kcal/mol) is far more readily abstractable than a hydrogen from the analogous propane (98.6 kcal/mol).[19] This is further exemplified by homoconjugation in 1,4-pentadiene, whose bisallylic hydrogen atom BDE is reduced by an additional 11.8 kcal/mol.[20,21] Substrates capable of propagating by addition show a similar trend, with conjugated olefins such as 1,3-butadiene possessing lower π-BDE than the nonconjugated 1-butene.[22] In both cases, these trends in BDE can be attributed to resonance stabilization of the radical species being formed.[23] Many additional factors (i.e. solubility, pH, temperature, etc.) contribute to a propagation rate, but between analogous substrates, BDE serves as a simple feature for contrasting relative rate.

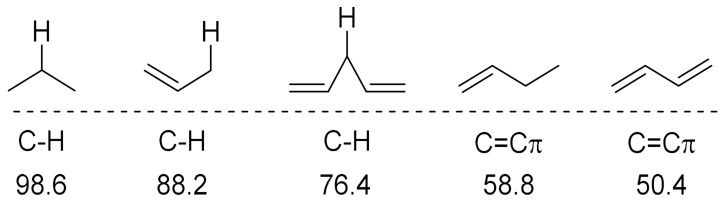

Figure 1.2 C-H and C=C π-bond BDEs (kcal/mol) in hydrocarbons of interest. Depicted are methane, propene, 1,4-pentadiene, ethylene, and 1,3-butadiene, left to right.[19,20,22]

It is by propagation mechanisms that radical species can persist in biological systems. Organisms possess a wide range of oxidizable substrates and relative rate of propagation defines which are most at risk. Polyunsaturated fatty acids (PUFAs) contain a variety of conjugated and homoconjugated structures and are as a result, a primary target for ROS in biological systems. These lipids play a central role in proper cell function, making management of their oxidation essential. PUFAs will be discussed in greater detail in **Section 1.1.2**.

1.1.1.3 Termination

Autoxidation reactions that eliminate radical species and break the radical chain reaction are referred to as termination steps, characterized by the coupling of two propagating radicals. Termination and propagation reactions compete during autoxidation, and their relative rates ultimately determine the magnitude of oxidation within a system. Although termination steps can occur between two carbon-centred radicals or between peroxyl and carbon-centred radicals, neither of these steps are rate-determining (**Scheme 1.1**, eq 6,7). Given that peroxyl radicals constitute the majority of active species, their combination is the largest contributor to termination, and establishes termination rate (**Scheme 1.1**, eq 8).[24] Peroxyl radicals combine to form a linear tetroxide intermediate species (ROOOOR) which undergoes an intramolecular decomposition reaction to form non-radical products through a process known as the Russell mechanism, yielding molecular oxygen, an alcohol, and a carbonyl (**Scheme 1.5**).[25,26]

Scheme 1.5 The Russell mechanism; the rate-determining termination step in autoxidation reactions, forming non-radical products from ROOOOR.

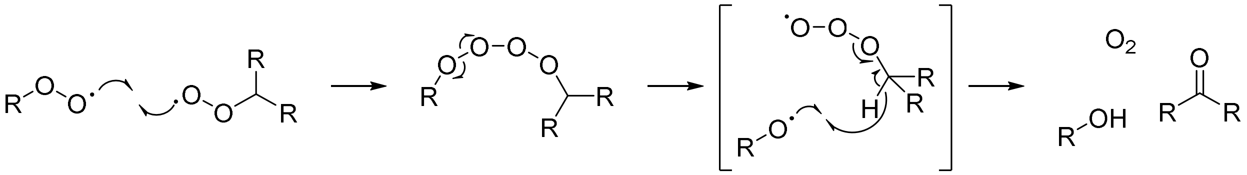

Cells possess mechanisms to terminate autoxidation and prevent an accumulation of oxidative stress. Glutathione peroxidases (GPxs) are part of a family of enzymes which decrease the number of autoxidizable species by reducing H_2O_2 and organohydroperoxides to water and alcohols, respectively (**Figure 1.3**).[27] Reduced species are significantly less likely to undergo HAT and promote autoxidation. Methyl hydroperoxide (CH_3OOH), for example, has an O-H BDE of 88 kcal/mol which, when reduced to methanol, becomes 104.6 kcal/mol, comparable to alkyl C-H bond strength.[19] By performing this reduction, GPx enzymes play an important role in maintaining cell homeostasis and preventing oxidative damage. The functions and mechanisms associated with GPx enzymes are discussed further in **Section 1.2.1**.

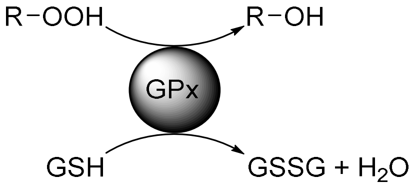

Figure 1.3 Basic catalytic reduction performed by various GPx enzymes using glutathione (GSH) as a reducing substrate for the hydroperoxyl species.

1.1.2 Lipid Peroxidation

Polyunsaturated fatty acids (PUFAs) along with saturated and monounsaturated fatty acids differentiate between the diverse structural forms of these amphipathic carboxylic acids (**Figure 1.4A**). In tissues, fatty acids commonly vary from 14 to 22 hydrocarbons in length, and are often found within phospholipid, cholesterol ester, or triglyceride macromolecules.[28] As the name implies, PUFAs are fatty acids characterized by two or more unsaturated double bonds within their hydrocarbon chains. Homoconjugated PUFAs are of special interest due to their highly oxidative nature, characterized by the low BDE of bisallylic hydrogens at their methylene bridge positions and reflected in their high propagation rate constants (k_P). Saturated fatty acids are straight chains often 14 to 18 carbon atoms in length and are relatively inert chemically, such as stearic acid (**Figure 1.4A**).[28] As one might expect, monounsaturated fatty acids fall somewhere in between; allylic sites promote HAT, but not nearly to the degree of PUFAs. If substrates are lacking bisallylic H-atoms for abstraction, addition (or other possible mechanisms) may compete with HAT and contribute to propagation.

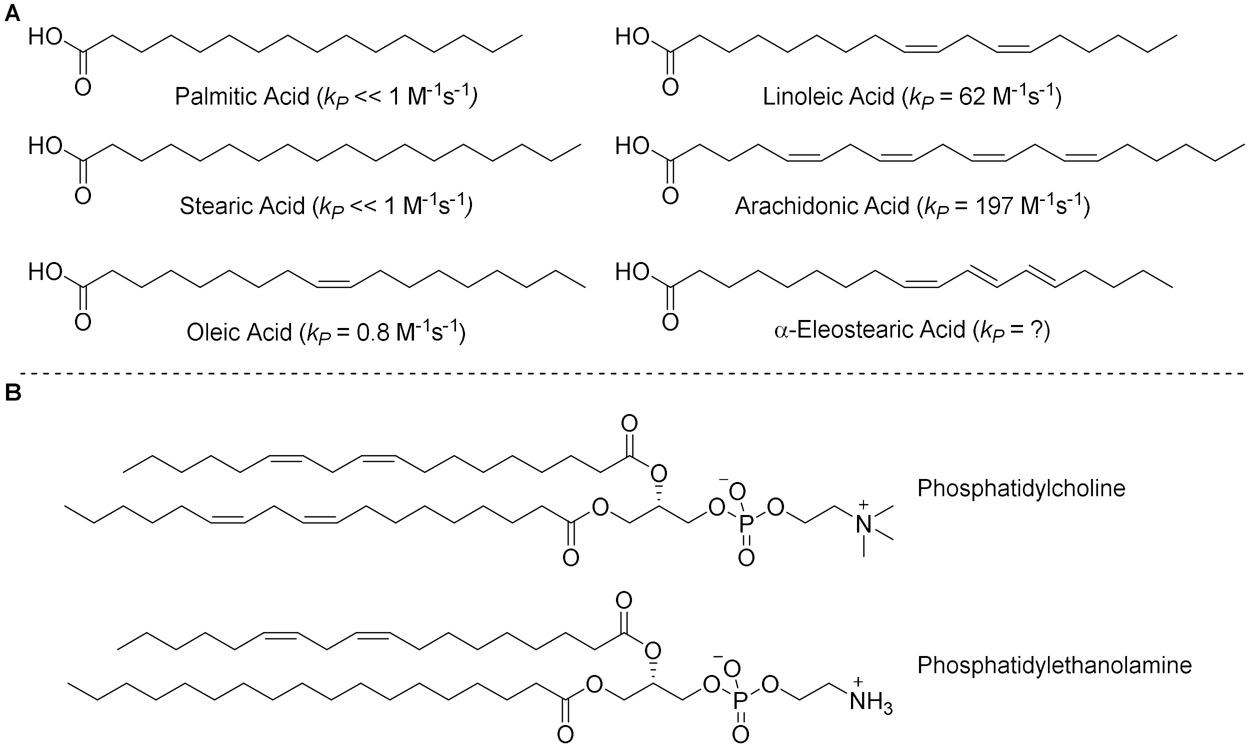

Figure 1.4 Chemical structures and rate constants of saturated, monounsaturated, and polyunsaturated fatty acids (**A**) and structures of common phospholipids with unsaturated fatty acid tails (**B**). Constants were measured at 37 °C.[29]

PUFAs are integral cellular components, associated with a wide range of metabolic functions. PUFAs are major substituents of over 80% of phospholipid structures, including phosphatidylcholine and phosphatidylethanolamine (**Figure 1.4B**).[30] Their presence in phospholipid bilayers such as the plasma membrane, endoplasmic reticulum, and nuclear membrane contributes to modulating membrane fluidity and flexibility of the cell and cellular compartments.[31] PUFAs also possess numerous biochemical functions such as cell signalling (e.g. gene regulation)[32] and neurotransmitter function (e.g. enhancing signal transduction).[31]

The mechanisms underlying PUFA oxidation are critical to our understanding of how these fatty acids oxidize and, in turn, influence cells. The intricacy of autoxidation pathways increases with the degree of unsaturation and PUFA lipid oxidation inevitably yields complex product distributions. For example, the homoconjugated diene methyl linoleate (ML) has one site at which HAT will generally take place, however five hydroperoxide isomers result (**Scheme 1.6**).[34] Abstraction of the ML bisallylic hydrogen will result in a delocalized pentadienyl radical, which will rapidly react with oxygen yielding the *cis,cis* homoconjugated product at C11, or a *trans,cis* conjugated hydroperoxide at either C9 or C13. The latter products can undergo reversible addition of oxygen (β-fragmentation) and subsequent rearrangement to produce the more thermodynamically stable C9 and C13 *trans,trans* products.[34]

Scheme 1.6 Autoxidative pathways and the five primary isomeric products of methyl linoleate. Naming convention identifies peroxyl addition site followed by conjugated diene configuration (*c* = *cis*, *t* = *trans*, $R_1 = (CH_2)_4CH_3$, $R_2 = (CH_2)_7COOCH_3$).[24]

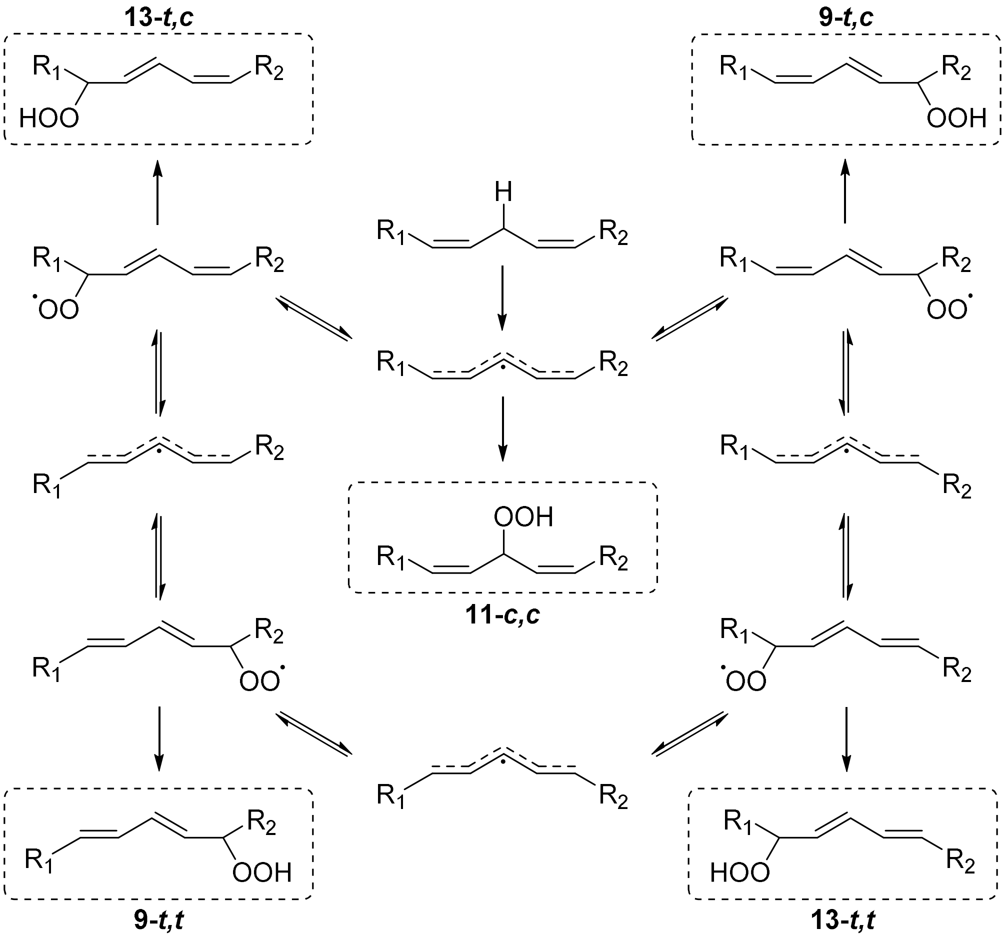

1.1.2.1 Conjugated Polyunsaturated Fatty Acids & α-Eleostearic Acid

Conjugated PUFAs lack bisallylic sites to amplify HAT and must instead rely on addition to drive propagation. Peroxyl addition is not generally observed in isolated double bonds, however conjugated olefins are prone to addition and will react with molecular oxygen to form peroxyl radicals and propagate by copolymerization (**Scheme 1.7**).[13,35] Although allylic HAT is also a feasible mechanism, it is less favoured in conjugated systems given the BDE increase when compared to bisallylic sites, and the limited number of abstractable H-atoms.[20] Addition rate is principally dependent on the stability of the radical product, which will increase with greater delocalization (i.e. conjugation).[36] Notably, the products of homoconjugated oxidation, such as those stemming from ML, are conjugated dienes which have been confirmed to propagate by addition.[37]

Scheme 1.7 Potential mechanism and route of copolymerization of butadiene and molecular oxygen. Molecular oxygen can react with the delocalized radical at C2 or C4 sites, and product distribution is consequently more complex than depicted.

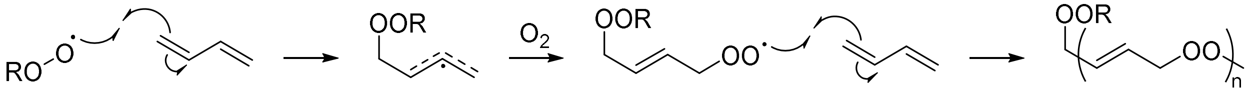

α-Eleostearic acid (α-ESA) is a PUFA possessing a 9-*cis,trans,trans* conjugated trienic unit (**Figure 1.4A**). α-ESA is a common substituent of plant essential oils and is the primary fatty acid present in Tung oil, constituting 80% of the extract.[38] Tung oil is also comprised of homoconjugated and other olefinic fatty acids which, along with α-ESA, are esterified as triglycerides forming a highly oxidizable oil commonly used in inks, coatings, and resins. Unfortunately, minimal kinetic data is available for conjugated PUFAs when compared to homoconjugated lipids, and α-ESA is no exception. Investigations into the therapeutic benefits of α-ESA suggest a mechanism of action unique from other PUFAs;[39,40] however, no concrete results describing its kinetics or characterization have been completed to date.

1.1.3 Radical-Trapping Antioxidants

For industrial products and biological systems, autoxidation is often an adverse process resulting in the degradation of material and accumulation of undesirable products; inhibition of autoxidation is a necessity. There are two classes of antioxidants which can meet this need, preventative antioxidants (PAs) and radical-trapping antioxidants (RTAs). Preventative antioxidants interfere with chain-initiation, reducing the rate by which propagating chains form, commonly decomposing alkyl and hydroperoxides.[41] PAs often take the form of enzymes (e.g. GPxs) in biological systems and organosulfur compounds in industry. RTAs, also known as chain-breaking antioxidants, are compounds which outcompete propagation in an autoxidation reaction by capturing chain-carrying radical species, often by HAT of a labile RTA-bound hydrogen.[42,43] The resulting radicals are persistent and slow to react, characterized by low BDE and corresponding greater radical stability, which is reflected in their inhibition rate constant (k_{inh}). Although BDE is often tied to k_{inh}, RTA implementation in specialized environments such as liposomes and cells indicates BDE is not always an accurate indicator of activity.[44] Similar to propagation rate constants in radical species, k_{inh} is influenced by several other factors including solubility and pH. RTAs often take the form of phenols or aromatic amines, substituted to optimize their potency (**Figure 1.5**).[41]

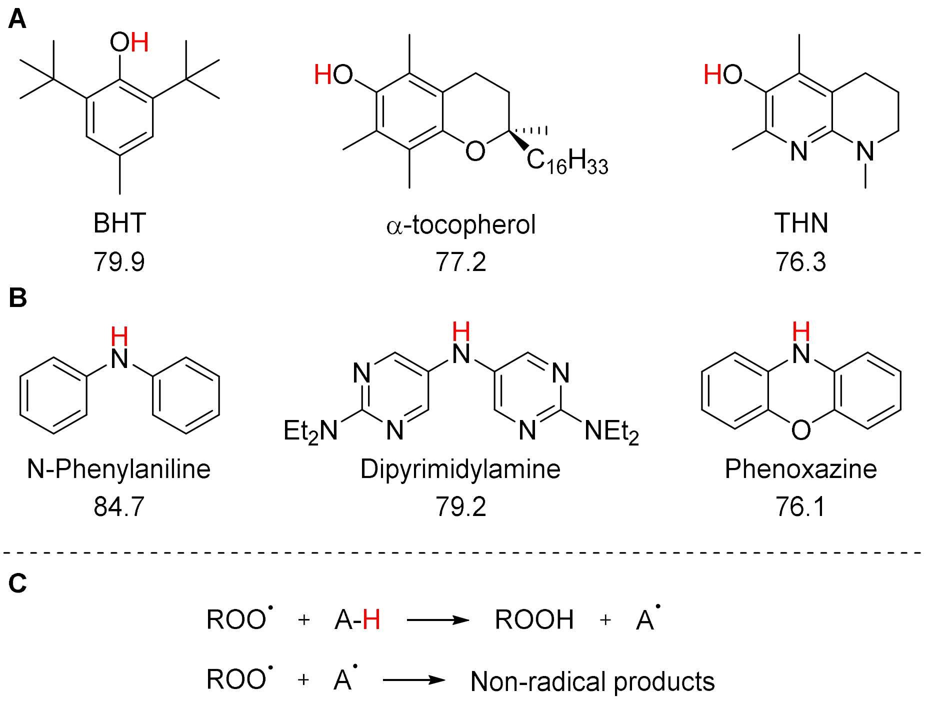

Figure 1.5 Structures of common phenolic (**A**) and aromatic amine (**B**) RTAs and their respective labile H-atom BDEs, in kcal/mol. Inhibition of peroxyl radicals by RTAs (**C**). Labile H-atoms are highlighted in red.[42,43,45]

Phenols are considered the quintessential RTA and are characterized by the phenol scaffold, which contains a weak O-H bond (87 kcal/mol).[43] This bond can be weakened further by the addition of electron-donating groups (EDGs) which will stabilize the phenoxyl radical.[46] By manipulating substitutions on a phenol or other RTA, O-H BDE can be reduced to form effective RTAs such as 2,6-di-*tert*-butyl-4-methylphenol (BHT) and nature's best antioxidant, α-tocopherol (α-TOH) (**Figure 1.5A**).[47,48] Incorporating nitrogen atoms into the phenolic aromatic systems within antioxidants also contributes to reactivity and can help stabilize an RTA towards autoxidation.[49] For example, tetrahydronaphthyridinols (THNs), aza analogs of α-TOH, possess two nitrogen atoms in its scaffold and constitute some of the most potent inhibitors of lipid peroxidation.[44]

Diarylamine derivatives represent another large library of RTAs, used industrially since the 1950s (**Figure 1.5B**).[43] Although the labile N-H bond of aromatic amines is not as strongly impacted by EDGs as phenols, incorporating nitrogen heteroatoms into the scaffold facilitates the synthesis of air-stable RTAs which are highly reactive with peroxyl radicals.[49] An additional method of improving HAT involves fusing the aromatic rings with heteroatoms to form tricyclic amines, such as phenothiazine and phenoxazine. In the case of phenoxazines, an aryl linkage via an oxygen atom provides an 8.6 kcal/mol decrease in N-H BDE.[45]

RTAs are commonly described using their HAT mechanism which results in the formation of non-radical products (**Figure 1.5C**); however, aminic RTAs are also known to participate in catalytic mechanisms. At elevated temperatures, the catalytic activity of diarylamines can be explained by a process known as the Korcek cycle (**Scheme 1.8**).[50] Diarylamines undergo HAT with an alkyl peroxide radical followed by subsequent reaction with a second alkyl peroxide producing a diarylnitroxide species. Regeneration of the diarylamine species is then proposed to occur under high temperature conditions in the presence of an alkyl radical forming a non-radical carbonyl product, recently demonstrated to occur by a pericyclic retro-carbonyl-ene reaction.[51]

Ambient and physiological temperatures are insufficient to regenerate the initial amine species, however, nitroxide intermediates may undergo additional catalytic termination and regeneration mechanisms prolonging autoxidative inhibition.[43] In liposomes and aqueous media, single electron transfer occurs between nitroxide and alkyl peroxyl species (**Scheme 1.8**). The resulting oxoammonium ion can subsequently undergo hydride transfer, producing a hydroxylamine derivative capable of HAT, reducing a peroxyl radical and regenerating the nitroxide. This hydride transfer was observed to occur between oxoammonium ion and NADPH, a natural hydride donor produced by cells.[52] This mechanism provides justification for the cytoprotective effects observed from nitroxide-based compounds, discussed in **Section 1.2.2**.

Scheme 1.8 Regeneration of diarylamine RTAs via the Korcek cycle, as well as in aqueous solution and liposomes under physiological conditions. The Korcek cycle only occurs at elevated temperatures.

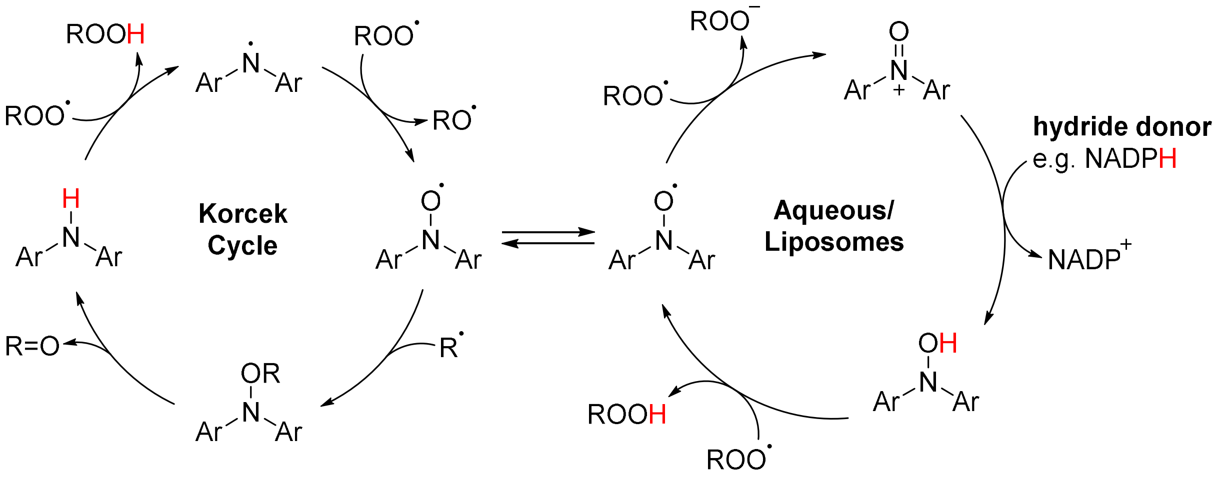

1.2 Ferroptosis: A Unique Form of Regulated Cell Death

Regulated cell death has traditionally been divided between apoptosis and necroptosis, two morphologically and biochemically distinct modalities.[53] The former, apoptosis, is characterized by a reduction in cellular and nuclear volume, resulting in an increase of cellular density.[54] During apoptosis, nuclear fragmentation plays the predominant role in cellular degradation through the agglutination of chromatin, known as pyknosis. In contrast, necroptotic cells experience swelling organelles and cytoplasm alongside condensation of chromatin.[55] The resulting increase in cell volume leads to disruption of the plasma membrane and leakage of cellular contents. From a biochemical perspective necroptosis is characterized by a lethal depletion of intracellular adenosine triphosphate (ATP).[56]

In 2003, a form of cell death was identified which lacked nuclear morphological degradation, uncharacteristic of traditional pathways.[57] Several years later, increased intracellular ROS was associated with the same non-traditional cell death, and iron chelating agents were identified as inhibitors.[58,59] In 2012 this cell death pathway was formally named ferroptosis, after its iron-dependent mechanism.[60] Ferroptosis was therein morphologically characterized by reduced mitochondrial size, associated with increased inner membrane density, cristae reduction, and outer membrane rupture. Unlike previously reported cell death mechanisms, ferroptotic cells were found to have intact nuclei and plasma membranes. Since its discovery, ferroptosis has been implicated in various cancers[61–63] as well as neurological,[64,65] kidney,[66] and heart disease,[67] motivating research aimed at elucidating its mechanism.

Preceding the characterization of ferroptosis, the cell death pathway ‘oxytosis’ was identified as a result of glutamate-induced cytotoxicity in HT-22 neuronal cells.[68] Morphology reported for oxytosis is similar to that of ferroptosis, with intact nuclei and damage localized in membranous organelles (e.g. endoplasmic reticulum and golgi apparatus), most severely in mitochondria which were swollen, with cristae reduction.[68] Induction of oxytosis also reflects ferroptosis biochemically, with glutamate inhibiting the membrane-bound x_c^- antiporter, leading to an increase in cellular ROS (as described in **Section 1.2.1**). Glutamate-induced cytotoxicity of HT-22 cells is a commonly studied model for oxidative cell death, and is studied alongside ferroptotic models.[44,69] Although we have distinguished oxytosis from ferroptosis herein, the similarities between these cell death pathways has led to the suggestion they are in fact two names for the same pathway.[70]

1.2.1 The Biochemistry Behind Ferroptotic Cell Death

Ferroptosis can be biochemically described as an intracellular iron-dependent accumulation of lipid–derived hydroperoxide species.[60] Formation of lipid hydroperoxides has been implicated in several deleterious effects which may contribute to cell death. Lipid-derived electrophiles (e.g. aldehydes, epoxides) can arise from hydroperoxides, which are known to form adducts with nucleic acids and proteins, disrupting gene expression and causing cellular damage.[71] In addition, oxidized PUFAs embedded in the hydrophobic portion of the phospholipid bilayer can aggregate and to form 'hydrophilic pores' which disrupt membrane permeability and fluidity, leading to cellular dysfunction.[32] Although certainly detrimental, the extent to which lipid oxidation leads to cellular dysfunction still remains largely unknown.

The production of lipid-derived hydroperoxide species can be the result of Fenton chemistry, enzyme-mediated peroxidation, and intracellular autoxidation (**Figure 1.6**).[72] Fenton-like reactions involve catalytic single electron transfer from low-valent iron releasing peroxyl species, although one-electron donors can initiate this transfer, if available.[73] Lipoxygenase (LOX) enzymes actively promote PUFA oxidation by catalyzing dioxygenation at bisallylic moieties (**Section 1.2.3**).[74] Reactions between PUFAs and endogenous ROS can also initiate oxidation through previously discussed autoxidation mechanisms. Once generated, these initial peroxyl radical species are capable of propagation by autoxidative mechanisms, the products of which can accumulate and result in ferroptosis. Typically, accumulation of peroxyl species is endogenously managed by reduction to their innocuous corresponding alcohols by peroxidase enzymes, however, these natural mechanisms are overwhelmed during ferroptotic cell death.

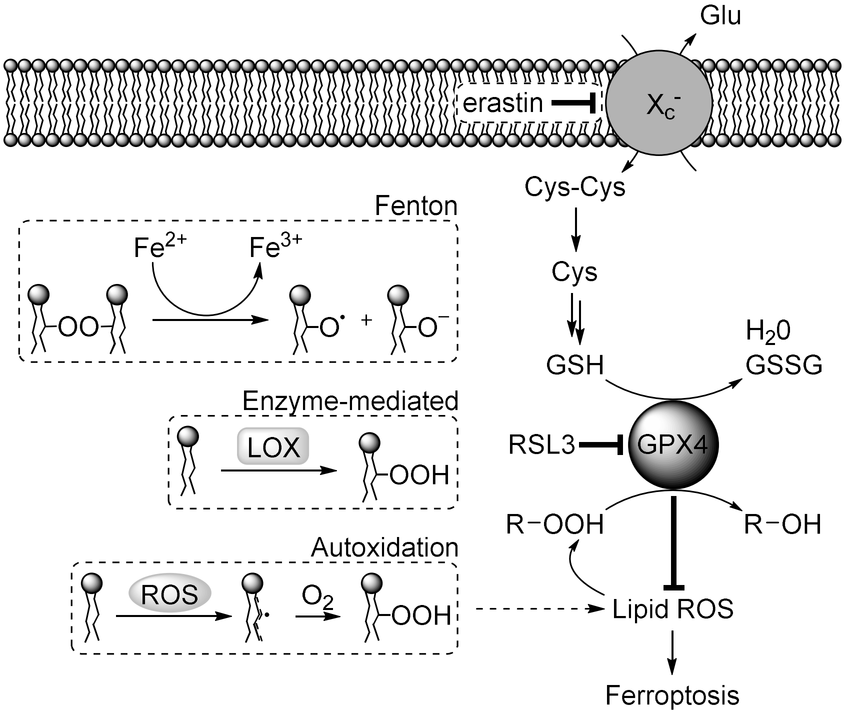

Figure 1.6 Key mechanistic steps in the biochemical regulation of ferroptosis. The inhibitory role of GPX4 in reducing lipid ROS is shown as well as its substrates and their upstream regulatory precursors, including the cystine/glutamate (Cys-Cys/Glu) antiporter system (x_c^-). GPX4 inhibitors erastin and RSL3 have also been included. Common sources of lipid-derived hydroperoxides are depicted, including Fenton chemistry, LOX enzyme-mediated dioxygenation, and autoxidation initiated by cellular ROS.

1.2.1.1 GPX4 Catalysis: From System x_c^- to Glutathione

During normal cellular function, lipid hydroperoxides are reduced to their non-toxic alcohols by the enzyme glutathione peroxidase 4 (GPX4) within the phospholipid bilayer (**Figure 1.6**).[27] GPX4 performs this lipid-reduction catalysis by consuming a pair of glutathione co-substrates (GSH), which are dimerized via a disulfide bridge yielding glutathione disulfide (GSSG) and water (chemical structures are depicted in **Figure 1.7**). Provided a healthy cellular environment and available substrates, GPX4 can remove hydroperoxides from cellular lipid bilayers, preventing their accumulation and suppressing ferroptosis.

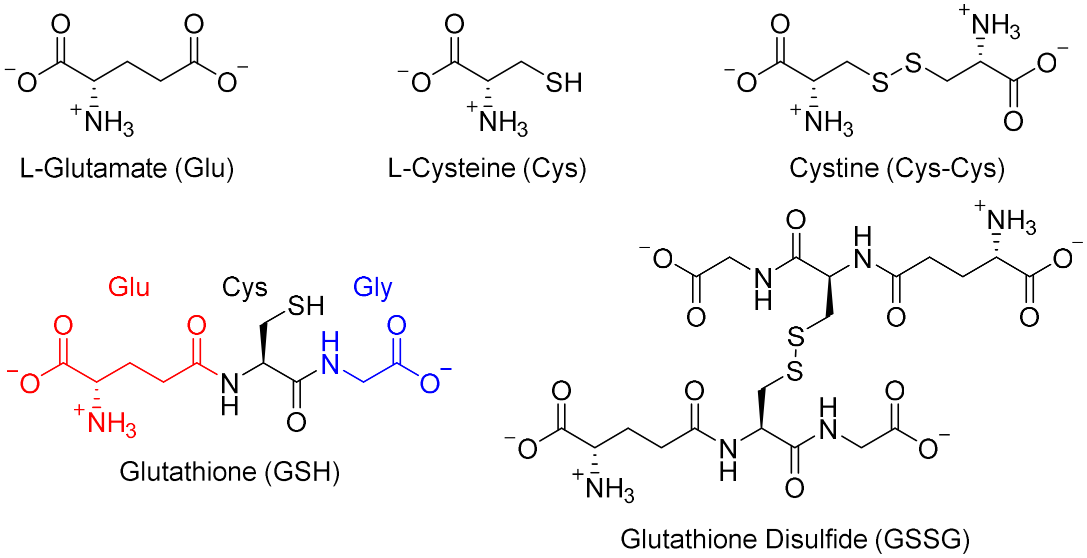

Figure 1.7 Amino acid and oligopeptide structures associated with GPX4 enzymatic function in the x_c^- antiporter pathway at physiological pH.

GPX4 substrate GSH is a tripeptide found in all mammalian tissues consisting of glutamate, cysteine, and glycine residues (**Figure 1.7**). Its biosynthesis involves two ATP-dependent enzymatic steps, first is the rate-limiting formation of γ-glutamylcysteine from glutamate and cysteine, followed by addition of glycine (**Scheme 1.9**).[75,76] GSH formation is particularly sensitive to cysteine availability, which is regulated by a number of pathways including the biosynthesis of cysteine via the transulfuration pathway and import of cystine (a cysteine dimer) via the x_c^- enzymatic antiporter. In the extracellular environment, available cysteine rapidly oxidizes to cystine, which is then transported into the cell in exchange for intracellular glutamate by the x_c^- antiporter in a 1:1 stoichiometric ratio (**Figure 1.6**).[75] Once inside the cell, cystine is rapidly reduced back into cysteine, promoting GSH synthesis. Although there are numerous methods by which a cell can acquire cysteine, the x_c^- transporter is critical for cellular viability and its disruption leads to the accumulation of lipid-derived hydroperoxides and subsequent ferroptosis.[77]

Scheme 1.9 Two-step enzymatic biosynthesis of GSH from its three amino acid residue precursors. The steps are catalyzed, in the presence of ATP, by γ-glutamylcysteine synthetase (GCL) and GSH synthetase (GS) respectively.

$$\text{L-glutamate} + \text{L-cysteine} + \text{ATP} \xrightarrow{\boxed{\text{GCL}}} \gamma\text{-glutamyl-L-cysteine} + \text{ADP} + \text{Pi}$$

$$\gamma\text{-glutamyl-L-cysteine} + \text{L-glycine} + \text{ATP} \xrightarrow{\boxed{\text{GS}}} \text{GSH} + \text{ADP} + \text{Pi}$$

1.2.1.2 Induction of Ferroptosis

There are several distinct methods available for inducing ferroptosis via direct or indirect inhibition/degradation of GPX4 and its activity. Preventing GPX4 activity will reduce the antioxidant capacity of the cell, leading to an accumulation of hydroperoxides in the phospholipid bilayer, and inducing ferroptosis. Indirect inhibition can be accomplished through the suppression of the x_c^- antiporter, which will prevent cystine import, starving GCL of cysteine and, as a result, GPX4 of GSH. With insufficient GSH for function, GPX4 cannot reduce lipid hydroperoxides, leading to their accumulation. Two common agents for x_c^- suppression include erastin and glutamate. Erastin was the prototype ferroptosis inducer, which has been demonstrated as a direct inhibitor of system x_c^- (**Figure 1.8**).[57,78] Since its discovery, erastin has been found to have more than one cellular target, contributing to ferroptosis through several modes of action. Notably, erastin induces mitochondrial dysfunction, releasing oxidative species by direct interaction with voltage-dependent anion channels (VDACs) and also promotes chaperone-mediated autophagy (CMA), leading to GPX4 degradation.[58,79] Although most commonly identified as a system x_c^- inhibitor, erastin remains a compound of interest with a spectrum of targets and effects not fully understood.

Glutamate is a charged amino acid, neurotransmitter, and ferroptotic inducer which can severely suppress or inhibit cystine cellular uptake.[77] System x_c^- function is driven, in part, by glutamate flowing down its concentration gradient, from high intracellular to low extracellular concentrations. High extracellular concentrations negate this gradient, disrupting transmembrane transport, starving GPX4 of GSH, and inducing ferroptosis.[80] Although effective, similar to erastin, the effect glutamate has on cells is not limited to x_c^- inhibition; glutamate can also induce Ca^{2+} influx, mitochondrial damage, and chromatin fragmentation.[60]

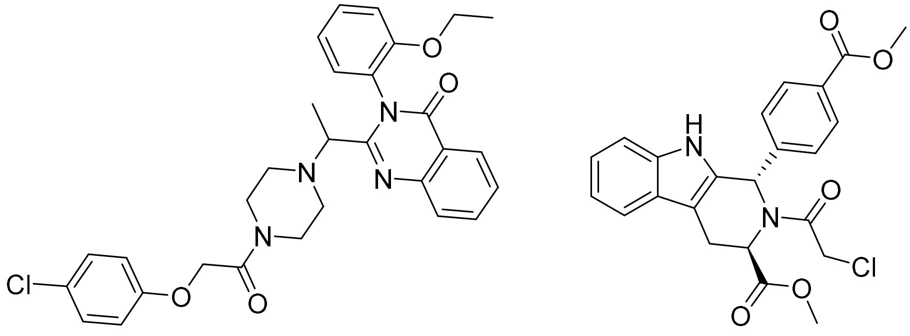
Erastin

RSL3

Figure 1.8 Common ferroptosis inducers erastin (x_C^- inhibition) and RSL3 (GPX4 covalent active site inhibition).

Direct inhibition of GPX4 is also possible using the small molecule diastereomer (1*S*-3*R*)-RSL3 (herein referred to as simply RSL3) (**Figure 1.8**). In 2014, Yang et al. identified RSL3 as a covalent inhibitor of GPX4, later confirming the drug binds to the active site selenocysteine residue.[81,82] RSL3 acts much more downstream than erastin and glutamate, directly inhibiting the GPX4 reduction mechanism while GSH levels remain intact, providing a more precise initiator of ferroptosis, with less concern of systemic cellular influence.

1.2.2 Suppression of Ferroptosis

Studying ferroptotic inhibitors is vital towards understanding preventative and initiative mechanisms of ferroptosis. Much of what has been reported on the mechanism of ferroptosis has been gleaned from screening compound libraries for small molecule inhibitors (e.g. iron chelators) and more recently genetic screens aimed at identifying genes involved in positive (e.g. ACSL4)[83] or negative (e.g. FSP1)[84] regulation. As a result of these screens, cytoprotection has been associated with depletion of active cellular iron or prevention of lipid peroxide accumulation.[53] Iron chelating agents, such as deferoxamine and ciclopirox olamine, have been successfully administered to prevent the accumulation of iron (**Figure 1.9A**).[60,85]

Biochemically, iron depletion can reduce the effects of oxidation-promoting enzymes (e.g. LOX) and peroxide-forming chemical reactions, rescuing cells from ferroptosis.[72]

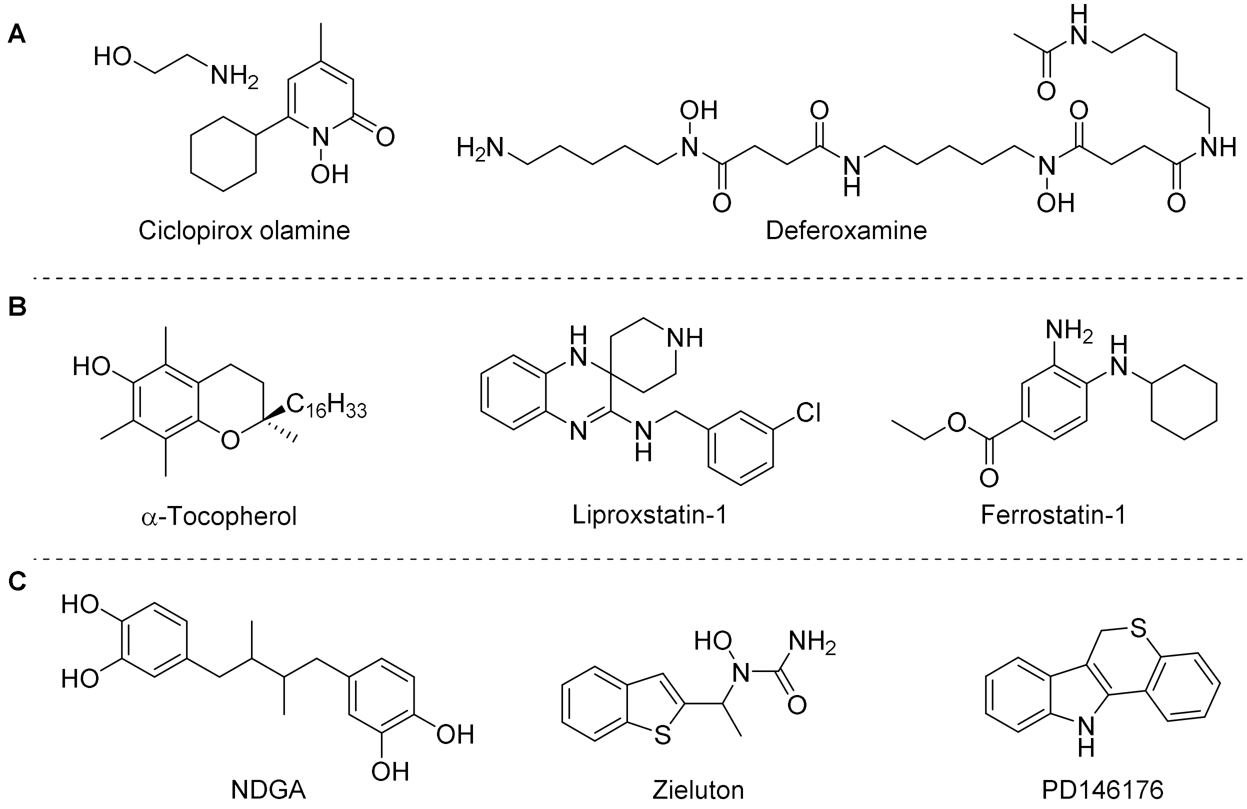

Figure 1.9 Cytoprotective compounds associated with the prevention of iron accumulation and lipid peroxidation. Pictured above are examples of iron chelators (**A**), RTAs (**B**), and LOX inhibitors (**C**).

RTAs inhibit ferroptosis by limiting the propagation of existing peroxyl species, serving as good H-atom donors to trap the radical species and break the radical chain reaction, particularly in lipid bilayers (**Figure 1.9B**). The relationship between biological membrane preservation and RTAs was realized through observations with α-TOH, nature's best antioxidant.[48] Solubility and compound structure were found to play a major role in the potency of an RTA within a cell, and lipid-soluble THNs, modelled after α-TOH, have proven their efficacy as ferroptotic inhibitors.[44] The effectiveness of THNs was optimized when nitrogen-bound alkyl chains ranged from 12 to 15 carbons in length, analogous to membrane lipid tail lengths. A similar effect was found in liproxstatin-1 (Lip-1) and ferrostatin-1 (Fer-1), which are less intrinsically reactive towards peroxyl radicals than α-TOH, yet provide greater inhibition within lipid bilayers.[44] This effect has been attributed to decreased H-bonding interactions with phospholipid head groups and surrounding aqueous media, resulting in improved lipid reactivity.

1.2.3 Lipoxygenases: Enzyme-mediated Lipid Peroxidation

Lipoxygenases (LOXs) are non-heme iron-containing dioxygenases, which catalyze the addition of molecular oxygen at bisallylic sites of PUFAs. The most widely accepted mechanism of action is a free radical mechanism in which catalysis is initiated by bisallylic HAT, forming a delocalized pentadienyl radical, before a LOX-controlled regioselective oxygen addition and subsequent reduction to form the hydroperoxyl species (**Scheme 1.10A**).[32] These enzymes are present in a diverse range eukaryotic organisms, including plants, animals, and fungi, with six isoforms present in humans (5-LOX, p12-LOX, 12R-LOX, 15-LOX-1, 15-LOX-2, and eLOX-3), the first five of which are shown oxidizing arachidonic acid in **Scheme 1.10B**.[74] Naming conventions for LOX distinguish between their regioselectivity, with a numerical assignment designating the carbon subject to dioxygenation (i.e. 15-LOX oxidizes the fifteenth carbon of arachidonic acid). Notably, although LOX preferentially bind free fatty acids, 15-LOX-1 has been found capable of oxygenating phospholipid- and cholesterol-bound PUFAs as well.[32,86] In addition, five of the six human LOX isoforms serve as PUFA dioxygenases, however eLOX-3 is the exception to the rule, serving as a hydroperoxide isomerase and catalyzing the formation of epoxyalcohol and epoxyketone lipid derivatives (**Scheme 1.10C**).[74]

Scheme 1.10 LOX enzyme catalysis in the presence of molecular oxygen on a homoconjugated PUFA (**A**), catalysis of arachidonic acid (AA) peroxidation via human LOX isoforms 5-LOX, p12-LOX, 12R-LOX, 15-LOX-1, and 15-LOX-2 (**B**), and eLOX-3 catalyzed formation of epoxyalcohol/ketone products (**C**). Common LOX substrates include arachidonic acid, eicosapentaenoic acid, docosahexaenoic acid, and linoleic acid. (HPETE: hydroperoxyl eicosatetraenoic acid)

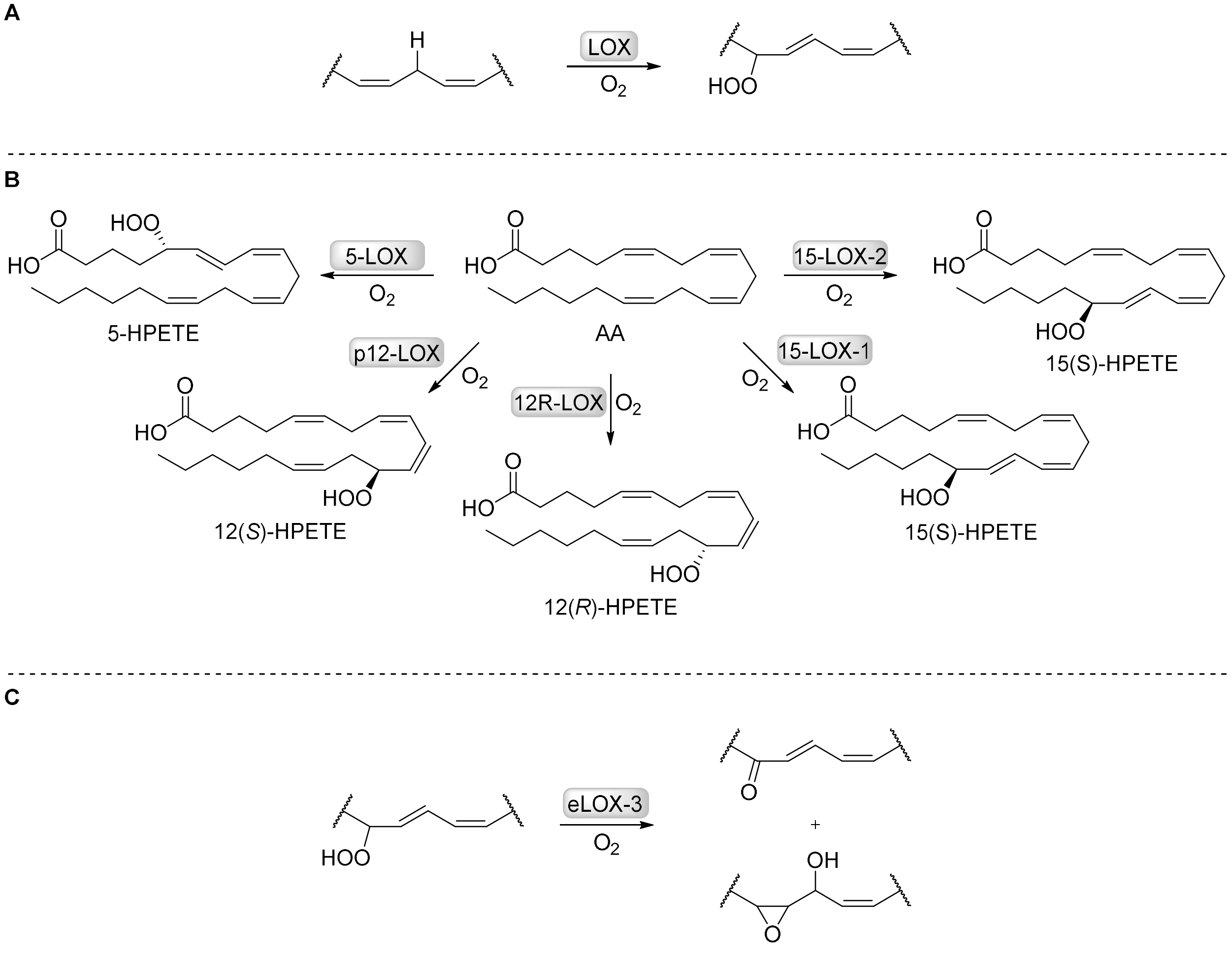

Predictably, forming a causative relationship between the oxidative function of LOX and ferroptosis has been a source of interest in modern research.[87–89] As an endogenous source of lipid peroxidation, LOX activity contributes to the cellular pool of lipid hydroperoxides and can therefore promote ferroptosis. The significance of this contribution has been measured by gene regulation[66] (e.g. gene knockouts, RNA interference) and pharmacological inhibition.[88] Although ferroptotic resistance is conferred in gene-regulated cell studies, only pharmacological inhibition has translated rescue activity in animal models (i.e. GPX4$^{-/-}$ knockout mice).[90] In addition, no individual LOX has been found solely responsible for inducing ferroptosis[66,90] and although ferroptosis is shown to be LOX-activity dependent, LOX-mediated oxidation was found negligible unless intracellular GSH was depleted.[82,91]

The essential role lipid peroxidation plays in the execution of ferroptosis has led to the investigation and development of pharmacological, cytoprotective strategies aimed at preventing initiation and propagation.[92] Given that lipid peroxidation is mediated both by enzymatic (LOX) and non-enzymatic pathways (autoxidation), cytoprotection has been investigated in the form of enzymatic inhibitors (LOX inhibitors) and autoxidation inhibitors (RTAs), examples of which are depicted in **Figure 1.9**. LOX inhibitors have been developed to obstruct LOX activity, preventing the catalytic formation of autoxidation-promoting initiative peroxyl species. There are five principle groups to classify LOX inhibitors: redox inhibitors interfering with catalytic iron, active site-targeted iron chelators, competitive inhibitors, irreversible 'suicide' inhibitors, and allosteric inhibitors.[32] These can be universal (pan) LOX inhibitors, such as nordihydroguaiaretic acid (NDGA), a redox inhibitor targeting all LOX isoforms, or isoform-specific such as Zileuton or PD146176, which inhibit 5-LOX and 15-LOX-1, respectively.[73,93,94] Although LOX inhibitors have been reported as cytoprotective towards ferroptosis, these compounds often exert off-target effects, making the root cause of their influence unclear. In the context of lip-1, the RTA had initially been identified as a high-affinity 15-LOX inhibitor.[88] It has since been shown that Lip-1 rescues cells from ferroptosis at multiple orders of magnitude lower than concentrations at which it suppresses LOX activity, cementing its role as an RTA ferroptotic inhibitor.[44] Although LOX plays a role in contributing to lipid peroxidation in ferroptosis, the extent to which it does is still up for debate.

Scheme 1.11 Key steps of lipid oxidation exemplifying the inhibitory actions of different cytoprotective compounds.

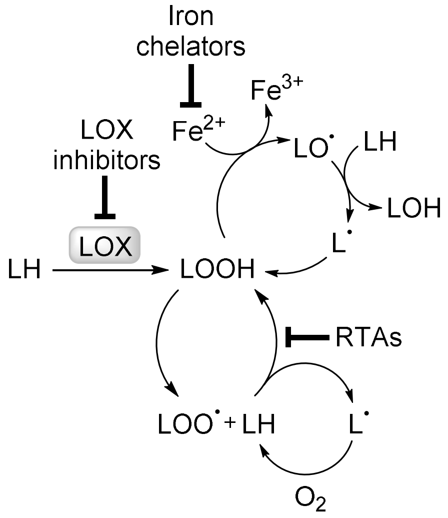

1.3 Research Objectives

In the past several years, our research group has aimed to contribute to a better understanding of the initiation and execution mechanisms of ferroptotic cell death. In particular, emphasis has been placed on resolving the role of lipid peroxidation (autoxidation) in this process. These explorations have been pursued on several fronts, two of which are discussed herein.

1.3.1 The Role of Lipoxygenases in Ferroptosis

Since the realization that ferroptosis is tied to an accumulation of lipid peroxidation, researchers have attempted to find evidence of a regulated (i.e. enzyme-mediated) mechanism, the prime suspect being LOX.[60,82,88] Although LOX-dependent ferroptosis has been supported by ferroptotic suppression using LOX inhibitors,[88,91] LOX gene regulation fails to confirm dependence.[90] In 2018, our lab presented findings that LOX inhibition is not tied to ferroptosis suppression, and LOX merely contributes to the cellular pool of lipid-derived peroxide species.[95] We sought to expand on this work by studying the impact of RTAs, RTA-active LOX inhibitors, and RTA-inactive LOX inhibitors on cell lines in which LOX catalysis has been implicated in ferroptosis (HT-1080, HT-22)[80] and oxytosis (HT-22).[68] In addition, we aimed to elucidate the RTA, redox, and anti-ferroptotic activity of necrostatin-1 (Nec-1) (**Figure 1.10**), a necroptosis inhibitor also implicated in the suppression of ferroptosis.

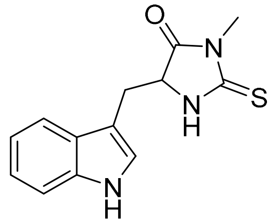

Figure 1.10 Chemical structure of necroptosis inhibitor Nec-1, recently found to also possess anti-ferroptotic properties.

1.3.2 Conjugated Lipids and Ferroptosis

Non-conjugated fatty acids sensitize cells to ferroptosis by increasing the pool of oxidizable lipid substrates. Recently, it has been reported that conjugated fatty acids – and in particular, α-ESA – induce ferroptosis, the molecular basis for which remains unclear. We propose that α-ESA (**Figure 1.11**) would induce lipid peroxidation by forming dialkylperoxides in cellular membranes, which would be resistant to detoxification by GPX4 and instead decompose into chain-initiating radicals. In theory, the characteristic α-ESA trienic unit would facilitate this process by propagating autoxidation by addition, not HAT.

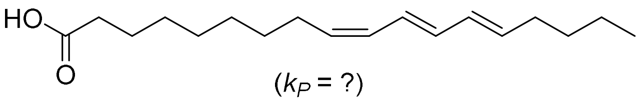

Figure 1.11 Chemical structure of trienoic fatty acid and potential ferroptotic inducer, α-ESA.

Kinetic studies on the oxidation of α-ESA are limited and thus, our first objective was to investigate if, indeed, the primary mechanism for α-ESA autoxidation is peroxyl radical addition. We sought to derive preliminary HAT and addition propagation rate constants for naturally derived α-ESA. Furthermore, we aimed to synthesize a lipid analogous to α-ESA, deuterated at allylic positions, to study in parallel and corroborate results from the natural analog. Lastly, we expected to isolate dialkylperoxide products from α-ESA autoxidation and measure their ability to act as initiators of lipid peroxidation and ferroptosis.

1.4 References

1. Teles, J. H., Hermans, I., Franz, G. & Sheldon, R. A. Oxidation. in Ullmann's Encyclopedia of Industrial Chemistry 1–103 (Wiley-VCH Verlag GmbH & Co. KGaA, 2015). doi:10.1002/14356007.a18_261.pub2
2. Brydson, J. A. Additives for Plastics. in Plastics Materials 134–145 (Elsevier, 1999). doi:10.1016/B978-075064132-6/50048-6
3. Porter, N. A. Mechanisms for the Autoxidation of Polyunsaturated Lipids. Acc. Chem. Res. 19, 262–268 (1986).
4. Finkel, T. Oxygen radicals and signaling Toren Finkel. Curr. Opin. Cell Biol. 10, 248–253 (1998).
5. Montine, T. J. et al. F 2 -Isoprostanes in Alzheimer and Other Neurodegenerative Diseases. Antioxid. Redox Signal. 7, 269–275 (2005).
6. Berliner, J. A. & Heinecke, J. W. The role of oxidized lipoproteins in atherogenesis. Free Radic. Biol. Med. 20, 707–727 (1996).
7. Hammad, L. A. et al. Elevated levels of hydroxylated phosphocholine lipids in the blood serum of breast cancer patients. Rapid Commun. Mass Spectrom. 23, 863–876 (2009).
8. Wu, R. P. et al. Nrf2 responses and the therapeutic selectivity of electrophilic compounds in chronic lymphocytic leukemia. Proc. Natl. Acad. Sci. U. S. A. 107, 7479–7484 (2010).
9. Wallick, S. A. & Sarkanen, K. V. Effect of pH on the autoxidation kinetics of vanillin. Wood Sci. Technol. 17, 107–116 (1983).
10. Litwinienko, G., Beckwith, A. L. J. & Ingold, K. U. The frequently overlooked importance of solvent in free radical syntheses. Chem. Soc. Rev. 40, 2157–2163 (2011).
11. Niki, E. Free radical initiators as source of water- or lipid-soluble peroxyl radicals. Methods Enzymol. 186, 100–108 (1990).
12. Noguchi, N. et al. 2,2'-azobis (4-methoxy-2,4-dimethylvaleronitrile), a new lipid-soluble azo initiator: Application to oxidations of lipids and low-density lipoprotein in solution and in aqueous dispersions. Free Radic. Biol. Med. 24, 259–268 (1998).
13. Yin, H., Xu, L. & Porter, N. A. Free radical lipid peroxidation: Mechanisms and analysis. Chem. Rev. 111, 5944–5972 (2011).
14. Bochkov, V. N. et al. Generation and biological activities of oxidized phospholipids. Antioxidants Redox Signal. 12, 1009–1059 (2010).
15. Babior, B. M. NADPH Oxidase: An Update. Blood 93, 1464–1476 (1999).
16. Turrens, J. F. Superoxide production by the mitochondrial respiratory chain. Biosci. Rep. 17, 3–8 (1997).
17. Finkel, T. & Holbrook, N. J. Oxidants, Oxidative Stress and Biology of Ageing. Nature 408, 239–247 (2000).

18. Porter, N. A., Caldwell, S. E. & Mills, K. A. Mechanisms of free radical oxidation of unsaturated lipids. Lipids 30, 277–290 (1995).

19. Blanksby, S. J. & Ellison, G. B. Bond dissociation energies of organic molecules. Acc. Chem. Res. 36, 255–263 (2003).

20. Pratt, D. A., Mills, J. H. & Porter, N. A. Theoretical calculations of carbon-oxygen bond dissociation enthalpies of peroxyl radicals formed in the autoxidation of lipids. J. Am. Chem. Soc. 125, 5801–5810 (2003).

21. Trenwith, A. B. Dissociation of 3-methylpenta-1, 4-diene and the resonance energy of the pentadienyl radical. J. Chem. Soc. Faraday Trans. 1 Phys. Chem. Condens. Phases 78, 3131–3136 (1982).

22. Egger, K. W. & Cocks, A. T. Homopolar and Heteropolar Bond Dissociation Energies and Heats of Formation of Radicals and Ions in the Gas Phase II. The relationship between structure and bond dissociation in organic molecules. Helv. Chim. Acta 56, 1537–1552 (1973).

23. Ingold, K. U. Inhibition of the autoxidation of organic substances in the liquid phase. Chem. Rev. 61, 563–589 (1961).

24. Yin, H. & Porter, N. A. New insights regarding the autoxidation of polyunsaturated fatty acids. Antioxidants Redox Signal. 7, 170–184 (2005).

25. Russell, G. A. Deuterium-isotope Effects in the Autoxidation of Aralkyl Hydrocarbons. Mechanism of the Interaction of Peroxy Radicals. J. Am. Chem. Soc. 79, 3871–3877 (1957).

26. Howard, J. A. & Ingold, K. U. The Self-Reaction of sec-Butylperoxy Radicals. Confirmation of the Russell Mechanism. J. Am. Chem. Soc. 90, 1056–1058 (1968).

27. Brigelius-Flohé, R. & Maiorino, M. Glutathione peroxidases. Biochim. Biophys. Acta - Gen. Subj. 1830, 3289–3303 (2013).

28. Christie, W. W. & Han, X. Lipids: their structures and occurrence. in Lipid Analysis 3–19 (Elsevier, 2012). doi:10.1533/9780857097866.3

29. Xu, L., Davis, T. A. & Porter, N. A. Rate constants for peroxidation of polyunsaturated fatty acids and sterols in solution and in liposomes. J. Am. Chem. Soc. 131, 13037–13044 (2009).

30. Reddy, R. D., Keshavan, M. S. & Yao, J. K. Reduced red blood cell membrane essential polyunsaturated fatty acids in first episode schizophrenia at neuroleptic-naive baseline. Schizophr. Bull. 30, 901–911 (2004).

31. Vásquez, V., Krieg, M., Lockhead, D. & Goodman, M. B. Phospholipids that Contain Polyunsaturated Fatty Acids Enhance Neuronal Cell Mechanics and Touch Sensation. Cell Rep. 6, 70–80 (2014).

32. Horrobin, D. F. The membrane phospholipid hypothesis as a biochemical basis for the neurodevelopmental concept of schizophrenia. Schizophr. Res. 30, 193–208 (1998).

33. Zielinski, Z. A. M. & Pratt, D. A. Lipid Peroxidation: Kinetics, Mechanisms, and Products. J. Org. Chem. 82, 2817–2825 (2017).

34. Matsumoto, A. & Higashi, H. Convenient synthesis of polymers containing labile bonds in the main chain by radical alternating copolymerization of alkyl sorbates with oxygen. Macromolecules 33, 1651–1655 (2000).

35. Howard, J. A. Absolute Rate Constants for Hydrocarbon Autoxidation. XXII. The Autoxidation of some Vinyl Compounds. Can. J. Chem. 50, 2298–2304 (1972).

36. Miyashita, K., Hara, N. & Fujimoto, K. Dimers Formed in Oxygenated Methyl Linoleate Hydroperoxides. 20, 578–587 (1985).

37. Dyer, J. M. et al. Molecular analysis of a bifunctional fatty acid conjugase/desaturase from tung. Implications for the evolution of plant fatty acid diversity. Plant Physiol. 130, 2027–2038 (2002).

38. Tsuzuki, T., Tokuyama, Y., Igarashi, M. & Miyazawa, T. Tumor growth suppression by α-eleostearic acid, a linolenic acid isomer with a conjugated triene system, via lipid peroxidation. Carcinogenesis 25, 1417–1425 (2004).

39. Beatty, A. et al. Conjugated linolenic fatty acids trigger ferroptosis in triple-negative breast cancer. bioRxiv (2019). doi:10.1101/556084

40. Li, B. & Pratt, D. A. Methods for determining the efficacy of radical-trapping antioxidants. Free Radic. Biol. Med. 82, 187–202 (2015).

41. Ingold, K. U. & Pratt, D. A. Advances in radical-trapping antioxidant chemistry in the 21st century: A kinetics and mechanisms perspective. Chem. Rev. 114, 9022–9046 (2014).

42. Poon, J. F. & Pratt, D. A. Recent Insights on Hydrogen Atom Transfer in the Inhibition of Hydrocarbon Autoxidation. Acc. Chem. Res. 51, 1996–2005 (2018).

43. Zilka, O. et al. On the Mechanism of Cytoprotection by Ferrostatin-1 and Liproxstatin-1 and the Role of Lipid Peroxidation in Ferroptotic Cell Death. ACS Cent. Sci. 3, 232–243 (2017).

44. Farmer, L. A., Haidasz, E. A., Griesser, M. & Pratt, D. A. Phenoxazine: A privileged scaffold for radical-trapping antioxidants. J. Org. Chem. 82, 10523–10536 (2017).

45. Pratt, D. A., Dilabio, G. A., Mulder, P. & Ingold, K. U. Bond strengths of toluenes, anilines, and phenols: To hammett or not. Acc. Chem. Res. 37, 334–340 (2004).

46. Lucarini, M., Pedrielli, P., Pedulli, G. F., Cabiddu, S. & Fattuoni, C. Bond dissociation energies of O-H bonds in substituted phenols from equilibration studies. J. Org. Chem. 61, 9259–9263 (1996).

47. Burton, G. W. & Ingold, K. U. Vitamin E: Application of the Principles of Physical Organic Chemistry to the Exploration of Its Structure and Function. Acc. Chem. Res. 19, 194–201 (1986).

48. Valgimigli, L. & Pratt, D. A. Maximizing the reactivity of phenolic and aminic radical-trapping antioxidants: Just add nitrogen! Acc. Chem. Res. 48, 966–975 (2015).

49. Jensen, R. K., Korcek, S., Zinbo, M. & Gerlock, J. L. Regeneration of Amine in Catalytic Inhibition of Oxidation. J. Org. Chem. 60, 5396–5400 (1995).

50. Haidasz, E. A., Shah, R. & Pratt, D. A. The catalytic mechanism of diarylamine radical-trapping antioxidants. J. Am. Chem. Soc. 136, 16643–16650 (2014).

51. Griesser, M. et al. The Catalytic Reaction of Nitroxides with Peroxyl Radicals and Its Relevance to Their Cytoprotective Properties. J. Am. Chem. Soc. 140, 3798–3808 (2018).

52. Li, J. et al. Ferroptosis: past, present and future. Cell Death Dis. 11, 88 (2020).

53. Majno, G. & Joris, I. Apoptosis, oncosis, and necrosis: An overview of cell death. Am. J. Pathol. 146, 3–15 (1995).

54. Vandenabeele, P., Galluzzi, L., Vanden Berghe, T. & Kroemer, G. Molecular mechanisms of necroptosis: An ordered cellular explosion. Nat. Rev. Mol. Cell Biol. 11, 700–714 (2010).

55. Leist, M., Single, B., Castoldi, A. F., Kühnle, S. & Nicotera, P. Intracellular Adenosine Triphosphate (ATP) Concentration: A Switch in the Decision Between Apoptosis and Necrosis. J. Exp. Med. 185, 1481–1486 (1997).

56. Dolma, S., Lessnick, S. L., Hahn, W. C. & Stockwell, B. R. Identification of genotype-selective antitumor agents using synthetic lethal chemical screening in engineered human tumor cells. Cancer Cell 3, 285–296 (2003).

57. Yagoda, N. et al. RAS–RAF–MEK-dependent oxidative cell death involving voltage-dependent anion channels. Nature 447, 865–869 (2007).

58. Yang, W. S. & Stockwell, B. R. Synthetic Lethal Screening Identifies Compounds Activating Iron-Dependent, Nonapoptotic Cell Death in Oncogenic-RAS-Harboring Cancer Cells. Chem. Biol. 15, 234–245 (2008).

59. Dixon, S. J. et al. Ferroptosis: An Iron-Dependent Form of Nonapoptotic Cell Death. Cell 149, 1060–1072 (2012).

60. Yamaguchi, Y., Kasukabe, T. & Kumakura, S. Piperlongumine rapidly induces the death of human pancreatic cancer cells mainly through the induction of ferroptosis. Int. J. Oncol. 52, 1011–1022 (2018).

61. Nie, J., Lin, B., Zhou, M., Wu, L. & Zheng, T. Role of ferroptosis in hepatocellular carcinoma. J. Cancer Res. Clin. Oncol. 144, 2329–2337 (2018).

62. Luo, M. et al. miR-137 regulates ferroptosis by targeting glutamine transporter SLC1A5 in melanoma. Cell Death Differ. 25, 1457–1472 (2018).

63. Sealy, W., Solano, R., Chen, L., Na, R. & Ran, Q. Redox Biology Ablation of ferroptosis regulator glutathione peroxidase 4 in forebrain neurons promotes cognitive impairment and neurodegeneration. Redox Biol. 12, 8–17 (2017).

64. Do Van, B. et al. Ferroptosis, a newly characterized form of cell death in Parkinson's disease that is regulated by PKC. Neurobiol. Dis. 94, 169–178 (2016).

65. Friedmann Angeli, J. P. et al. Inactivation of the ferroptosis regulator Gpx4 triggers acute renal failure in mice. Nat. Cell Biol. 16, 1180–1191 (2014).

66. Fang, X. et al. Ferroptosis as a target for protection against cardiomyopathy. Proc. Natl. Acad. Sci. U. S. A. 116, 2672–2680 (2019).

67. Shirlee Tan, B. S. P., David Schubert, B. S. P. & Pamela Maher, B. S. P. Oxytosis: A Novel Form of Programmed Cell Death. Curr. Top. Med. Chem. 1, 497–506 (2001).

68. Liu, Y. et al. The 5-lipoxygenase inhibitor zileuton confers neuroprotection against glutamate oxidative damage by inhibiting ferroptosis. Biol. Pharm. Bull. 38, 1234–1239 (2015).

69. Lewerenz, J., Ates, G., Methner, A., Conrad, M. & Maher, P. Oxytosis/Ferroptosis—(Re-) Emerging Roles for Oxidative Stress-Dependent Non-apoptotic Cell Death in Diseases of the Central Nervous System. Front. Neurosci. 12, (2018).

70. Marnett, L. J., Riggins, J. N. & West, J. D. Endogenous generation of reactive oxidants and electrophiles and their reactions with DNA and protein. J. Clin. Invest. 111, 583–593 (2003).

71. Kuhn, H., Banthiya, S. & Van Leyen, K. Mammalian lipoxygenases and their biological relevance. Biochim. Biophys. Acta - Mol. Cell Biol. Lipids 1851, 308–330 (2015).

72. Hadian, K. & Stockwell, B. R. SnapShot: Ferroptosis. Cell 181, 1188-1188.e1 (2020).

73. Conrad, M. & Pratt, D. A. The chemical basis of ferroptosis. Nat. Chem. Biol. 15, 1137–1147 (2019).

74. Haeggström, J. Z. & Funk, C. D. Lipoxygenase and leukotriene pathways: Biochemistry, biology, and roles in disease. Chem. Rev. 111, 5866–5896 (2011).

75. Lu, S. C. Glutathione synthesis. Biochim. Biophys. Acta - Gen. Subj. 1830, 3143–3153 (2013).

76. Lu, S. C. Regulation of glutathione synthesis. Mol. Aspects Med. 30, 42–59 (2009).

77. Lo, M., Wang, Y. Z. & Gout, P. W. The xc- cystine/glutamate antiporter: A potential target for therapy of cancer and other diseases. J. Cell. Physiol. 215, 593–602 (2008).

78. Dixon, S. J. et al. Pharmacological inhibition of cystine-glutamate exchange induces endoplasmic reticulum stress and ferroptosis. eLife 3, 1–25 (2014).

79. Wu, Z. et al. Chaperone-mediated autophagy is involved in the execution of ferroptosis. Proc. Natl. Acad. Sci. U. S. A. 116, 2996–3005 (2019).

80. Stockwell, B. R. et al. Ferroptosis: A Regulated Cell Death Nexus Linking Metabolism, Redox Biology, and Disease. Cell 171, 273–285 (2017).

81. Yang, W. S. et al. Regulation of Ferroptotic Cancer Cell Death by GPX4. Cell 156, 317–331 (2014).

82. Yang, W. S. et al. Peroxidation of polyunsaturated fatty acids by lipoxygenases drives ferroptosis. Proc. Natl. Acad. Sci. U. S. A. 113, E4966–E4975 (2016).

83. Doll, S. et al. ACSL4 dictates ferroptosis sensitivity by shaping cellular lipid composition. Nat. Chem. Biol. 13, 91–98 (2017).

84. Doll, S. et al. FSP1 is a glutathione-independent ferroptosis suppressor. Nature 575, 693–698 (2019).

85. Gao, M., Monian, P., Quadri, N., Ramasamy, R. & Jiang, X. Glutaminolysis and Transferrin Regulate Ferroptosis. Mol. Cell 59, 298–308 (2015).

86. Belkner, J., Wiesner, R., Kühn, H. & Lankin, V. Z. The oxygenation of cholesterol esters by the reticulocyte lipoxygenase. FEBS Lett. 279, 110–114 (1991).

87. Yang, W. S. & Stockwell, B. R. Ferroptosis: Death by Lipid Peroxidation. Trends Cell Biol. 26, 165–176 (2016).

88. Kagan, V. E. et al. Oxidized arachidonic and adrenic PEs navigate cells to ferroptosis. Nat. Chem. Biol. 13, 81–90 (2017).

89. Shintoku, R. et al. Lipoxygenase-mediated generation of lipid peroxides enhances ferroptosis induced by erastin and RSL3. Cancer Sci. 108, 2187–2194 (2017).

90. Brütsch, S. H. et al. Expression of inactive glutathione peroxidase 4 leads to embryonic lethality, and inactivation of the Alox15 gene does not rescue such knock-in mice. Antioxidants Redox Signal. 22, 281–293 (2015).

91. Seiler, A. et al. Glutathione Peroxidase 4 Senses and Translates Oxidative Stress into 12/15-Lipoxygenase Dependent- and AIF-Mediated Cell Death. Cell Metab. 8, 237–248 (2008).

92. Angeli, J. P. F., Shah, R., Pratt, D. A. & Conrad, M. Ferroptosis Inhibition: Mechanisms and Opportunities. Trends Pharmacol. Sci. 38, 489–498 (2017).

93. Carter, G. W. et al. 5-lipoxygenase inhibitory activity of zileuton. J. Pharmacol. Exp. Ther. 256, 929–37 (1991).

94. Sendobry, S. M. et al. Attenuation of diet-induced atherosclerosis in rabbits with a highly selective 15-lipoxygenase inhibitor lacking significant antioxidant properties. Br. J. Pharmacol. 120, 1199–1206 (1997).

95. Shah, R., Shchepinov, M. S. & Pratt, D. A. Resolving the Role of Lipoxygenases in the Initiation and Execution of Ferroptosis. ACS Cent. Sci. 4, 387–396 (2018).

CHAPTER 2 Beyond Lipoxygenase: Studying the Initiation of Ferroptosis

2.1 Introduction

Determining the primary source driving lipid peroxidation has remained of great interest since its causative relationship with ferroptotic cell death was identified.[1–4] Given the enzymatic role of lipoxygenase (LOX) centres around lipid hydroperoxide production, LOX remains a popular suspect.[2,5,6] LOX gene regulation (e.g. gene knockouts, RNA interference)[7] and pharmacological inhibition (i.e. LOX inhibitors)[6] of LOX enzymes have been shown to confer ferroptotic resistance; however, only purported LOX inhibitors have translated in animal models (i.e. GPX4$^{-/-}$ knockout mice).[8] As such, much of the evidence in support of a LOX-driven ferroptotic model is drawn from the study of LOX inhibitors.[2,4,6,9,10] However, this has become increasingly unconvincing given the off-target RTA effects commonly associated with LOX inhibitors capable of cell rescue.[11] For example, RTA liproxstatin-1 (Lip-1), which was previously identified as a high-affinity 15-LOX inhibitor through molecular modelling,[6] prevents ferroptosis at much lower concentrations than it suppresses LOX activity, suggesting its RTA activity is the primary source of its cytoprotective effect.[12] In fact, no individual LOX isoform has been implicated in the initiation of ferroptosis to date.[7,8,13]

In 2018, Shah, R., et al. published results demonstrating that the ability of LOX inhibitors to rescue cells is directly tied to their RTA activity, indicating their inhibitory effects are not due to enzyme interaction, but their peroxyl-trapping abilities.[14] Therein, a library of RTAs, redox-active LOX inhibitors, and redox-inactive LOX inhibitors was screened in human embryonic kidney (HEK-293) cells transfected to overexpress 5-LOX, p12-LOX, and 15-LOX-1. Screened RTAs comprised nature's best, α-TOH, renowned for its lipid peroxidation inhibition,[15] alongside compounds identified for their powerful RTA abilities in cells (**Figure 2.1A**). Liproxstatin-1[7] (Lip-1) and ferrostatin-1[16] (Fer-1) are potent RTA ferroptotic inhibitors identified in high-throughput screens soon following the discovery of ferroptosis. Although purported as inhibitors of 15-LOX-1, the antioxidative abilities of Lip-1 and Fer-1 flourish in the lipophilic environments of cell membranes with inhibition of lipid peroxidation overshadowing their comparably poor 15-LOX-1 inhibition.[12] In addition, C_{15}-THN (i.e. tetrahydronaphthyridinol), an aza-analog of α-TOH, and pentamethyl-6-chromanol (PMC), a truncated α-TOH analog lacking its aliphatic side chain, were included as potent designer-RTAs with established anti-ferroptotic effects.[14,17] Included as redox-active LOX inhibitors were pan-LOX inhibitor NDGA and 5-LOX inhibitor zileuton,[18] known for their associated RTA activity and ability to prevent lipid oxidation,[11] as well as, 15-LOX-1 inhibitor PD146176[19], providing a scope of LOX isoform specificity (**Figure 2.1B**). Lastly, two redox-inactive 5-LOX inhibitors were also screened, CAY10649 and CJ-13619 (**Figure 2.1C**).[14]

In sum, Shah, R., et al. (2018) exhibited that only redox-active 'antioxidants' were effective inhibitors of ferroptosis and redox-inactive compounds were ineffective, regardless of any inherent LOX inhibitory activity. Cytoprotection from redox-active LOX inhibitors was comparable to that of RTAs, and more importantly independent of LOX expression, with similar potencies in 5-LOX, p12-LOX, and 15-LOX-1 HEK-293 overexpressing isoforms. Should LOX be a necessary source for lipid-peroxyl production, LOX-specific inhibitors such as 5-LOX inhibitor zileuton would be expected to have a pronounced inhibitory effect in 5-LOX overexpressing cells, which was not the case.

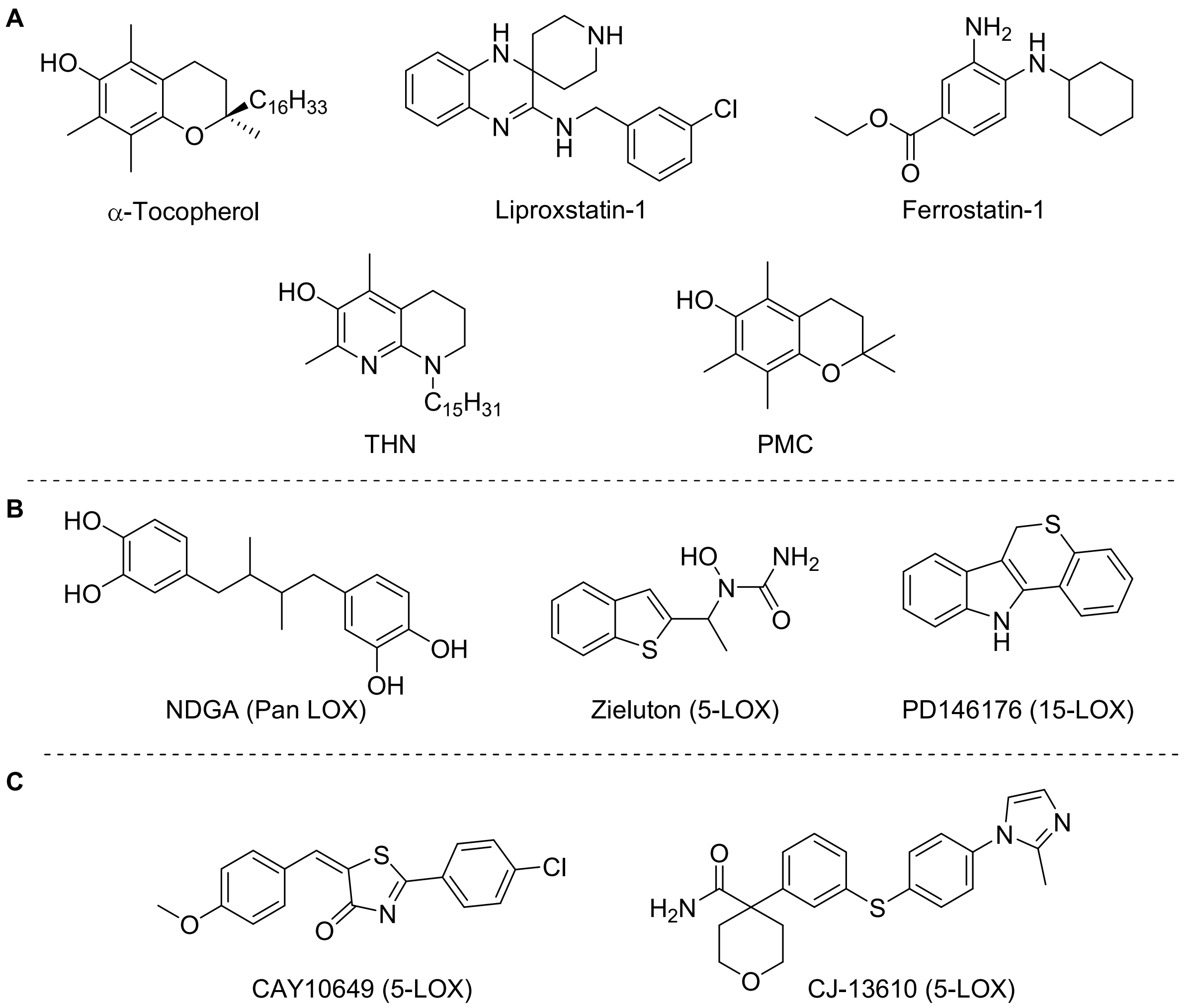

Figure 2.1 Inhibitory compounds previously screened using HEK-293 cells,[14] including RTAs (**A**), redox-active LOX inhibitors (**B**), and redox-inactive LOX inhibitors (**C**). Specific LOX isoforms affected are noted accordingly.

The importance of RTA activity in ferroptotic inhibitors was further exemplified in the α-TOH analog α-TOMe, *O*-methylated at its otherwise redox-active H-atom site (**Figure 2.2**). α-TOH has been postulated as a 15-LOX-1 inhibitor, and its cytoprotective effects credited to its obstruction of the LOX active site by insertion of its lipophilic side chain.[6] However, not only was α-TOH inhibition uniform across cell lines overexpressing various LOX isoforms, but methylation at the labile H-atom site suppressed the cytoprotective effects of α-TOH (now α-TOMe).

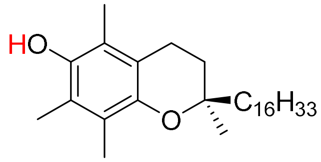

α-TOH

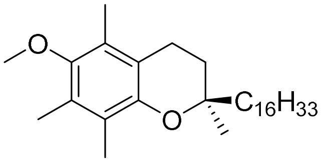

α-TOMe

	IC_{50} (μM)	
	α-TOH	α-TOMe
HEK-293	4.8	>10
+ 5-LOX	4.6	>10
+ 12-LOX	5.2	>10
+ 15-LOX-1	3.7	>10

Figure 2.2 Structures and IC_{50} results for α-TOH and its methylated analog α-TOMe in natural and transfected LOX overexpressing HEK-293 cells.[14]

Our 2018 work in HEK-293 cells provided evidence discrediting the role LOX play in ferroptosis; however, there are limitations in its scope. Although cells overexpressing 5-LOX, p12-LOX, and 15-LOX-1 are studied, the library of screened compounds lacks p12-LOX redox-active/inactive and 15-LOX-1 redox-inactive inhibitors. For a truly robust screen, both redox-active and inactive isoform-specific LOX inhibitors should be included for all LOX tested. In addition, the study was limited to transfected HEK-293 cells – the results of which are less convincing than reporting on rigorously-studied ferroptotic models (e.g. HT-1080 cells). To confirm our initial findings regarding the contribution of LOX isoforms towards ferroptosis, a more thorough screen of LOX inhibitors in model ferroptosis cell lines was required.

Herein, we expand on the foregoing transfected HEK-293 cell work to assess the ability of RTAs and both redox-active and redox-inactive LOX inhibitors to subvert ferroptosis, using a bolstered cytoprotective library incorporating p12-LOX and 15-LOX-1 isoform-specific inhibitors, screened in mouse neuronal hippocampal (HT-22) and human fibrosarcoma (HT-1080) cells. HT-22 cells were initially reported to overexpress p12-LOX; however, this finding was substantiated by rescue using redox-active LOX inhibitors prior to our current understanding.[20] In fact, HT-22 cells have more recently been shown to instead predominantly express 15-LOX-2, verified by western blotting.[21] The 15-LOX-2 isoform was unexplored in our previous study, allowing us further opportunity to expand our project scope.

The HT-22 lineage is a derivative of immortalized HT-4 hippocampal cells, identified as a clone particularly sensitive to glutamate toxicity.[22] This glutamate-induced cell death, coined 'oxytosis', is a cell death modality not unlike ferroptosis, used as a model for oxidative stress in neurodegeneration.[23] HT-22 sensitivity results from its lack of ionotropic glutamate receptors, which limit the ability of HT-22 cells to modulate extracellular glutamate concentrations – an ideal model for ferroptosis.[24] An abundance of extracellular glutamate inhibits x_c^- cystine uptake (**Section 1.2.1.1)**, disrupting downstream GPX4 function and ultimately leading to cell death.[20] Studying glutamate-induced 'oxytosis' in tandem with ferroptosis allows us an additional model with which to measure the contribution of LOX towards oxidative stress (completed by lab member Katie Shirley).

HT-1080 cells are a robust ferroptotic model; used extensively in the study of ferroptosis, HT-1080 is the lineage in which ferroptosis was first characterized.[1,25,26] HT-1080 cells naturally express elevated levels of multiple LOX isoforms, of which 15-LOX-2 and eLOX-3 are consistently prevalent.[4] eLOX-3 however, does not form lipid hydroperoxides and instead catalyzes the formation of epoxyalcohol and epoxyketone derivatives, allowing us to study 15-LOX-2 as the sole overexpressed LOX contributing to lipid peroxidation.[27] The historical significance and 15-LOX-2 expression of the HT-1080 lineage make it an ideal candidate to evaluate alongside our HT-22 screen and corroborate our lab's previous HEK-293 studies.

Alongside the evaluation of RTAs, redox-active LOX inhibitors, and redox-inactive LOX inhibitors we sought to investigate the activity of necrostatin derivatives as ferroptosis inhibitors. Necrostatin-1 (Nec-1) was initially identified as an inhibitor of necroptosis – a regulated cell death pathway characterized by plasma membrane disruption and leakage of cellular contents.[28] As per its primary function, Nec-1 is a potent receptor-interacting serine/threonine-protein kinase 1 (RIPK1) inhibitor which prevents necroptosis by inhibiting RIPK1 enzymatic interaction and phosphorylation with RIPK3.[29] This RIPK1-RIPK3 interaction is necessary to form the multiprotein 'necroptosis-signaling complex' – or necrosome – which then stimulates necroptosis.[28] In addition to anti-necroptotic function, Nec-1 has been identified as having off-target anti-ferroptotic activity at high concentrations, exemplified by the rescue of GPX4$^{-/-}$ knockout cells from cell death.[1,7] This anti-ferroptotic activity occurs via a mechanism unrelated to RIPK1 inhibition, validated by rescue of RIPK1$^{-/-}$ knockout cells with Nec-1, through a mechanism yet to be explained.[7] To date, necrostatin(s) anti-ferroptotic properties remain understudied and poorly understood.[30] In the pursuit of elucidating the relationship between Nec-1 and ferroptosis, we sought to further characterize the activity of a subset of necrostatin analogs, employing several chemical and biological methods (**Figure 2.3**).

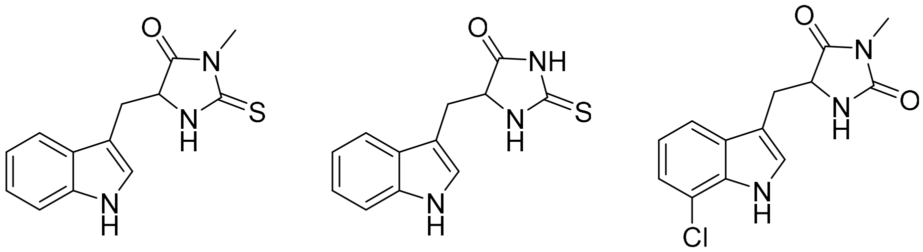

Nec-1 Nec-1i Nec-2

Figure 2.3 Chemical structure of necroptosis inhibitors necrostatin-1 (Nec-1), necrostatin-1i (Nec-1i), and necrostatin-2 (Nec-2).

2.2 Results

To examine the role LOX enzymes play in ferroptosis, we devised a library of compounds cytoprotective towards ferroptosis, including many from our lab's 2018 work[14] for direct comparison to the HEK-293 lineage and containing a diverse range of targets and functions. Our updated library was bolstered with 15-LOX-2 inhibitors, given HT-22 and HT-1080 cells' purported overexpression of 15-LOX-2, and redox-inactive inhibitors of p12-LOX and 15-LOX-1 which were absent from our HEK-293 library. The screened compounds can be differentiated into three distinct categories: RTAs, redox-active LOX inhibitors, and redox-inactive LOX inhibitors (**Figure 2.4**). As in our lab's previous work, the screened RTAs included α-TOH, Lip-1, Fer-1, C_{15}-THN, and PMC. When selecting redox-active LOX inhibitors, p12-LOX/15-LOX-1 inhibitor baicalein[31] was included alongside the previously-screened pan-LOX inhibitor NDGA for their non-specific inhibitory activity. Similarly, zileuton[18] (5-LOX) and PD146176[19] (15-LOX-1) were included from the HEK-293 library, with ML351[32] (15-LOX-1) and ML355[33] (p12-LOX) added to provide additional isoform-specific scope.

In contrast to the previously screened redox-inactive 5-LOX inhibitors CAY10649 and CJ-13619, in our screen we selected β-thujaplicin[34] (p12-LOX), ML094[32] (15-LOX-1), and in particular, ML545091,[35] MLS000327186,[36] and MLS000327069[36] for 15-LOX-2, the LOX isoform predominantly expressed in both our cell lines. By contrasting the cytoprotective effects of redox-active and redox-inactive compounds we hoped to clarify the role radical-trapping ability plays in the prevention of ferroptosis.

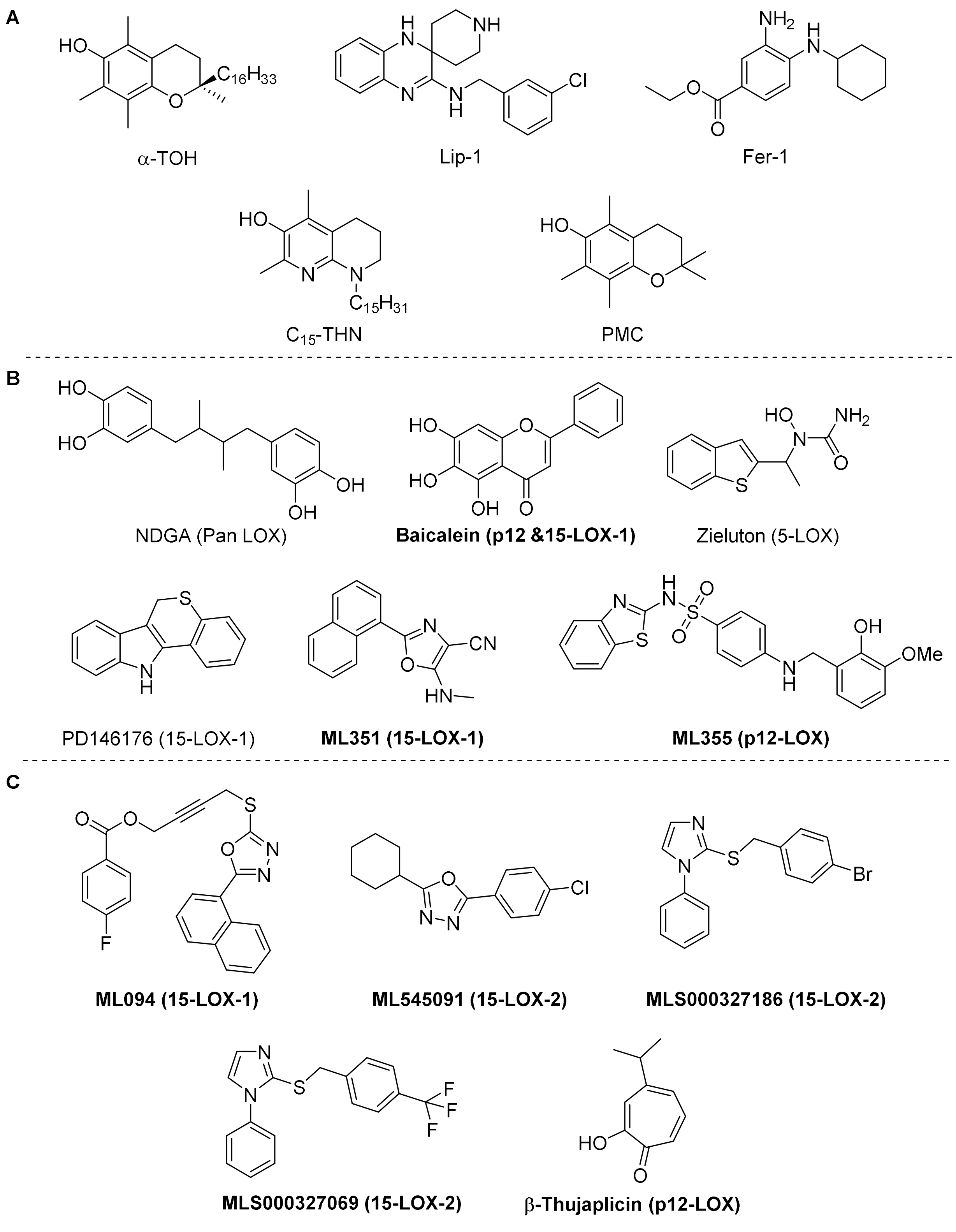

Figure 2.4 Chemical structures of screened inhibitory compounds, including RTAs (**A**), redox-active LOX inhibitors (**B**), and redox-inactive LOX inhibitors (**C**). Specific LOX isoforms affected are noted accordingly, compounds not previously included in HEK-293 screen are in bold.

2.2.1 Inhibition of RSL3-Induced Ferroptosis in HT-22 Cells

In order to assess the efficacy of the test compounds, cells were treated with (1*S*,3*R*)-RSL3, the archetype GPX4 inhibitor.[25] RSL3 is a small molecule inhibitor capable of inducing ferroptotic cell death; covalently binding to the selenocysteine residue of GPX4 and irreversibly inhibiting the enzyme directly involved in reduction of lipid hydroperoxides.[4,26] Cell viability was assessed by fluorescence using AquaBluer^{TM} (Multitarget Pharmaceuticals, LLC) which is reduced by viable cells from its nonfluorescent (blue) form to its fluorescent (red, $\lambda_{ex/em}$ = 540/590 nm) form.

In HT-22 cells, median lethal dose (LD_{50}) of RSL3 was found to be 0.38 μM after 4 hours, shown in **Figure 2.5A.** When assaying test compounds, a RSL3 concentration of 0.80 μM was used to ensure cells completely underwent ferroptosis after a 4 hour treatment of RSL3 in the absence of inhibitor. By adding test compounds in conjunction with RSL3 treatment, cell rescue could then be assessed relative to a control population of entirely ferroptotic cells.

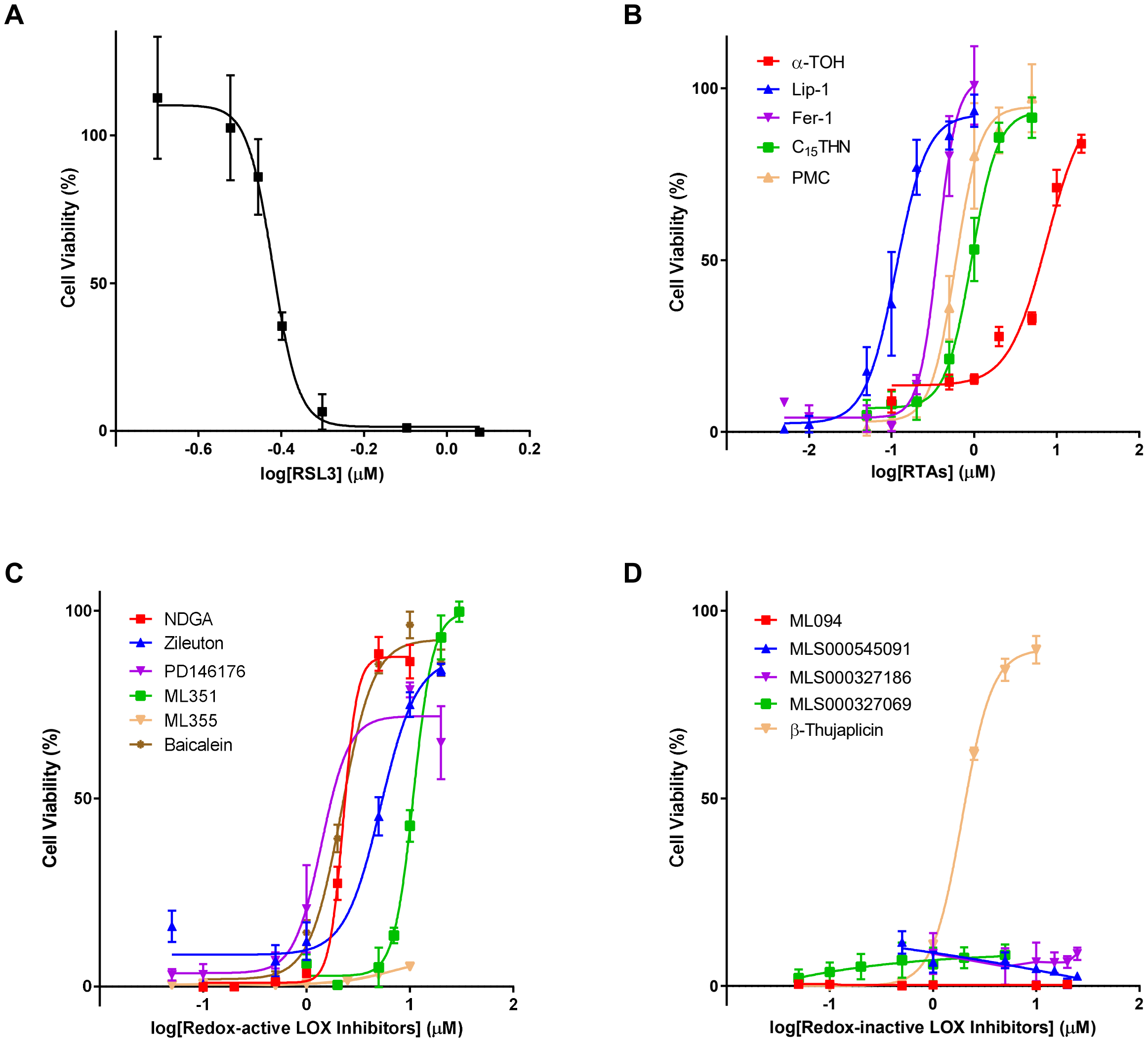

Figure 2.5 Ferroptosis induction and inhibition in HT-22 cells. Sensitization of cells to RSL3 treatment (**A**) and dose-response curves to cells treated with 0.80 μM RSL3 and varying concentrations of RTAs (**B**), redox-active LOX Inhibitors (**C**), and redox-inactive LOX inhibitors (**D**) over a 4 hour exposure, cell viability was assessed using AquaBluer treatment. IC_{50} values reported in **Table 2.1**.

Treatment of HT-22 cells with lipophilic RTAs provided complete rescue from ferroptosis at sufficient inhibitor concentrations (**Figure 2.5B**). α-TOH, nature's best RTA, required the highest median inhibitory concentration (IC_{50}) of 7.6 μM. In contrast, designer α-TOH-based RTAs C_{15}-THN and PMC showed rescue an order of magnitude greater than their α-TOH, at 0.93 and 0.59 μM, respectively. Known ferroptosis inhibitors Lip-1 and Fer-1 possessed greater-still inhibitory function at 0.11 and 0.36 μM, respectively.

Screening redox-active LOX inhibitors showed a similar trend in rescue activity. NDGA, baicalein, zileuton, PD146176, and ML351 all demonstrated comparable IC_{50} (within an order of magnitude), ranging from 1.4 to 11 μM (**Figure 2.5C**). Whilst these compounds grant similar inhibitory effects In HT-22 cells, they possess diverse isoform specificity. One redox-active LOX inhibitor which did not possess observable rescue activity was ML355. Although a slight upward trend in cell viability was observed at the highest treated concentrations of ML355, rescue could not be confirmed as the compound was insufficiently soluble to treat cells with concentrations exceeding 10 μM.

The redox-inactive 15-LOX-1 inhibitor ML091 and 15-LOX-2 inhibitors MLS000545091, MLS000327186, and MLS000327069 showed no rescue activity (**Figure 2.5D**) but much to our initial surprise, p12-LOX inhibitor β-thujaplicin showed complete cell rescue with good potency (IC_{50} = 1.9 μM). Interestingly, β-thujaplicin was recently reported to possess excellent chelating ability towards Fe^{2+} and Fe^{3+}, iron cations necessary for the initiation of ferroptosis.[37] Considering this off-target activity of β-thujaplicin, we have yet to identify a ferroptosis inhibitor characterized solely by LOX inhibitory activity.

2.2.2 Inhibition of RSL3-Induced Ferroptosis in HT-1080 Cells

Suppression of RSL3-induced ferroptosis in HT-1080 cells showed very similar trends. HT-1080 cells were found to be slightly less sensitive to RSL3, with LD_{50} = 0.75 μM for a 4 hour incubation period (**Figure 2.6A**). As with the previous experiments in HT-22 cells, HT-1080 cells were treated with a higher concentration (2.0 μM) to ensure complete induction of ferroptosis after the 4 hour treatment period. Inhibition was assessed using an identical method to that used for HT-22 cells to facilitate comparison between results.

RTAs were able to completely rescue HT-1080 cells under the assay conditions, with the same IC_{50} trend previously observed in HT-22 cells (**Figure 2.6B**). α-TOH rescued cells with a calculated IC_{50} of 1.4 μM, with designer analogs C_{15}-THN and PMC rescuing at an order of magnitude higher potency (0.27 and 0.29 μM, respectively). Fer-1 showed improved potency (IC_{50} = 0.18 μM), while Lip-1 showed a marked improvement over Fer-1 (IC_{50} = 0.028 μM), a difference which was less pronounced in HT-22 cells. In all cases, inhibitors were found to have improved potency in HT-1080 cells when compared to HT-22 cells.

Redox-active LOX inhibitors NDGA, baicalein, zileuton, and PD146176, and ML351 again demonstrated comparable IC_{50} amongst themselves, ranging from 0.93 to 6.3 μM in magnitude (**Figure 2.6C**). In contrast to their diverse LOX inhibitory functionalities, these redox-active compounds share a trend of rescue ability similar to that observed in HT-22 cells. We were pleased to find ferroptotic rescue by ML355 was observed in HT-1080 cells, establishing the ability of the redox-active LOX inhibitor to rescue cells, previously unclear in HT-22 cells. Cell rescue was insufficient to calculate a true IC_{50} value, again given its limited solubility; however, by extrapolating the observed response, an IC_{50} value (34 μM) was estimated and has been included as a numerical representation of ML355 ferroptotic inhibition.

Lastly, treatment of HT-1080 cells with each of the four redox-inactive 15-LOX-1 and 15-LOX-2 inhibitors showed no indication of rescue from ferroptotic cell death (**Figure 2.6D**). Analogous to the HT-22 screen, p12-LOX inhibitor (and iron chelator) β-thujaplicin was able to fully rescue HT-1080 cells (IC_{50} = 1.5 μM). As in HT-22 cells, we were unable to identify a LOX inhibitor capable of inhibiting ferroptosis without off-target rescue activity.

IC_{50} values collected from both HT-22 and HT-1080 dose-response curves are compiled in **Table 2.1**; complementary results from glutamate- (HT-22) and erastin- (HT-1080) induced cell death collected by lab member Katie Shirley have also been included (although some RTAs studied in glutamate- and erastin-induced models had incomplete rescue (IR), activity was still observed). Aside from the aforementioned solubility-limited results for ML355, any compounds capable of rescuing cells from ferroptosis were found to do so in both cell lines. In addition, rescue was only facilitated by LOX inhibitors also possessing off-target RTA activity (or iron-chelating activity in the case of β-thujaplicin). The remaining four redox-inactive LOX-inhibitors were incapable of rescuing cells from either line. Notably, in almost all cases compounds were more effective at rescuing HT-1080 cells from ferroptosis; although the ability of a specific compound to rescue cells from ferroptosis was not found to be cell-line-dependent, the potency at which inhibitors were effective varied as a whole.

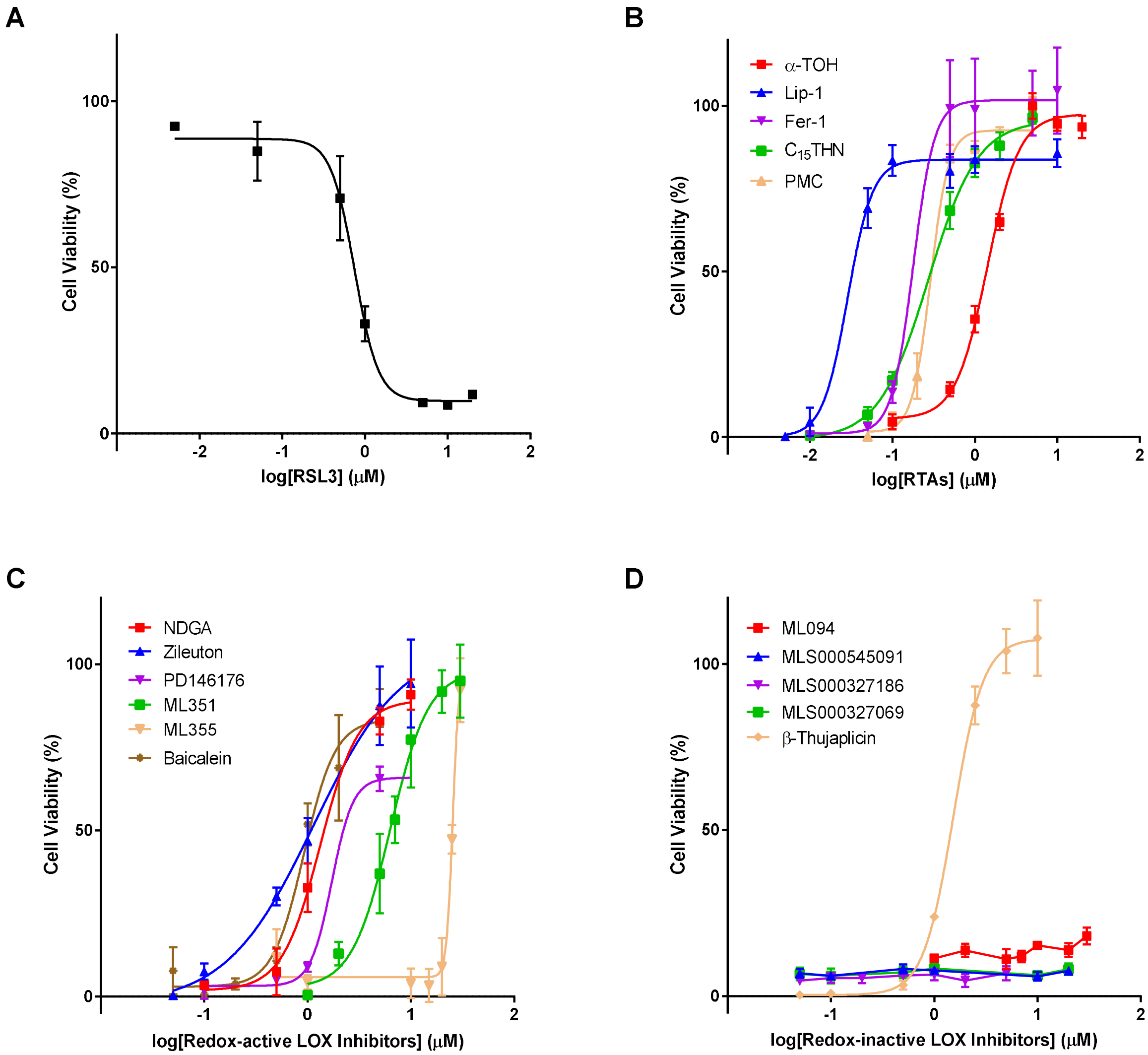

Figure 2.6 Ferroptosis induction and inhibition in HT-1080 cells. Sensitization of cells to RSL3 treatment (**A**) and dose-response curves to cells treated with 2.0 μM RSL3 and varying concentrations of RTAs (**B**), redox-active LOX Inhibitors (**C**), and redox-inactive LOX inhibitors (**D**) over a 4 hour exposure, cell viability was assessed using AquaBluer treatment. IC_{50} values reported in **Table 2.1**.

Table 2.1 IC$_{50}$ values for RTA and LOX inhibitor compounds in HT-22 and HT-1080 cells undergoing ferroptosis. Lab Member Katie Shirley's IC$_{50}$ results for corresponding glutamate and erastin cytotoxicity assays are included for comparison.

			IC$_{50}$ (μM)			
			RSL3		Glutamate	Erastin
		LOX Isoform Specificity	HT-22	HT-1080	HT-22	HT-1080
RTAs	α-TOH	-	7.6	1.4	0.11	0.32
	Lip-1	-	0.11	0.028	0.080	0.046
	Fer-1	-	0.36	0.18	0.45	0.13
	C$_{15}$-THN	-	0.93	0.27	0.090	0.045
	PMC	-	0.59	0.29	0.81	0.083
Redox-active LOX inhibitors	NDGA	Pan LOX	2.3	1.3	2.6	1.7
	Zileuton	5-LOX	5.3	1.2	2.5	2.8
	PD146176	15-LOX-1	1.4	1.7	1.5	IR
	ML351	15-LOX-1	11	6.3	3.4	IR
	ML355	p12-LOX	NR	34*	IR	IR
	Baicalein	Pan LOX	2.2	0.93	IR	IR
Redox-inactive LOX inhibitors	ML094	15-LOX-1	NR	NR	NR	NR
	MLS00054091	15-LOX-2	NR	NR	NR	NR
	MLS000327186	15-LOX-2	NR	NR	NR	NR
	MLS000327069	15-LOX-2	NR	NR	NR	NR
	β-Thujaplicin	p12-LOX	1.9	1.5	2.1	0.063

NR = no rescue; IR = incomplete rescue; *Estimated value, rescue insufficient to generate an IC$_{50}$

2.2.3 Investigations into the Effects of Protocol Modification

Several manipulations were made to the RSL3/inhibitor treatment protocol to investigate potential effects extrinsic factors may have played in the effectiveness of inhibitors. Lab member Katie Shirley induced cell death in HT-22 cells via glutamate toxicity and observed that in order to sensitize cells to ferroptosis, cells must be cultured without L-glutamine (L-Gln) during experimentation (**Figure 2.17**). Glutamate and glutamine share a well known relationship (i.e. the glutamate-glutamine cycle[38]); however, we sought to test if removing L-Gln from cell media during RSL3-induced ferroptosis impacted the dose-response of inhibitors. In doing so, we could determine if a L-Gln/RSL3 dependence exists, while assessing the validity of contrasting results between (+)L-Gln-RSL3- and (-)L-Gln-glutamate-induced ferroptosis. After assaying RTA inhibitors Lip-1 and Fer-1, we are pleased to report no sizable change in RSL3-treated rescue using media lacking L-Gln (**Figure 2.7A** and **B**). A minimal shift occurs in calculated IC_{50}, L-Gln is certainly not affecting rescue activity by any order of magnitude (16-29%), and no statistically significant change in sensitivity could be observed for Lip-1 (**Figure 2.7C**).

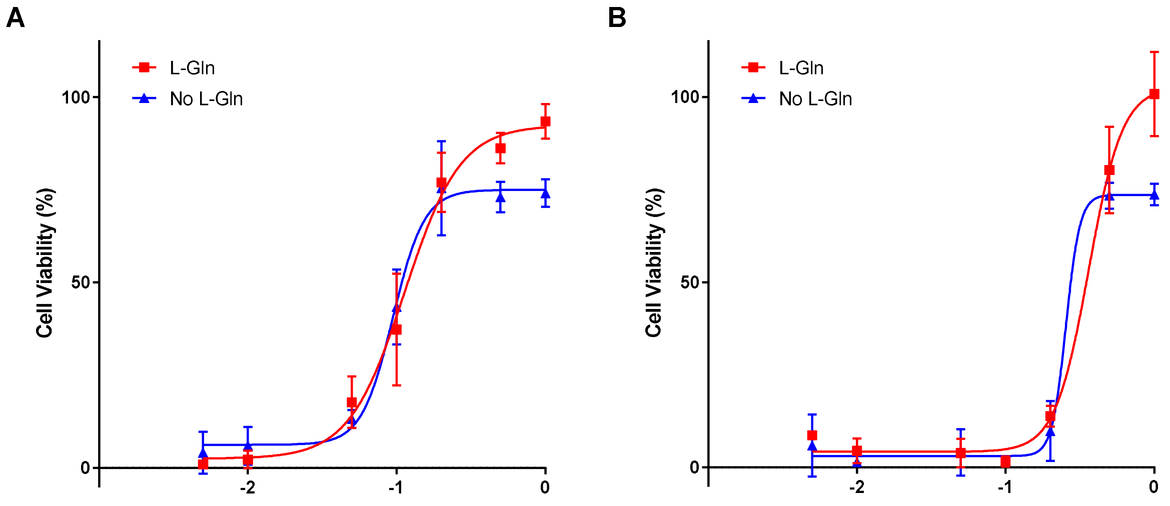

C

	IC_{50} (μM)			95% CI	
	L-Gln	No L-Gln	% Difference	L-Gln	No L-Gln
Lip-1	0.11	0.094	16%	[0.093, 0.138]	[0.080, 0.108]
Fer-1	0.36	0.25	29%	[0.308, 0.427]	†

† Insufficient data for a prediction of CI

Figure 2.7 Difference in dose-response in HT-22 cells cultured with and without L-Gln, treated with 0.80 μM RSL3 and varying concentrations of Lip-1 (**A**) and Fer-1 (**B**), and their corresponding results (**C**).

Contrasting cell rescue (IC_{50}) from RSL3-induced ferroptosis and either erastin- or glutamate-induced ferroptosis also indicated that cells were sometimes rescued from the latter at improved potencies, most significantly in the case of α-TOH and C_{15}-THN (**Table 2.2, Figure 2.19**). We surmised that this difference may be explained by the increased induction times upon erastin and glutamate treatment (24 hours) combined with the low solubility of these substrates. If α-TOH and C_{15}-THN required longer incubation times to permeate media and cell membranes to establish cytoprotection, perhaps incubating cells in the presence of the RTAs for comparable time periods would provide similar protection from RSL3-induced ferroptosis. α-TOH and C_{15}-THN were incubated for an additional 20 hours before addition of RSL3 (for a total of 24 hours) in both HT-22 and HT-1080 cell lines to mimic the incubation period of erastin and glutamate experiments. In all cases, lengthening the period of RTA incubation did improve rescue activity from RSL3-induced cell death (**Figure 2.8A-D**). A 24 hour incubation of C_{15}-THN in HT-22 cells did show cellular toxicity at higher concentrations, however sufficient data was available to plot a dose-response for 1 μM and below. This toxicity was observed in HT-1080 cells as well, but at concentrations exceeding the plotted dose-response. A shift in cytoprotection for α-TOH and C_{15}-THN was observed in both cell lines. α-TOH showed the greatest improvement, increasing in potency by more than an order of magnitude (95 and 93% difference in HT-22 and HT-1080 cells, respectively, **Figure 2.8E**). The shift in C_{15}-THN rescue was less pronounced (<50% difference) but rescue still improved with incubation. Thus, prolonged incubation of α-TOH in RSL3-treatments provided comparable rescue to glutamate-/erastin-treated cells, however the observed shift was insufficient in C_{15}-THN to rescue cells at the inhibitor concentrations observed with glutamate/erastin.

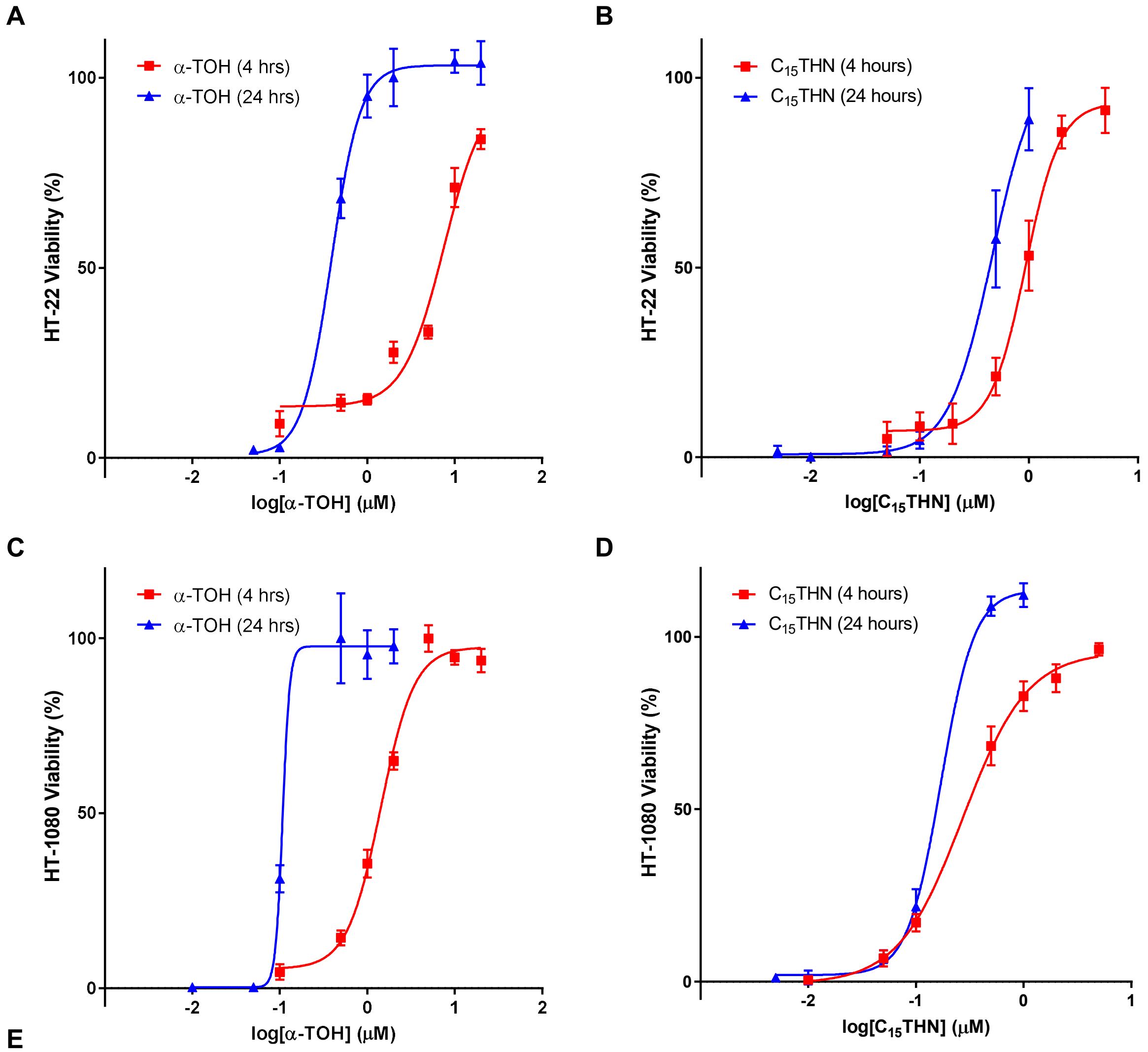

E

	IC_{50} (μM) α-TOH			IC_{50} (μM) C_{15}THN		
	4 hrs	24 hrs	% Diff	4 hrs	24 hrs	% Diff
HT-22	7.6	0.39	95	0.93	0.46*	50
HT-1080	1.4	0.11	93	0.27	0.17	37

*Estimated value, rescue insufficient to generate an IC_{50}

Figure 2.8 Difference in dose-response when varying RTA incubation time from 4 to 24 hours in HT-22 and HT-1080 cells treated with 0.80 μM and 2.0 μM RSL3, respectively, and varying concentrations of α-TOH (**A** (HT-22) and **C** (HT-1080)) and C_{15}THN (**B** (HT-22) and **D** (HT-1080)), and their corresponding results (**E**).

2.2.4 Inhibition of Ferroptosis by Necrostatins

As part of the foregoing assays of ferroptotic inhibition by RTAs and LOX inhibitors, we tested necrostatin-1 (Nec-1), a necroptosis and RIPK1 inhibitor. Nec-1 has been previously identified as having off-target anti-ferroptotic activity at high concentrations.[7] Testing the efficacy of Nec-1 to rescue cells from RSL3-induced cell death showed considerably more effective rescue in HT-1080 cells (44 μM) compared to HT-22, which were not able to be fully rescued (estimated $IC_{50} = 1.5 * 10^2$ μM, **Figure 2.20**) leading us to pursue the investigation solely in HT-1080 cells (**Figure 2.9**) Even still, the rescue activity in HT-1080 cells required high concentrations of Nec-1, with complete rescue only achieved at $3.0 * 10^2$ μM.

Given the off-target nature of Nec-1 cytoprotection, we selected two common necrostatin analogs, its inactive control necrosatin-1i (Nec-1i) and Cl-analog necrostatin-2 (Nec-2) to broaden our study (**Figure 2.9A**). Our hope was that including the inactive control of Nec-1 would help confirm the off-target nature of the anti-ferroptotic activity. Presumably if the RIPK1 inhibitory effects of necrostatin compounds were unrelated to its cytoprotection, the inactive control and analogs could have comparable rescue activity. Assaying Nec-1i and Nec-2, both compounds showed remarkably similar rescue, with estimated IC_{50} values of $1.7 * 10^2$ and $2.0 * 10^2$ μM (**Figure 2.9B,C**). Similar in trend to the Nec-1 rescue in HT-22 cells, rescue is incomplete for Nec-1i and Nec-2 at a concentration of $3.0 * 10^2$ μM in HT-1080 cells, with solubility as a limiting factor. Regardless, the trends indicate that the rescue ability of Nec-1i and Nec-2 is only slightly below that of Nec-1 – indicating an off-target effect.

Given our previous findings correlating the RTA and anti-ferroptotic activity of cytoprotective compounds, we wondered if the rescue activity displayed by necrostatin(s) could be attributed to their ability to act as RTAs. Structurally, necrostatin(s) possesses two nitrogen-bound H-atoms (three in the case of Nec-1i), one within each of its indole and (thio)hydantoin moieties. Sufficient HAT at these sites facilitating weak RTA activity could provide an explanation for the rescue activity observed.

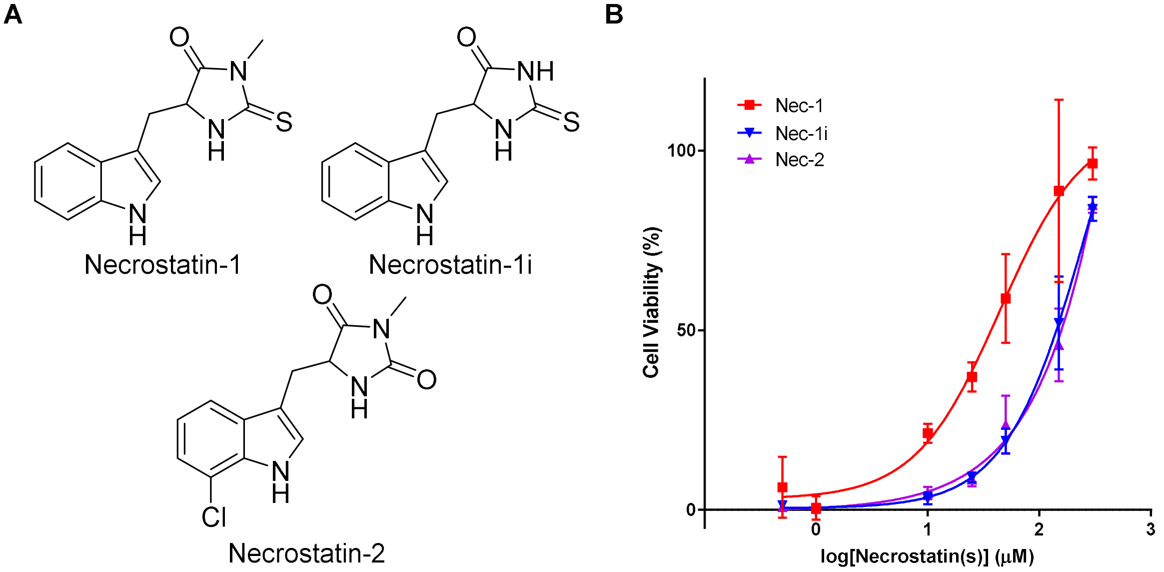

C

	IC50 (μM)		
	Nec-1	Nec-1i	Nec-2
HT-1080	44	1.7 * 10^2*	2.0 * 10^2*
HT-22	1.5 * 10^2*	nd	nd

*Estimated value, rescue insufficient to generate an IC_{50}; nd = no data

Figure 2.9 Results of necrostatin screen. Structures of Nec-1, Nec-1i, and Nec-2 (**A**), ferroptosis induction and inhibition in HT-1080 cells treated with 2.0 μM RSL3 and varying concentrations of inhibitor (**B**), and their corresponding results, contrasted to results in HT-22 cells (**C**). HT-22 data included in table in Appendix.

Using our established approach for determining RTA efficacy,[39] the necrostatin compounds were assessed for activity in organic and lipophilic environments. The method consists of a co-autoxidation of styrene-conjugated 4,4-difluoro-4-bora-3*a*,4*a*-diaza-*s*-indacene (STY-BODIPY) with either cumene or the polyunsaturated lipids of egg phosphatidylcholine liposomes. Oxidation of STY-BODIPY disrupts its absorption at λ_{max} = 565 nm and fluorescence at λ_{max} = 620 nm, allowing the autoxidation reaction to be tracked by loss of absorbance or fluorescence in real-time by spectrophotometry (**Figure 2.10A**). The test RTA is subsequently added and the reaction is monitored for any retardation in the rate of autoxidation.

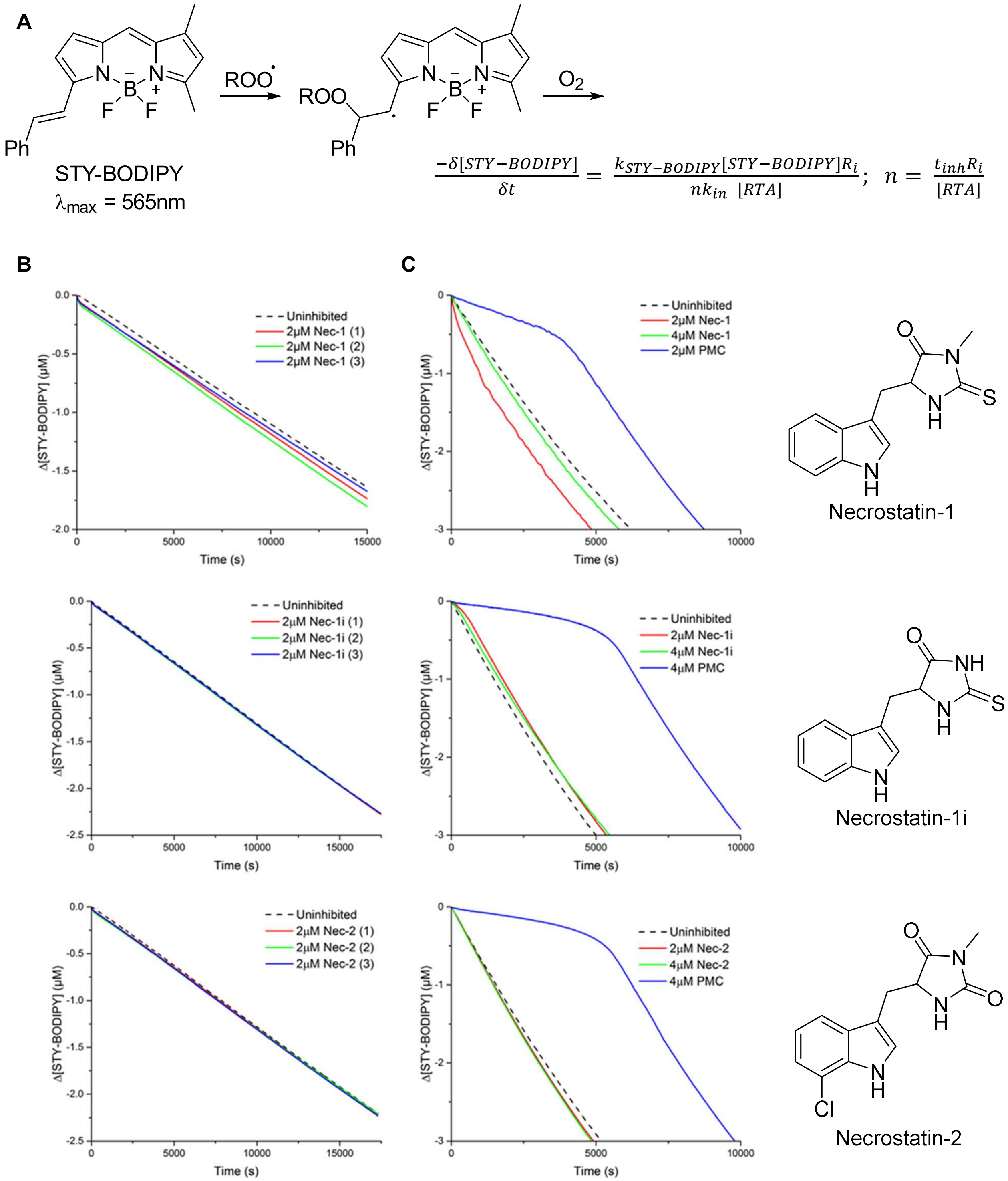

$$\frac{-\delta[STY-BODIPY]}{\delta t} = \frac{k_{STY-BODIPY}[STY-BODIPY]R_i}{nk_{in}\ [RTA]};\quad n = \frac{t_{inh}R_i}{[RTA]}$$

Figure 2.10 RTA activity of Nec-1, Nec-1i, and Nec-2, measured by coautoxidation of STY-BODIPY (**A**) at 37 °C with cumene (**B**) and liposomes (**C**). Experiments in cumene were performed in triplicate and liposome experiments were performed at varying concentration alongside PMC as a control RTA.

We were surprised to discover that Nec-1, Nec-1i, and Nec-2 lacked any observable RTA activity in organic solution (**Figure 2.10B**) or in liposomes (**Figure 2.10C**). In all cases, no discernable retardation of the autoxidation reaction can be seen, and dye consumption takes place at a similar rate to the uninhibited autoxidation. An RTA control (4.0 μM PMC) was included as part of the liposome experiments, clearly exemplifying the otherwise lacking inhibitory period as the RTA is consumed. Considering the low potency necrostatin(s) display in cells, we predicted that RTA activity may be present, but not immediately obvious at the lower concentrations used during experimentation. However, increasing Nec-1 concentration to 20.0 μM in organic solution still provided a rate indistinguishable to that observed in the co-autoxidations to which 2.0 and 4.0 μM were added (**Figure 2.21**).

With insufficient RTA activity to justify the cytoprotection observed from necrostatin(s), we wondered about its ability to inhibit lipid peroxidation indirectly by modulating other redox processes in the cell via one-electron chemistry. Using cyclic voltammetry (CV), Nec-1, Nec-1i, and Nec-2 were found to have irreversible oxidation potentials in acetonitrile (MeCN) at 1.45, 1.40, and 1.60 V (values reported vs. NHE), respectively (**Figure 2.11A**,**D**, **2.22-2.36**). The electrochemical experiments were repeated in aqueous solution (pH = 7.4) to see if a downward shift in oxidation potential was observed under physiological conditions (**Figure 2.11B**). In aqueous solution, a lower-voltage peak was observed for all three compounds (1.19-1.24 V), alongside a second peak comparable to that in organic solution (1.52-1.54 V), and an additional peak for Nec-2 (1.36 V). To test the reversibility of this new aqueous peak, CV was run with a reduced switching potential of 1.10 V. Unfortunately, this new oxidation peak was also found to be irreversible in nature (**Figure 2.11C**, **2.28-2.30**). Thiohydantoin and hydantoin structures have a reported pKa of 8.5[40] and 9.1,[41] respectively, and are charged under basic conditions (**Figure 2.11 E**,**F**). Thus, pH was increased to 8.5 and 10.0 to study the effect of deprotonation (and reciprocal charge) on oxidation potential. Increasing basicity did not affect oxidation peak potential, however, the second Nec-2 peak was suppressed at pH = 8.5, and the earliest oxidation peak was suppressed in all three necrostatin(s) at pH = 10.0.

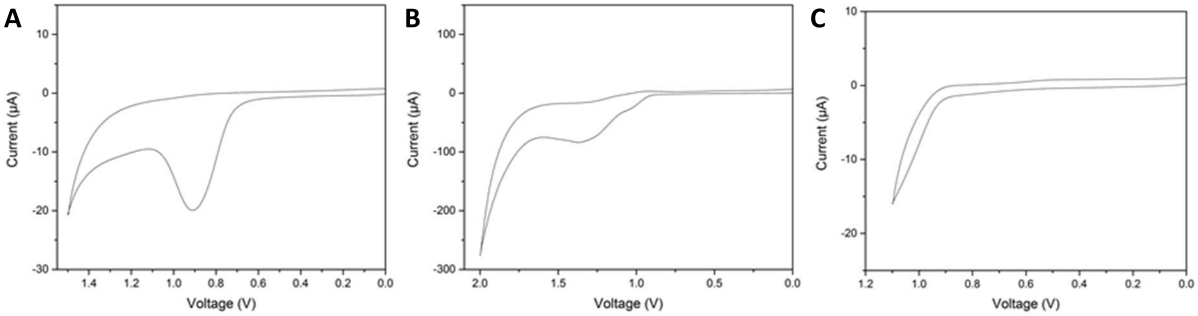

D

	Nec-1		Nec-1i		Nec-2		
	$E_{ox,1}^0$ (V)	$E_{ox,2}^0$ (V)	$E_{ox,1}^0$ (V)	$E_{ox,2}^0$ (V)	$E_{ox,1}^0$ (V)	$E_{ox,2}^0$ (V)	$E_{ox,3}^0$ (V)
MeCN	n.p.	1.45	n.p.	1.40	n.p.	n.p.	1.60
pH = 7.4	1.24	1.53	1.21	1.52	1.19	1.36	1.54
pH = 8.5	1.23	1.51	1.23	1.47	1.22	supp.	1.53
pH = 10.0	supp.	1.50	supp.	1.45	supp.	supp.	1.48

n.p. = no peak observed; supp. = peak suppressed into curve

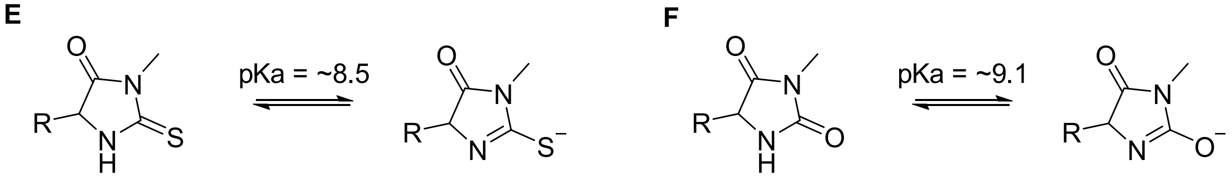

Figure 2.11 CVs of Nec-1 (vs. Ag/Ag+) in organic solution (**A**) and in 10mM potassium phosphate buffer (pH = 7.4) with an upper bounds of 2.0 (**B**) and 1.1 V (**C**), standard oxidation potentials (vs. NHE) of Nec-1, Nec-1i, and Nec-2 in organic solution (MeCN) and aqueous solution (buffered at pH = 7.4, 8.5, and 10.0) (**D**), and structures of thiohydantoin (**E**) and hydantoin (**F**) functionalities in their acidic and conjugate base form.

Considering that necrostatin(s) were neither RTAs nor significantly redox-active, we wondered if they were somehow able to indirectly suppress lipid peroxidation, thereby suppressing ferroptosis. To do so, C_{11}-BODIPY, a lipophilic BODIPY analog, was used to inform on the extent of lipid peroxidation in cells co-treated with RSL3 and the necrostatins (**Figure 2.12A**).[42] The fatty acid tail of C_{11}-BODIPY allows the probe to traverse cellular membranes and track lipid-specific peroxidation, making it an ideal method to study ferroptosis.[43] HT-1080 cells were treated with C_{11}-BODIPY, RSL3 to induce ferroptosis, and varying concentrations of Nec-1 alongside Lip-1 and PD146176, two well-characterized RTAs. As cells became ferroptotic, oxidation was assessed via flow cytometry (**Figure 2.12B-E**). Lip-1 and PD146176 shared very similar trends, with the lowest concentrations of RTA-treatment, at which cell viability was very low, resulting in oxidation measurements very similar to RSL3 control groups. Correspondingly, increasing RTA concentration led to reduced levels of lipid peroxidation associated with suppression of ferroptosis at cell-rescuing concentrations of RTA. Interestingly, Nec-1 did not follow this trend. At concentrations of Nec-1 under which complete cell rescue from ferroptosis was observed, membrane oxidation remained at levels similar to the RSL3 control. Regardless of the level of Nec-1 treatment, cells underwent lipid/BODIPY peroxidation at the same rate that would be expected in ferroptotic cells. As a side note, the measured cell count at 0.10 μM Lip-1 was low during all three replicates due to low cell viability, however, the recorded fluorescent intensity was comparable to the RSL3 control, consistent with the observed trends.

Spurred by this result, we sought to investigate if incubating cells with necrostatin(s) for prolonged periods prior to RSL3 treatment provided improved protection. Similar to α-TOH and C_{15}-THN, Nec-1 was reported by lab member Katie Shirley as having significantly increased potency in glutamate- and erastin-induced ferroptosis assays (i.e. 24 hour assays). For HT-22 and HT-1080 cells, IC_{50} values for glutamate and erastin-induced cell death were estimated at 5.0 and 0.085 μM, respectively; at least two orders of magnitude more potent than in RSL3-induced ferroptosis (**Figure 2.19**). Surmising that the cytoprotective effects of Nec-1 may be more pronounced following prolonged incubation, we attempted a similar experiment to that in **Figure 2.8**.

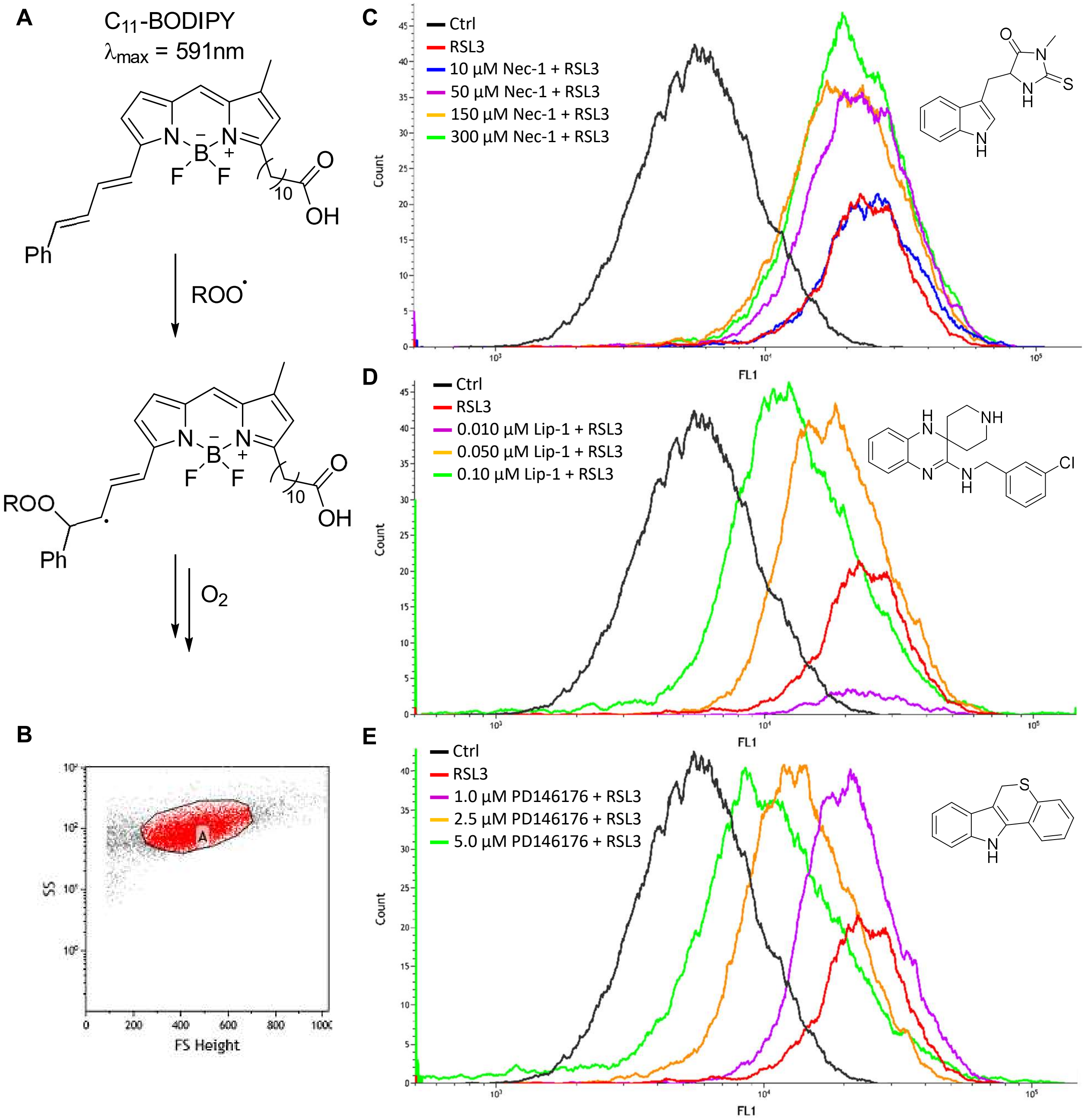

Figure 2.12 C_{11}-BODIPY coautoxidation (**A**) in HT-1080 cells treated with RSL3 (1.25 µM) and various concentrations of ferroptosis inhibitors. Cell fluorescence was assessed via flow cytometry (**B**) in the presence of Nec-1 (**C**), Lip-1 (**D**), and PD146176 (**E**) after 4 hour incubation at 37 °C.

To test the effects of prolonged incubation, HT-1080 cells were treated with Nec-1, Nec-1i, and Nec-2 and incubated for additional 4 and 20 hour periods prior to RSL3 treatment (**Figure 2.13A**). In the case of all three necrostatin analogs, no significant change in viability was observed during the assays (**Figure 2.13B-C**). Although trends in all three cases indicate a slight cytoprotective shift with increasing incubation, this minor trend pales in comparison to the dramatic difference in IC_{50} for erastin- and glutamate-treated cells (**Table 2.2**). Thus, the observed differences in potency of Nec-1 does not greatly vary with incubation time, but instead by the method which ferroptosis is induced.

Table 2.2 IC_{50} values for HT-1080 cell rescue in the presence of Nec-1 from RSL3- and erastin-induced cell death while varying incubation time.

Ferroptotic Agent	RSL3			Erastin
Incubation time (h)	0	4	24	24
IC_{50} Nec-1 (μM)	44	21	10	0.085

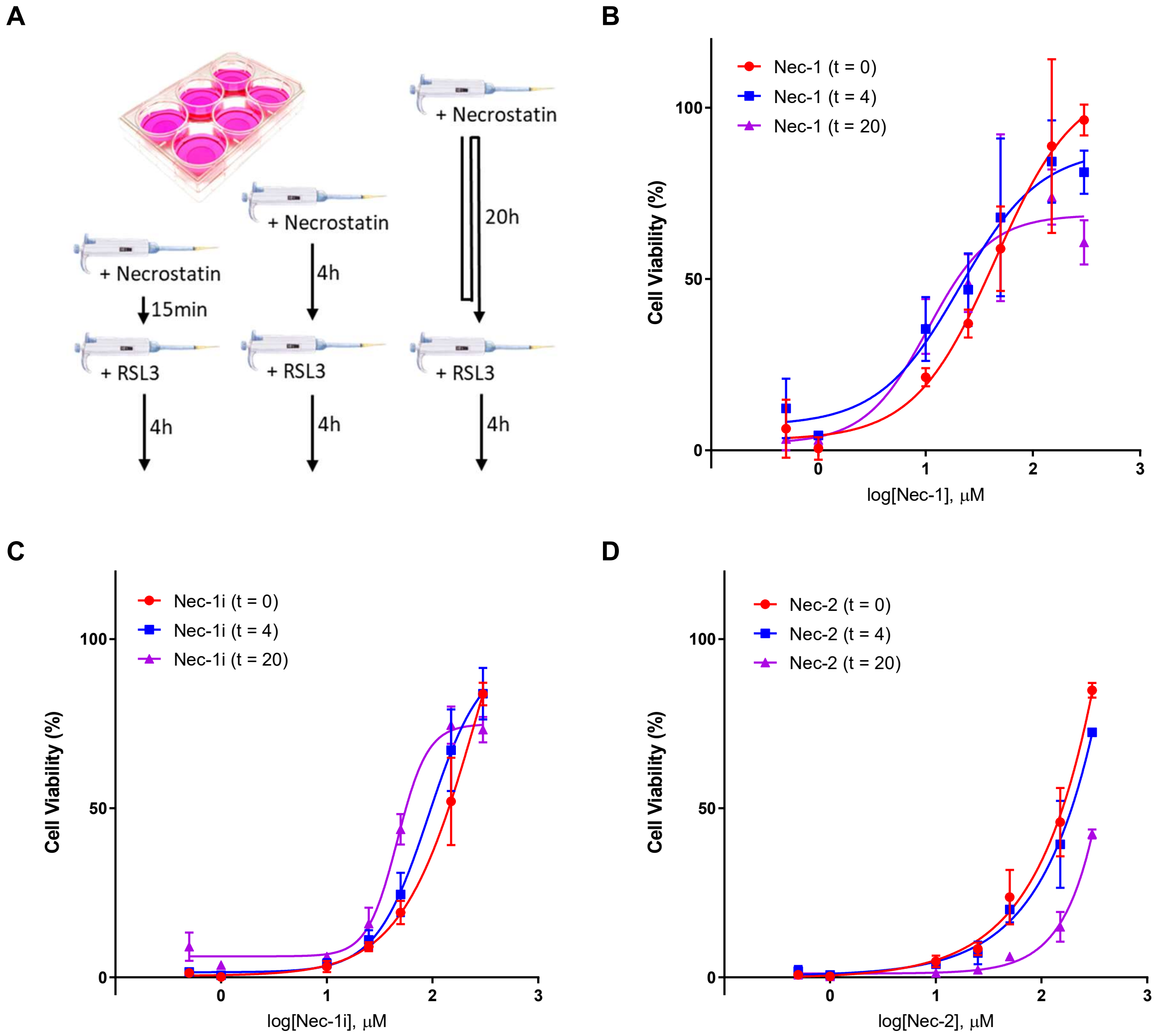

Figure 2.13 Ability of necrostatin(s) to rescue HT-1080 cells from RSL3-induced cell death after prolonged incubation period with inhibitor. As shown in (**A**), cells were incubated for an additional 4 and 20 hours before 4 hour RSL3 (2.0 μM) incubation in the presence of Nec-1 (**B**), Nec-1i (**C**), and Nec-2 (**D**).

It was reported to us by a collaborator's lab, that Nec-1-treated cells rapidly underwent ferroptosis upon replacement of the media following incubation. This result indicated that Nec-1 must be exerting its protective effects in a reversible manner, and a 'washout' of the media would remove any lasting cytoprotection. Given that our collaborators were studying this effect by 4-OH-tamoxifen (TAM)-induced ferroptosis in mouse embryonic fibroblast (Pfa1) cells, which prevents GPX4 expression by gene deletion, we chose to implement a similar method for RSL3-induced cell death. To do so, we first measured RSL3-potency in Pfa1 cells, finding an LD_{50} of 0.58 μM (**Figure 2.14A**). Subsequently, measuring the dose-response of Nec-1 to RSL3-induced ferroptosis yielded a result quite similar to that found in HT-22s, with cells undergoing rescue at $3.0 * 10^2$ μM Nec-1, with a dose-response insufficient to generate a true IC_{50} value (**Figure 2.14B**).

The devised washout assay involved a 4 hour incubation with $3.0 * 10^2$ μM Nec-1 and 2.0 μM RSL3, as per our standard AquaBluer assay. However, instead of AquaBluer treatment, Nec-1 media was removed and replaced with fresh media (**Figure 2.14C**). Cell viability was then visually monitored for a difference between the washout cells and the control group. After 4.5 hours, the washout Pfa1 cells were observed to have ferroptosed, and viability was assessed. Although sufficient Nec-1 was present during treatment to prevent ferroptosis, this was not a lasting effect, as there was a dramatic loss in Pfa1 viability between the control group and washout cells after the additional 4.5 hour incubation (**Figure 2.14D**). Expecting to find similar results in HT-22 and HT-1080 cell lines, we repeated the experimental measures only to find this was not universally the case. Following washout (at 4.5 hours), HT-22 cells showed pronounced loss of viability, but in contrast, after 8 hours HT-1080 cells still did not show signs of sensitivity to the Nec-1 washout. These results indicate a cell-line-dependent response to Nec-1 rescue activity.

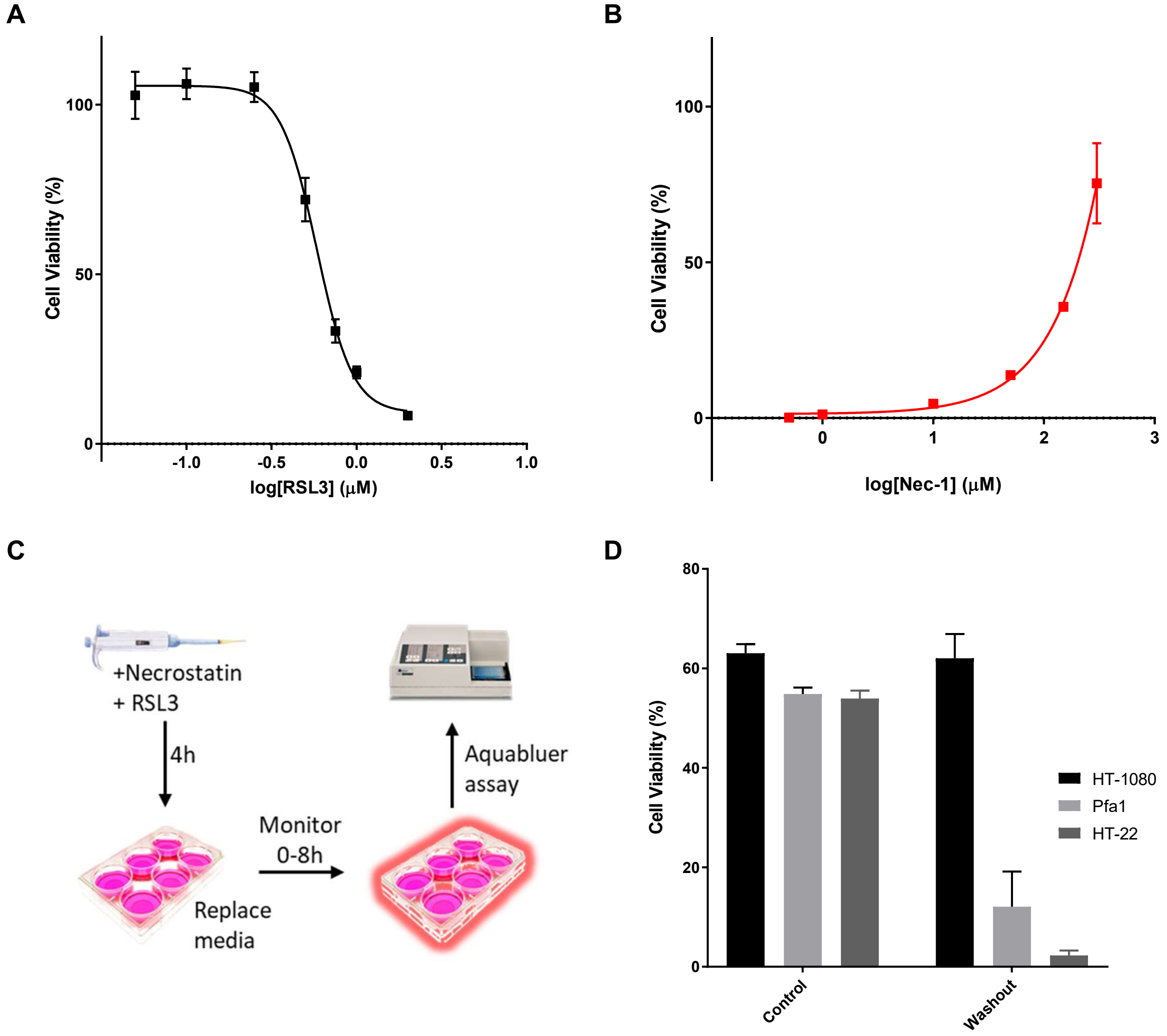

Figure 2.14 Washout experiment between HT-1080 and Pfa1 cells in the presence of Nec-1. Sensitization of Pfa1 cells to RSL3 treatment (**A**), dose-response curve to cells treated with 2.0 μM RSL3 and varying concentrations of Nec-1 (**B**), and viability of cells after rescue from RSL-3-induced ferroptosis by Nec-1 followed by subsequent washout/replacement of media and extended incubation (**C & D**) (additional 8 hours for HT-1080, and 4.5 hours for Pfa1).

2.3 Discussion

Ferroptosis has been characterized as the iron-dependent accumulation of lipid hydroperoxides in cellular phospholipid bilayers.[1] The often-cited source of hydroperoxide accumulation is LOX-catalyzed oxygenation of lipids, which has been illustrated through LOX gene regulation (e.g. gene knockouts, RNA interference)[7] and pharmacological inhibition (i.e. LOX inhibitors),[6] although only the latter has been translated *in vivo* (GPX4$^{-/-}$ knockout mice).[8] Unfortunately, LOX inhibitors identified as anti-ferroptotic often possess off-target RTA (or other) activities which put their preventative mechanism-of-action in question.[11] In addition, no specific isoform of LOX has been implicated in initiation of ferroptosis.[7,8,13] In 2018, our lab published results suggesting that although LOX may play a minor role in contributing to the cellular pool of ROS it is autoxidation, not LOX, which serves as the primary driver of ferroptosis.[14] In fact, off-target RTA activity was necessary for effective inhibition of cell death and anti-ferroptotic activity was independent of LOX overexpression. These findings were accomplished by screening redox-active LOX and redox-inactive 5-LOX inhibitors in HEK-293 cells transfected for 5-LOX, p12-LOX, and 15-LOX-1 overexpression. Given the limited scope of these experiments (transfected HEK-293 cells and redox-inactive 5-LOX inhibitors), we expanded upon efforts to resolve the role of LOX using HT-22 and HT-1080 cell lines, the cell models in which ferroptosis and oxytosis were originally characterized, in combination with an expanded redox-inactive inhibitor screen to include 15-LOX-1, 15-LOX-2 and p12-LOX.

Assays of RTAs, redox-active LOX inhibitors, and redox-inactive LOX inhibitors in tandem provides us with a basis to resolve the role of LOX in ferroptosis. By distinguishing between RTAs and LOX inhibitors and examining the rescue activity of the compound screen, the importance of antioxidative activity as criteria for cytoprotection becomes apparent. LOX inhibition or not, compounds are only cytoprotective provided they possess RTA activity. If LOX enzymes were necessary drivers of ferroptosis, at the very least partial rescue would be expected from LOX inhibitors. However, 'true' LOX inhibitors lack RTA activity (i.e. they lack the ability to inhibit autoxidation in a lipophilic environment) and were unable to show rescue activity in either HT-22 or HT-1080 cell lines, the quintessential oxytosis and ferroptosis lineages. Previously demonstrated through 5-LOX inhibitors CAY10649 and CJ-13610,[14] we not only find equivalent cytoprotective trends in HT-22 and HT-1080 cell models, but exemplify the ineffectiveness of inhibiting LOX in isoforms 15-LOX-1 and 15-LOX-2. The inability to rescue cells using 15-LOX-2 inhibitors is particularly significant, as this isoform is dominantly expressed in both HT-22[21] and HT-1080[4] cells. If ferroptosis were dependent on LOX activity, 15-LOX-2 inhibition would be expected to have a pronounced effect on ferroptotic resistance, which is not observed in either cell lineage. Our results strengthen our lab's previous work,[14] providing complementary findings in archetypal cell lines and expanding our LOX isoform-specific scope to 15-LOX-1 and 15-LOX-2. These results support our theory of an autoxidation-driven ferroptotic model, as LOX inhibition alone was insufficient to rescue cells from ferroptosis. Autoxidation of cellular membranes can be initiated by many sources, and although LOX may contribute to the cellular pool of ROS, they are merely one facet in the initiative process of autoxidation.

We attempted to include a redox-inactive p12-LOX inhibitor, β-thujaplicin, to demonstrate ineffectiveness of inhibiting the p12 isoform as well; however, we were surprised to find it completely rescued cells from ferroptosis. Although the lack of RTA activity was at first puzzling, β-thujaplicin is not simply a p12-LOX inhibitor but is capable of iron chelation as well.[37] Although this research is focused on the influence of RTAs on lipid peroxidation, there are of course other factors contributing to ferroptotic inhibition, one of which is iron chelation. Ferroptosis is iron-dependent and iron chelators (e.g. ciclopirox olamine, deferoxamine) deplete oxidation-promoting enzymes and prevent peroxide-forming chemical reactions from promoting autoxidative initiation.[1,44] Thus, the anti-ferroptotic activity of β-thujaplicin is justified by its chelating function, and further screening would be required to verify the ineffectiveness p12-LOX inhibitor without off-target effects. Through high-throughput screening, a series of highly isoform-specific p12-LOX inhibitors (from a 8-hydroxyquinoline-based scaffold) were identified, reported as lacking RTA and active site iron-chelating effects.[45] To expand on our findings, several of these p12-LOX inhibitors should be prepared, validated as RTA/iron chelating activity-free, and screened in our cell lines.

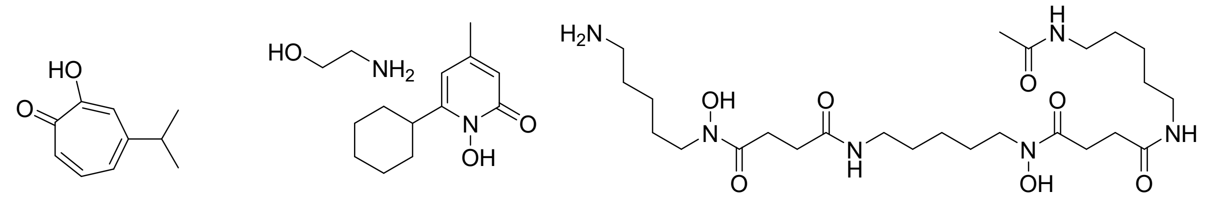

β-Thujaplicin (p12-LOX) Ciclopirox olamine Deferoxamine

Figure 2.15 Chemical structures of anti-ferroptotic iron-chelating agents. LOX isoform targets are noted.

The only redox-active compound lacking numerical (IC_{50}) data in RSL3-induced ferroptosis is p12-LOX inhibitor, ML355. Although it was shown effective at rescuing HT-1080 cells, its limited solubility prevented us from displaying rescue in HT-22s. However, the low solubility of ML355, combined with the highest recorded IC_{50} in HT-1080 cells (34 μM) justify this absence. Examining the IC_{50} concentration trends in **Table 2.1**, rescue activity is less pronounced in HT-22 cells for ten of eleven compounds (and comparable for PD146176). Were ML355 to follow in this trend, an elevated IC_{50} would be predictably higher than the already solubility-limited HT-1080 concentration. Most likely, this compound's lack of solubility overshadows its poor rescue activity, limiting our ability to observe rescue in the more tolerant HT-22 cell line.

The comparable rescue activity of redox-active LOX inhibitors lends weight to their shared RTA activity as a means to their function, and less so to their diverse range of LOX activity. Were LOX inhibition to dictate these compounds' inhibitory effects, a much more variable range of potency could be expected between compounds, which act on enzymes of varying levels of expression and location in each cell line. For example, NDGA, zileuton, and PD146176, LOX inhibitors each with varying isoform specificity, would likely not have such comparable potencies in both cell lines. RTAs are often defined by their ability to act as effective HAT donors, and the absence of such sites on redox-inactive LOX inhibitors is not a coincidence. Ferroptotic and LOX inhibitors are often found via high-throughput screening of small molecules,[1,7,32,46] and are often studied prior to a thorough analysis of off-target (e.g. redox) activity. In fact, prior to our lab's initial discoveries on the role of redox-chemistry in ferroptotic inhibition,[12,14] although redox activity of LOX inhibitors is sometimes noted,[11] their reactivity in a biological context was not investigated and has been overlooked in place of LOX activity.[18,32]

In our 2018 work, LOX overexpression was also found to sensitize cells to induction of ferroptosis with RSL3 and erastin, and by culturing these cells with redox-inactive 5-LOX inhibitor CJ-13610 specifically desensitized 5-LOX overexpressing cells.[14] This finding supports our theory of an autoxidation-driven ferroptotic model, in that LOX partly contribute to the initial pool of lipid hydroperoxides, which can then be inhibited downstream by RTAs. In support of our work, similar experiments should be carried out in HT-22 and HT-1080 cells, wherein cells are cultured in the presence of redox-inactive 15-LOX-1 and 15-LOX-2 inhibitors. Were the cells to become less susceptible to RSL3-initiated (or otherwise) ferroptosis this would complement our findings with transfected cells in archetypal cell lines.

Protocol modification (i.e. culturing without L-Gln and increasing RTA incubation time) did not yield an increase in potency comparable to that observed in glutamate- and erastin-induced cell death experiments, but did provide several valuable insights into ferroptotic processes. There are mixed reports regarding the effect of L-Gln on ferroptosis.[47] Our own lab has found L-Gln to confer resistance to glutamate-induced ferroptosis in HT-22 cells, while in contrast, glutamine deprivation has also been cited as a method of inhibiting ferroptosis in mouse embryonic fibroblasts (MEFs).[44] Although not fully understood, the glutaminolysis pathway is central in ferroptosis, responsible for glutamine metabolism and glutamate production.[44,48] While not a primary focus of this work, the minimal effect on ferroptotic rescue found between L-Gln and RSL3-induced cell death serves to emphasize the distinct methods by which we can induce ferroptosis. While many ferroptosis inducers target the production of GPX4 substrate glutathione, closely linked to L-Gln and glutaminolysis, RSL3 directly inhibits GPX4, an effect which negates any peripheral influence on substrate presence. As a result, we do not observe sizable changes in sensitivity to RSL3-induced ferroptosis when varying L-Gln availability.

Increasing incubation time of RTAs α-TOH and PMC to that of erastin- and glutamate-induced cell death (24 hours) resulted in comparable potency for α-TOH in erastin-induced ferroptosis of HT-1080 cells, and although longer incubation times did mildly increase C_{15}-THN potency the effect was not as pronounced. As before, ferroptotic initiator plays a role in determining rescue activity. RSL3-induced cell death can require higher concentrations of RTA for rescue compared to induction by erastin or glutamate, which could be linked to the specificity of RSL3 for GPX4, which covalently inhibits a central enzyme involved in preventing ferroptosis. [81] While erastin and glutamate stress several cellular pathways which includes GSH depletion, RSL3 eliminates GPX4 function irreversibly, a more precise method leading to accumulation of lipid hydroperoxides. Although this may help justify the higher concentrations of some RTA necessary to rescue from RSL-induced ferroptosis, it is not universally the case. An emerging issue to consider regarding distinct approaches for induction of cell death (i.e. erastin, RSL3, etc.), is whether ferroptosis initiated by these different agents can even be considered alike. In a recently accepted manuscript, the Birsoy lab has shown that treatment with erastin and RSL3 results in the upregulation of completely different sets of genes, indicating the process of ferroptosis execution varies by initator.[49] These regulatory differences help to explain the variations we observe when varying ferroptotic-initiator, particularly when contrasting redox-active LOX inhibitor rescue RSL3- to erastin-induced cell death, the later of which are incompletely rescued in many cases (See **Table 2.1**). These regulatory differences in gene expression affect the rate and timing at which lipid peroxidation and subsequent ferroptosis occurs, observable through the differences in incubation required to induce ferroptosis. As RTAs are fixed in their rates of inhibition and degradation, their potency could vary as the timing of initiator-dependant ferroptotic lipid peroxidation varies. For example, if an RTA undergoes degradation before the 24-hour erastin-induction of ferroptosis runs its course, it would be unable to prevent the latent lipid peroxidation and ferroptosis. This is in fact observed in many of the redox-active LOX inhibition assays, which are unable to fully rescue cells from ferroptosis. Current research in our and other labs are aimed at more accurately differentiating these different initiative mechanisms.

Screening Nec-1 and its analogs Nec-1i and Nec-2 provided an unexpected deviation from the pattern of results observed in the LOX study. All three necrostatin compounds provided cytoprotection from RSL3-dependent ferroptosis at considerably high concentrations, and although Nec-1i and Nec-2 were not potent enough to provide a complete dose-response, their curves certainly indicate potencies close behind that of Nec-1. Nec-1i, the inactive control for Nec-1, rescuing cells from ferroptosis at comparable concentrations provides strong support that the cytoprotective activity of necrostatin derivatives is unrelated to the RIPK1 inhibition Nec-1 is known for in the literature.[29] Were RIPK1 inhibition key to ferroptotic inhibition, little to no protective effect would be expected from Nec-1i.

The structural similarities amongst necrostatins indicated to us that anti-ferroptotic activity was likely resulting from an off-target effect related to a shared structural feature. The necrostatin scaffold consists of an indole core bound at C-3 to a (thio)hydantoin functionality, the former of which is an arylamine, known for their good RTA abilities (e.g. Lip-1, Fer-1, etc.).[12,50] The N-H bond of unsubstituted indole is somewhat weak (88 kcal/mol)[51] making it comparable in strength to RTA scaffold phenol (87 kcal/mol)[52] and only ~5-6 kcal/mol greater in strength than Fer-1 and Lip-1.[12] Given that indole groups are incorporated into biologically active RTAs (e.g. arylated indole PD146176), we sought to confirm if necrostatin(s) possessed RTA activity. Necrostatin(s) were found devoid of RTA activity in organic solution and liposomes, indicating the observed cytoprotective effects must be otherwise associated. Oxidation potentials of 5-(3’-indolyl)-2-thiohydantoin derivatives, compound(s) sharing the indole and (thio)hydantoin functionalities of necrostatin (**Figure 2.16**), have been measured and appear to share the characteristic two-peak scan of necrostatin(s) in aqueous buffer.[53] All oxidative processes were associated with the indole-bound nitrogen atom, with no oxidation step observed for thiohydantoin, findings which may be translatable to necrostatin(s). Our irreversible oxidation potentials observed were also noticeably higher than that reported for indolyl-derivatives (1.19-1.24 V vs. NHE contrasted to their 0.66-1.11 V vs. NHE in aqueous media), possibly attributed to the increased indole radical stabilization from the C-3 allyl functionality. Necrostatin oxidation potentials are also much higher than known redox potentials biologically active compounds such as uric acid and ascorbate (0.59 V and 0.28 V vs. NHE, respectively)[54] indicating necrostatin(s) are not an ideal substrate for electron transfer.

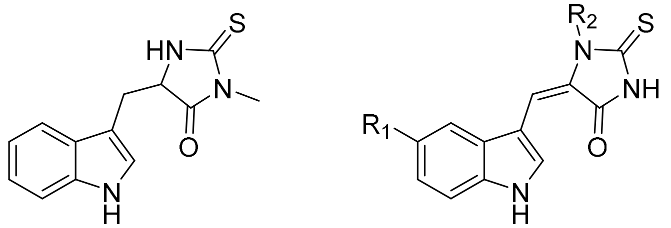

Figure 2.16 Chemical structures of Nec-1 (left) and the 5-(3'-indolyl)-2-thiohydantoin scaffold (right).[53]

Contrasting our initial Nec-1 peak measured in MeCN (0.91 vs. Ag/Ag$^+$) to the literature value of unsubstituted indole (0.9 V vs. Ag/Ag$^+$)[55] strongly indicates it is the indole functionality which is being oxidized. To determine whether the lower-voltage peaks observed in the aqueous CVs are from additional indole oxidations or the (thio)hydantoin group, further CV studies should be undertaken with separate indole and (thio)hydantoin substrates for comparison. The two moieties are separated on necrostatin(s) by a methylene bridge, and these nonconjugated functionalities should oxidize independently, which we can contrast to the independent indole/hydantoin oxidation potentials.

The observations of cellular membrane oxidation via flow cytometry aids in characterizing the impact of necrostatin(s) in cell death. Lip-1 and PD146176 are anti-ferroptotic RTA agents, and their abilities to prevent the accumulation of lipid hydroperoxides and resulting ferroptosis are well understood.[12,14] Inducing ferroptosis in their presence provided the predicted result, with cellular lipid oxidation decreasing as RTA concentration increases, inhibiting ferroptosis by limiting the accumulation of lipid hydroperoxides. However during Nec-1 treatment, cellular oxidation levels were similar to RSL3-induced ferroptotic control groups, even though the cells were viable – based on both metabolic assessment (AquaBluer assay) and based on visualization by phase contrast microscopy. Firstly, this verifies that Nec-1 subverts ferroptosis by a mechanism other than RTA activity. The prior coautoxidation experiments in organic solution and liposomes indicated a lack of RTA activity in necrostatin(s), but the FC results cement that RTA activity is absent in the cellular environment. Secondly, given that Nec-1-rescued cells retain oxidation levels comparable to that of the ferroptosed RSL3 control, Nec-1 appears to supersede an otherwise lethal accumulation of lipid hydroperoxides. Nec-1 is preventing ferroptosis, but not the autoxidative propagation with which ferroptosis is associated, a feature unlike rescue by other anti-ferroptotic agents (i.e. RTAs, iron chelators, etc.) to date.

Given its improved potency in erastin and glutamate-induced cell death, we theorized cytoprotection may be attributed to necrostatin(s) serving as a metabolic substrate or transcription factor, requiring prolonged incubation periods to express its full effects. However, increasing the incubation time of cells with Nec-1, Nec-2, and Nec-1i for up to 24 hours led to no increase in potency against RSL3-induced ferroptosis. Given the recent revelation that erastin and RSL3 initiate ferroptosis though distinct gene regulation,[49] the improved potency of Nec-1 observed rescuing cells from erastin and glutamate could be related to the method of ferroptotic induction similar to that observed in our RTA studies. Speculatively, the difference in Nec-1 potency between ferroptotic initiators could be explained by initiator-dependent up- or downregulation of genes. As a start, in follow-up to this work, Nec-1i and Nec-2 should also be screened against erastin/glutamate to observe if potency is consistent with Nec-1.

The cytoprotective effect imposed by Nec-1 appears to be rapidly lost upon media replacement post-rescue. Performing a 'washout', replacing RSL3/Nec-1-containing media with fresh media, two out of three cell lines lose viability in under five hours, apart from HT-1080s. This indicates that Nec-1 exerts a reversible cytoprotective effect, the extent of which varies based on cell line. RSL-3 covalently binds GPX4, and sufficient enzyme modification occurs within the four hour window to execute ferroptosis.[26] Thus, when replacing media, RSL3 has already exerted its intended effect, meaning the variation in viability observed can be tied to Nec-1. The pronounced drop in cell viability observed in Pfa1 and HT-22 washout cells indicates that Nec-1 must neither be consumed (like an RTA) nor covalently modified (as with RSL3). Furthermore, the reversal of its effect upon media replacement implies Nec-1 is exerting its effect on the outside of the cell membrane. Given that necrostatin(s) does not inhibit autoxidation, and lipid peroxidation accumulates as a consequence, the loss of the inhibitor appears to allow ferroptosis to run its otherwise inevitable course. Of note, during visual inspection, washout HT-1080 cells also showed early signs of stress and cell death, but this was not sufficiently pronounced at the end of the eight hour incubation period. This suggests that HT-1080s are not insensitive to Nec-1 washout, but simply more slow to react. In order to gain a more complete picture as to the effects of a media washout, a more comprehensive series of experiments should be implemented in future work. For now, we can conclude that Nec-1 exerts a unique (potentially extracellular) cytoprotective effect of which cell lineage plays a key role in its mode of action.

2.4 Conclusions

After screening a library of RTAs, redox-active LOX inhibitors, and redox-inactive LOX inhibitors, we conclude that autoxidation, not LOX activity, presents as the primary driver of ferroptosis. The most cytoprotective compounds tested possess robust rates of inhibition in lipophilic environments, representative of their competency as RTAs within cellular membranes. The only LOX inhibitors with notable anti-ferroptotic activity possess off-target effects, either serving as RTAs or in some cases, iron chelators. This has now been exemplified in two model cell lineages of oxidative stress, both of which show identical patterns of response to ferroptosis (and oxytosis) inhibition, emphasizing the broad application of these findings. In particular, 15-LOX-1 and 15-LOX-2 inhibitors were proven ineffective at protecting from ferroptosis, complementing the previously debunked role of 5-LOX inhibition. Although an effort was made to discredit the role of p12-LOX as well, the screened inhibitor had off-target iron chelating effects and future efforts to rule out this isoform are required.

Our efforts in protocol modification during RSL3-induced ferroptosis have provided some interesting and unexpected results. Although far from the major focus of this work, RSL3-induced cell death has shown a relative lack of sensitivity to L-Gln and incubation time when contrasted to erastin-induced cell death. These findings add to mounting evidence that erastin and RSL3 initiate distinct cellular processes both resulting in ferroptosis.

Lastly, while investigating the anti-ferroptotic effects of necrostatin(s) we discovered a class of cytoprotective compound not yet fully characterized. Necrostatin compounds lack RTA activity, possess high oxidation potential, and do not prevent autoxidation in cellular environments. Nevertheless, necrostatin(s) provide rescue from ferroptosis at high doses and are cytoprotective even after lipid peroxidation reaches ferroptotic levels. This form of rescue, is not time dependent, possesses comparable dose-response among analogs which is lost upon removal of inhibitor from the medium, and could be achieved for each mode of ferroptosis induction with varying potency. Although the anti-ferroptotic effect of RTAs is now clear, necrostatin(s) exemplify that alternate mechanisms of ferroptotic inhibition exist, requiring continued investigation.

2.5 Experimental

Cell culture materials including Dulbecco's phosphate-buffered saline (DPBS), Dulbecco's modified eagle medium (DMEM) with and without phenol red, non-essential amino acid (NEAA) cell culture supplement, fetal bovine serum (FBS), penicillin-streptomycin (P/S), L-glutamine (L-Gln), and AquaBluer^{TM} (Multitarget Pharmaceuticals, LLC) were purchased from commercial sources and used as received. LOX Inhibitors MLS00054509, MLS000327186, MLS327069, ML094, and ML351 were synthesized by Pratt Group graduate student Katie Shirley. RSL3, Lip-1, Fer-1, C_{15}-THN, C_{16}-THN, and STY-BODIPY were synthesized by other members of the Pratt Group, according to literature procedure. AIBN, MeOAMVN, Egg PC, and all other chemicals and solvents were purchased from commercial sources and used as received.

Cell Culture: HT-22 and HT-1080 cells were cultured in a VWR^{TM} Shel Lab 2300 water jacketed incubator at 37 ^{o}C under 5% CO_2 atmosphere. Cells were grown in DMEM media with phenol red containing 10% FBS, 1% P/S, and 10 mM L-Gln, unless otherwise noted. HT-1080 cell media also contained 1% 100x NEAA. During passage, media was removed, plate was washed with 7 mL DPBS, and cells were dissociated using 0.05% trypsin and 0.2% EDTA. For experimental procedures using DMEM without phenol red, media was prepared without FBS. Cell were passaged when confluent, approximately every two days. All cell work was carried out under a DFMZ$^{©}$ BK-3-6 biological safety cabinet.

AquaBluer^{TM} (Multitarget Pharmaceuticals, LLC) Assay: Unless otherwise noted, cells were plated at 3000 cells/well on 96-well plates in 100 μL DMEM containing phenol red the day prior to assay. Compound of interest was dissolved in DPBS and added to wells in a volume of 5 μL. Following a fifteen minute incubation period, RSL3 dissolved in DPBS was added in a volume of 10 μL at a concentration of 0.80 μM for HT-22 cells and 2.0 μM for HT-1080 cells. Cells were incubated for four hours at which point media was removed and replaced with AquaBluer 1/100 v/v in DMEM (without phenol red). Cells were incubated for an additional four hours and measured by fluorescence on a BioTek® Synergy H1 microplate reader. DMSO concentration was maintained below 1% of total well volume. α-TOC was purified by column chromatography the day of use. All experiments were carried out in triplicate on the same day/cell batch. Dose-response values were calculated by nonlinear regression (log(inhibitor) vs. response – variable slope) using GraphPad Prism® 7.04. Cases in which response was insufficient to determine IC_{50} by regression modelling, dose-response was extrapolated to estimate a value, noted in-text (*).

Washout Assay: Cells were plated at 3000 cells/well on a 96-well plate in 100 μL DMEM containing phenol red the day prior to assay. Nec-1 was dissolved in DPBS and added to wells in a volume of 5 μL, followed by 10 μL of RSL3 dissolved in DPBS at a concentration of 2 μL for both HT-1080 and Pfa1 cells. Cells were incubated for four hours, at which point the media was removed and replaced with fresh media, control group was left as is. Cells were then monitored for ferroptosis at the first 15 and every 30 minutes for 8 hours. Upon cell death or completion of assay, whichever came first, media was replaced with AquaBluer 1/100 v/v in DMEM (without phenol red). Cells were incubated for an additional four hours and measured by absorbance on a BioTek® Synergy H1 microplate reader. DMSO concentration was maintained below 1% of total well volume. All experiments were carried out in triplicate.

Cumene Preparation: Commercial cumene was purified by first washing three times with 1M NaOH, followed by $H_2O_{(d)}$, and brine. The organic fraction was dried using $MgSO_4$, filtered, and heated to 55 ºC for fractional distillation under negative pressure. The collected distillate was than purified by silica plug using a column of ¼ silica (top) and ¾ alumina (bottom).

Cumene Coautoxidation: To a cuvette, 1.25 mL of freshly prepared cumene and 1.18 mL of PhCl were added. Cuvette was placed in a Cary 100 Bio UV-Vis spectrophotometer (Agilent Technologies, Inc.) and warmed to 37 °C for fifteen minutes. 12.5 μL of 2.0 mM STY-BODIPY (10 μM) in PhCl and 50 μL of 0.3 M AIBN (6 mM) dissolved in PhCl were then added, in that order. After 45 minutes, 10 μL of 500 μM stock (2 μM) of the compound of interest, dissolved in PhCl, was added. To controls, 10 μL of PhCl was added in lieu of the compound of interest. Experiments were performed in triplicate using HPLC grade solvents.

Egg-PC Liposome Preparation: To commercial phosphatidylcholine, sufficient chloroform was added to completely dissolve the lipid. Solution was placed under vacuum and spun by hand for approximately five minutes, until lipids were dried to sides of vial. Lipids were then left to dry for one hour after which they were dissolved in 10 mM PBS solution (pH = 7.4) to a lipid concentration of 25 mM. The mixture was then subjected to ten freeze-thaw cycles (five minutes in dry ice, five minutes in 35 °C water bath, five minutes sonication at 35 °C). After sonication, 1mL mixture was extruded 25 times through a 100 nm polycarbonate membrane (AVESTIN, Inc.) to produce uniform unilamellar micelles.

Autoxidation of Liposomes: To a cuvette, 125 μL of freshly prepared liposomes and 2.33 mL of 10 mM PBS solution (pH = 7.4) were added. Cuvette was placed in Cary 100 Bio UV-Vis spectrophotometer (Agilent Technologies, Inc.) and warmed to 37°C for fifteen minutes. 12.5 μL of 2 mM STY-BODIPY (10μM) in DMSO and 10 μL of 50 mM MeOAMVN (0.2 mM) dissolved in MeCN were then added, in that order. After 45 minutes, 10 μL or 20 μL of 500 μM stock (2 μM or 4 μM) of the compound of interest, dissolved in DMSO, was added. To controls, DMSO was added in lieu of the compound of interest. Experiments were performed in HPLC grade solvents.

Electrochemistry (Organic Solution): Standard potential was measured by cyclic voltammetry at 25 ºC with 0.1 M NBu_4PF_6 in anhydrous MeCN solution as the electrolyte. Experiments were performed on a BASi© C3 Cell Stand equipped with a 5 mM $AgNO_3$ reference electrode, glassy-carbon working electrode, and platinum auxiliary electrode. Ferrocene and tested compounds were run at a concentration of 3 mM in electrolyte containing 3% DMSO (from tested compound stock solutions). Oxidation potentials were calculated relative to ferrocene/ferrocenium couple in acetonitrile Fc/Fc^+ ($E^o = 0.64$ V vs NHE)[56].

Electrochemistry (Aqueous Solution): Standard potential was measured by cyclic voltammetry at 25 ºC with 3 M KCl in either 10 mM potassium phosphate buffer solution (pH = 7.4) or 10 mM potassium borate buffer solution (pH = 8.5 and 10.0). Experiments were performed on a BASi© C3 Cell Stand equipped with a AgCl aqueous electrode, glassy-carbon working electrode, and platinum auxiliary electrode. Potassium ferrate and tested compounds were run at a concentration of 1 to 3 mM in electrolyte containing 250 µL DMSO (8%) for solubility. Oxidation potentials were calculated relative to ferricyanide/ferrocyanide couple in aqueous solution ($E^o = 0.436$ V vs NHE)[57].

Flow Cytometry: Cells were plated at 100 000 cells/well on 12-well plates in 1mL DMEM containing phenol red the day prior to assay. C11 BODIPY (5 µM), RSL3 (0.4 µM for HT-22s and 1.25 µM for HT-1080s), and compound of interest (varying concentrations) were added, in that order, to wells. Experiment completion was assessed visually by light microscope (approximately 3-4 hours), at which time media was removed, cells were washed in DPBS, trypsinized, suspended in DMEM without phenol red, analyzed using flow cytometer. DMSO concentration was maintained below 1% of total well volume. Flow cytometry was performed on a Gallios Flow Cytometer (Beckman Cloutier, Inc.) with a 488 nm argon laser for excitation, with emission recorded at FL1 (530 nm) and FL2 (585 nm). Results were collected from a minimum of 5000 cells per experiment.

2.6 References

1. Dixon, S. J. et al. Ferroptosis: An Iron-Dependent Form of Nonapoptotic Cell Death. Cell 149, 1060–1072 (2012).
2. Shintoku, R. et al. Lipoxygenase-mediated generation of lipid peroxides enhances ferroptosis induced by erastin and RSL3. Cancer Sci. 108, 2187–2194 (2017).
3. Seiler, A. et al. Glutathione Peroxidase 4 Senses and Translates Oxidative Stress into 12/15-Lipoxygenase Dependent- and AIF-Mediated Cell Death. Cell Metab. 8, 237–248 (2008).
4. Yang, W. S. et al. Peroxidation of polyunsaturated fatty acids by lipoxygenases drives ferroptosis. Proc. Natl. Acad. Sci. U. S. A. 113, E4966–E4975 (2016).
5. Yang, W. S. & Stockwell, B. R. Ferroptosis: Death by Lipid Peroxidation. Trends Cell Biol. 26, 165–176 (2016).
6. Kagan, V. E. et al. Oxidized arachidonic and adrenic PEs navigate cells to ferroptosis. Nat. Chem. Biol. 13, 81–90 (2017).
7. Friedmann Angeli, J. P. et al. Inactivation of the ferroptosis regulator Gpx4 triggers acute renal failure in mice. Nat. Cell Biol. 16, 1180–1191 (2014).
8. Brütsch, S. H. et al. Expression of inactive glutathione peroxidase 4 leads to embryonic lethality, and inactivation of the Alox15 gene does not rescue such knock-in mice. Antioxidants Redox Signal. 22, 281–293 (2015).
9. Liu, Y. et al. The 5-lipoxygenase inhibitor zileuton confers neuroprotection against glutamate oxidative damage by inhibiting ferroptosis. Biol. Pharm. Bull. 38, 1234–1239 (2015).
10. Yigitkanli, K. et al. Inhibition of 12/15-lipoxygenase as therapeutic strategy to treat stroke. Ann. Neurol. 73, 129–135 (2013).
11. Czapski, G. A., Czubowicz, K. & Strosznajder, R. P. Evaluation of the antioxidative properties of lipoxygenase inhibitors. Pharmacol. Reports 64, 1179–1188 (2012).
12. Zilka, O. et al. On the Mechanism of Cytoprotection by Ferrostatin-1 and Liproxstatin-1 and the Role of Lipid Peroxidation in Ferroptotic Cell Death. ACS Cent. Sci. 3, 232–243 (2017).
13. Hadian, K. & Stockwell, B. R. SnapShot: Ferroptosis. Cell 181, 1188-1188.e1 (2020).
14. Shah, R., Shchepinov, M. S. & Pratt, D. A. Resolving the Role of Lipoxygenases in the Initiation and Execution of Ferroptosis. ACS Cent. Sci. 4, 387–396 (2018).
15. Burton, G. W. & Ingold, K. U. Vitamin E: Application of the Principles of Physical Organic Chemistry to the Exploration of Its Structure and Function. Acc. Chem. Res. 19, 194–201 (1986).
16. Skouta, R. et al. Ferrostatins inhibit oxidative lipid damage and cell death in diverse disease models. J. Am. Chem. Soc. 136, 4551–4556 (2014).

17. Li, B. et al. Besting vitamin E: Sidechain substitution is key to the reactivity of naphthyridinol antioxidants in lipid bilayers. J. Am. Chem. Soc. 135, 1394–1405 (2013).

18. Carter, G. W. et al. 5-lipoxygenase inhibitory activity of zileuton. J. Pharmacol. Exp. Ther. 256, 929–37 (1991).

19. Bocan, T. M. A. et al. A specific 15-lipoxygenase inhibitor limits the progression and monocyte-macrophage enrichment of hypercholesterolemia-induced atherosclerosis in the rabbit. Atherosclerosis 136, 203–216 (1998).

20. Li, Y., Maher, P. & Schubert, D. A role for 12-lipoxygenase in nerve cell death caused by glutathione depletion. Neuron 19, 453–463 (1997).

21. Wenzel, S. E. et al. PEBP1 Wardens Ferroptosis by Enabling Lipoxygenase Generation of Lipid Death Signals. Cell 171, 628-641.e26 (2017).

22. Davis, J. B. & Maher, P. Protein kinase C activation inhibits glutamate-induced cytotoxicity in a neuronal cell line. Brain Res. 652, 169–173 (1994).

23. Lewerenz, J., Ates, G., Methner, A., Conrad, M. & Maher, P. Oxytosis/Ferroptosis—(Re-) Emerging Roles for Oxidative Stress-Dependent Non-apoptotic Cell Death in Diseases of the Central Nervous System. Front. Neurosci. 12, (2018).

24. Maher, P. & Davis, J. B. The role of monoamine metabolism in oxidative glutamate toxicity. J. Neurosci. 16, 6394–6401 (1996).

25. Yang, W. S. & Stockwell, B. R. Synthetic Lethal Screening Identifies Compounds Activating Iron-Dependent, Nonapoptotic Cell Death in Oncogenic-RAS-Harboring Cancer Cells. Chem. Biol. 15, 234–245 (2008).

26. Yang, W. S. et al. Regulation of Ferroptotic Cancer Cell Death by GPX4. Cell 156, 317–331 (2014).

27. Haeggström, J. Z. & Funk, C. D. Lipoxygenase and leukotriene pathways: Biochemistry, biology, and roles in disease. Chem. Rev. 111, 5866–5896 (2011).

28. Vandenabeele, P., Galluzzi, L., Vanden Berghe, T. & Kroemer, G. Molecular mechanisms of necroptosis: An ordered cellular explosion. Nat. Rev. Mol. Cell Biol. 11, 700–714 (2010).

29. Christofferson, D. E. & Yuan, J. Necroptosis as an alternative form of programmed cell death. Curr. Opin. Cell Biol. 22, 263–268 (2010).

30. Xie, Y. et al. Ferroptosis: Process and function. Cell Death Differ. 23, 369–379 (2016).

31. Deschamps, J. D., Kenyon, V. A. & Holman, T. R. Baicalein is a potent in vitro inhibitor against both reticulocyte 15-human and platelet 12-human lipoxygenases. Bioorganic Med. Chem. 14, 4295–4301 (2006).

32. Rai, G. et al. Potent and selective inhibitors of human reticulocyte 12/15-lipoxygenase as anti-stroke therapies. J. Med. Chem. 57, 4035–4048 (2014).

33. Luci, D. K. et al. Synthesis and structure-activity relationship studies of 4-((2-hydroxy-3-methoxybenzyl)amino)benzenesulfonamide derivatives as potent and selective inhibitors of 12-lipoxygenase. J. Med. Chem. 57, 495–506 (2014).

34. Suzuki, H. et al. Hinokitiol, a selective inhibitor of the platelet-type isozyme of arachidonate 12-lipoxygenase. Biochem. Biophys. Res. Commun. 275, 885–889 (2000).

35. Jameson, J. B. et al. A high throughput screen identifies potent and selective inhibitors to human epithelial 15-lipoxygenase-2. PLoS One 9, e104094 (2014).

36. Armstrong, M. Lipoxygenase Investigations Lead to the Discovery of Potent Inhibitors and their Mechanisim of Action. (University of California Santa Cruz, 2016).

37. Grillo, A. S. et al. Restored iron transport by a small molecule promotes absorption and hemoglobinization in animals. Science, 356, 608–616 (2017).

38. Kritis, A. A., Stamoula, E. G., Paniskaki, K. A. & Vavilis, T. D. Researching glutamate - induced cytotoxicity in different cell lines: a comparative/collective analysis/study. Front. Cell. Neurosci. 9, 1–18 (2015).

39. Haidasz, E. A., Van Kessel, A. T. M. & Pratt, D. A. A continuous visible light spectrophotometric approach to accurately determine the reactivity of radical-trapping antioxidants. J. Org. Chem. 81, 737–744 (2016).

40. Edward, J. T. & Nielsen, S. 1014. Thiohydantoins. Part I. Ionisation and ultraviolet absorption. J. Chem. Soc. 5075–5079 (1957).

41. Zief, M. & Edsall, J. T. Studies in the Physical Chemistry of Amino Acids, Peptides, and Related Substances. IX. The Dissociation Constants of Some Amino Acid Derivatives. J. Am. Chem. Soc. 59, 2245–2248 (1937).

42. Naguib, Y. M. A. A fluorometric method for measurement of peroxyl radical scavenging activities of lipophilic antioxidants. Anal. Biochem. 265, 290–298 (1998).

43. Drummen, G. P. C., Van Liebergen, L. C. M., Op den Kamp, J. A. F. & Post, J. A. C11-BODIPY581/591, an oxidation-sensitive fluorescent lipid peroxidation probe: (Micro)spectroscopic characterization and validation of methodology. Free Radic. Biol. Med. 33, 473–490 (2002).

44. Gao, M., Monian, P., Quadri, N., Ramasamy, R. & Jiang, X. Glutaminolysis and Transferrin Regulate Ferroptosis. Mol. Cell 59, 298–308 (2015).

45. Kenyon, V. et al. Discovery of potent and selective inhibitors of human platelet-type 12-lipoxygenase. J. Med. Chem. 54, 5485–5497 (2011).

46. Dolma, S., Lessnick, S. L., Hahn, W. C. & Stockwell, B. R. Identification of genotype-selective antitumor agents using synthetic lethal chemical screening in engineered human tumor cells. Cancer Cell 3, 285–296 (2003).

47. Stockwell, B. R. et al. Ferroptosis: A Regulated Cell Death Nexus Linking Metabolism, Redox Biology, and Disease. Cell 171, 273–285 (2017).

48. Li, J. et al. Ferroptosis: past, present and future. Cell Death Dis. 11, 88 (2020).

49. Soula, M. et al. Metabolic determinants of cancer cell sensitivity to canonical ferroptosis inducers. Nat. Chem. Biol. 16, 1351–1360 (2020).

50. Ingold, K. U. & Pratt, D. A. Advances in radical-trapping antioxidant chemistry in the 21st century: A kinetics and mechanisms perspective. Chem. Rev. 114, 9022–9046 (2014).

51. Barckholtz, C., Barckholtz, T. A. & Hadad, C. M. C-H and N-H bond dissociation energies of small aromatic hydrocarbons. J. Am. Chem. Soc. 121, 491–500 (1999).

52. Poon, J. F. & Pratt, D. A. Recent Insights on Hydrogen Atom Transfer in the Inhibition of Hydrocarbon Autoxidation. Acc. Chem. Res. 51, 1996–2005 (2018).

53. Süzen, S., Demírcígíl, B. T., Buyukbingol, E. & Özkan, S. A. Electroanalytical evaluation and determination of 5-(3′-indolyl)-2-thiohydantoin derivatives by voltammetric studies: Possible relevance to in vitro metabolism. New J. Chem. 27, 1007–1011 (2003).

54. Simic, M. G. & Jovanovic, S. V. Antioxidation mechanisms of uric acid. J. Am. Chem. Soc. 111, 5778–5782 (1989).

55. Zhang, X., Wang, C., Jiang, H. & Sun, L. Convenient synthesis of selenyl-indoles via iodide ion-catalyzed electrochemical C-H selenation. Chem. Commun. 54, 8781–8784 (2018).

56. Pegis, M. L. et al. Standard Reduction Potentials for Oxygen and Carbon Dioxide Couples in Acetonitrile and N,N-Dimethylformamide. Inorg. Chem. 54, 11883–11888 (2015).

57. Stott, L. A., Prosser, K. E., Berdichevsky, E. K., Walsby, C. J. & Warren, J. J. Lowering water oxidation overpotentials using the ionisable imidazole of copper(2-(2′-pyridyl)imidazole). Chem. Commun. 53, 651–654 (2017).

2.7 Appendix

Raw data for all results reported in **Section 2.7.1** was reported by Lab Member Katie Shirley except for the "No L-Gln" data reported in **Figure 2.17**.

2.7.1 Glutamate- and Erastin-treated Dose-Response Curves for HT-22 and HT-1080

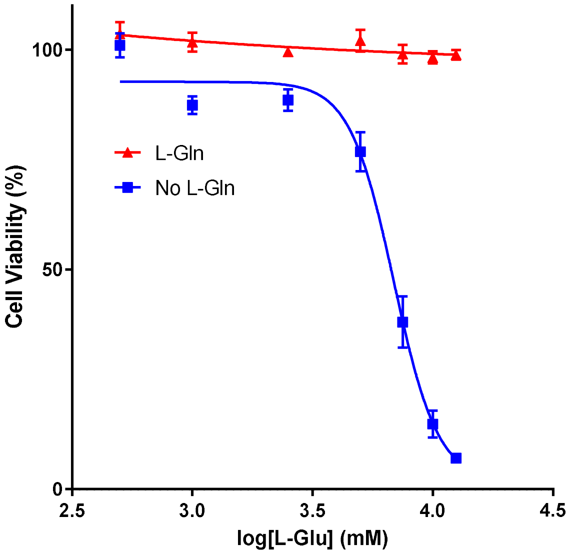

Figure 2.17 Sensitization of HT-22 cells to varying concentrations of L-Glu over a 24 hour exposure period, cultured with and without media containing 10 mM L-Gln. Cell viability was assessed using AquaBluer treatment.

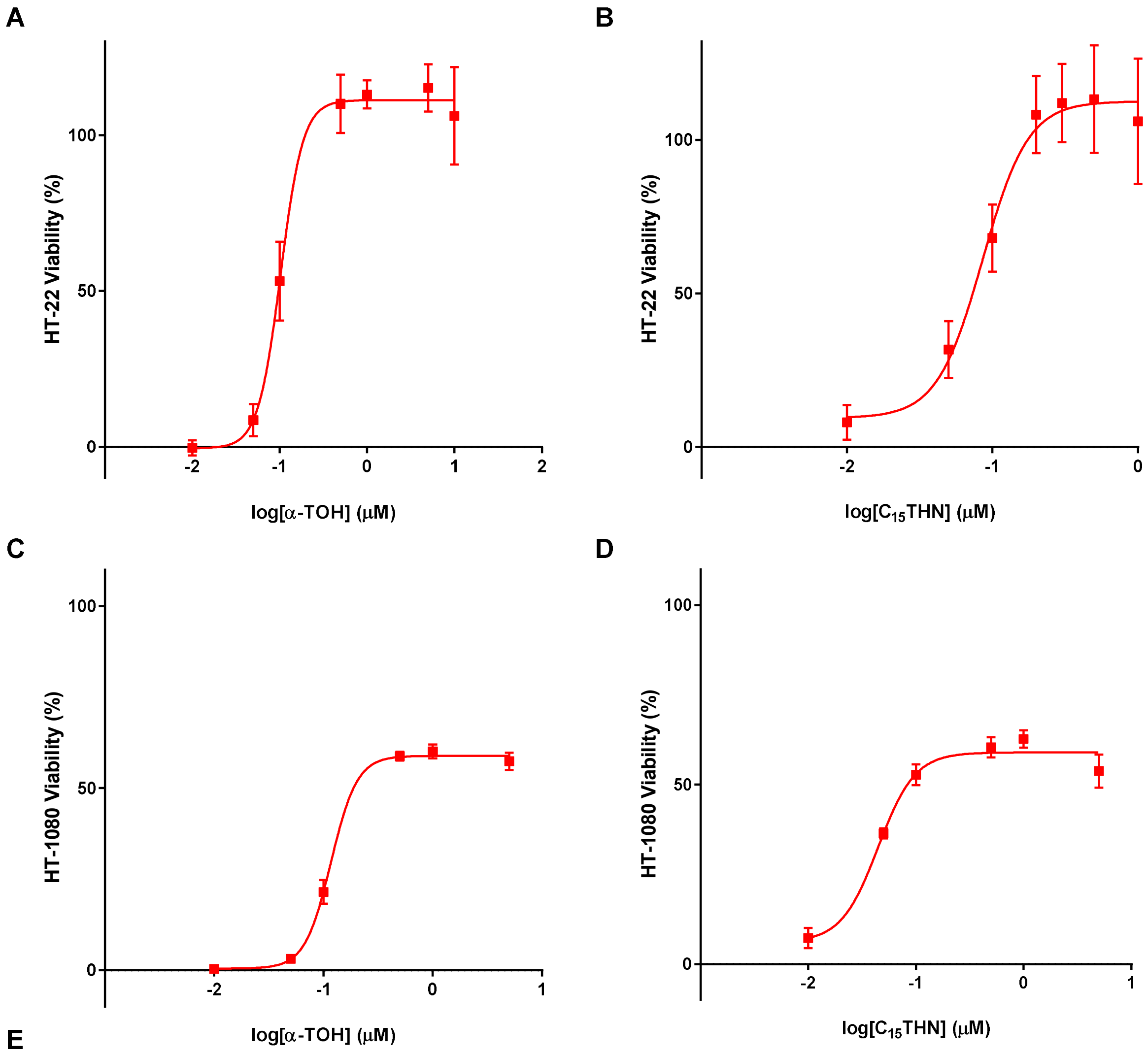

E

IC$_{50}$ (μM)

	α-TOH	C$_{15}$THN
HT-22	0.11	0.090
HT-1080	0.32	0.045

Figure 2.18 Dose-response curves for HT-22 and HT-1080 cells treated with 10 mM glutamate and 10 μM erastin, respectively, and varying concentrations of α-TOH (**A** (HT-22) and **C** (HT-1080)) and C$_{15}$THN (**B** (HT-22) and **D** (HT-1080)), and their corresponding results (**E**).

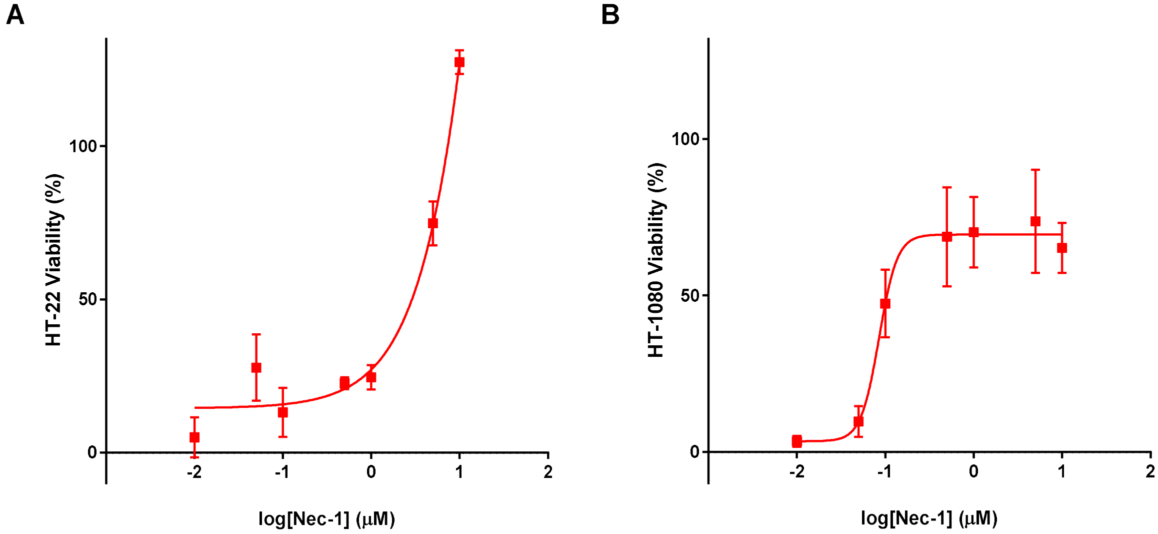

C

	IC_{50} (μM)
HT-22	5.0*
HT-1080	0.085

*Estimated value, rescue insufficient to generate an IC_{50}

Figure 2.19 Dose-response curves for Nec-1 in HT-22 and HT-1080 cells treated with 10 mM glutamate and 10 μM erastin, respectively, and varying concentrations of Nec1 (**A** (HT-22) and **B** (HT-1080)), and their corresponding results (**C**).

2.7.2 Nec-1 Dose-Response Curves in HT-22 Cells

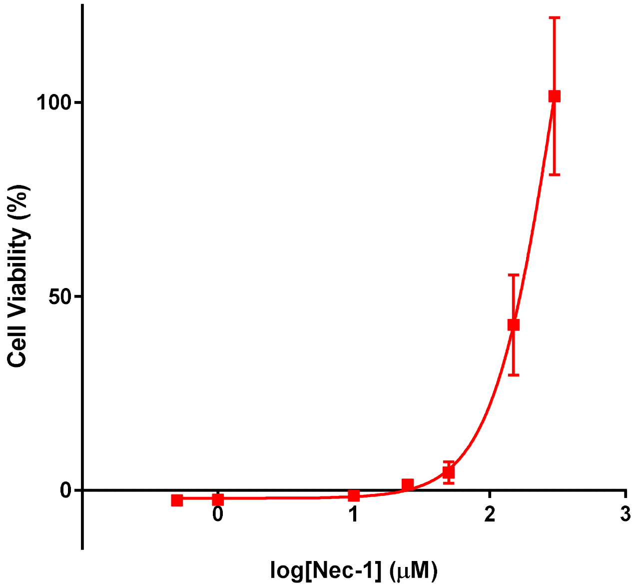

Figure 2.20 Dose-response curve of HT-22 cells treated with 0.80 μM RSL3 and varying concentrations of Nec-1 over a 4 hour exposure, cell viability was assessed using AquaBluer treatment.

2.7.3 Liposome Coautoxidation of Nec-1 (Higher concentration)

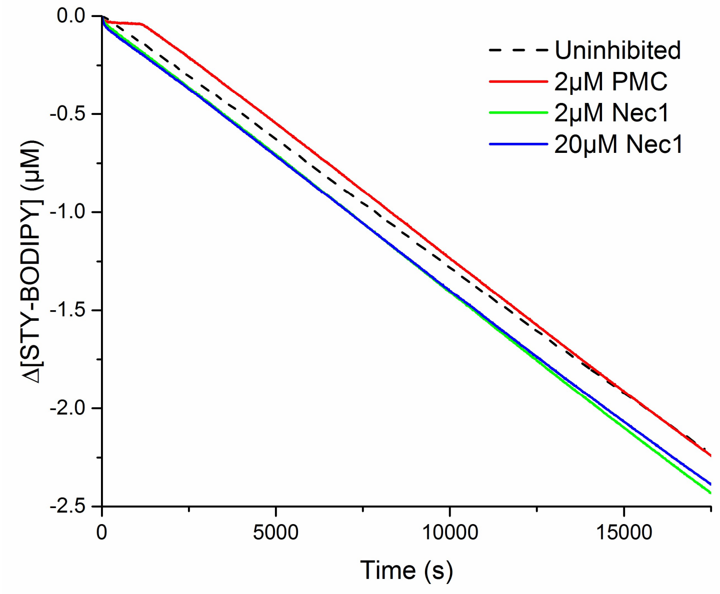

Figure 2.21 RTA activity of Nec-1, measured by coautoxidation of STY-BODIPY at 30 °C in liposomes. Performed at 2.0 and 20.0 μM concentration, with uninhibited and 2.0 μM PMC controls.

2.7.4 Cyclic Voltammograms (CV)

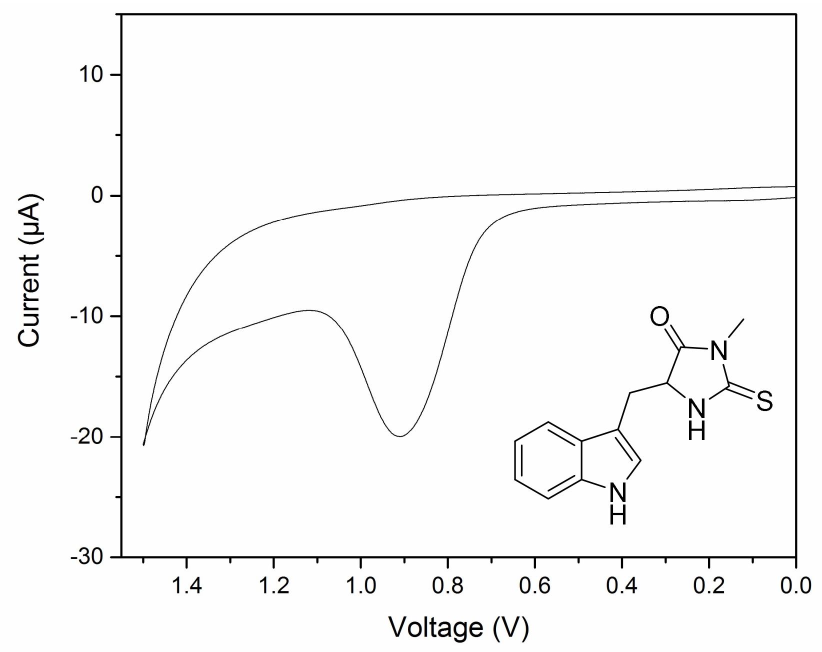

Figure 2.22 CV of Nec-1 vs. Ag/Ag$^+$ in 0.1 M NBu_4PF_6 buffered MeCN solution. E^o = 1.45 V vs. NHE.

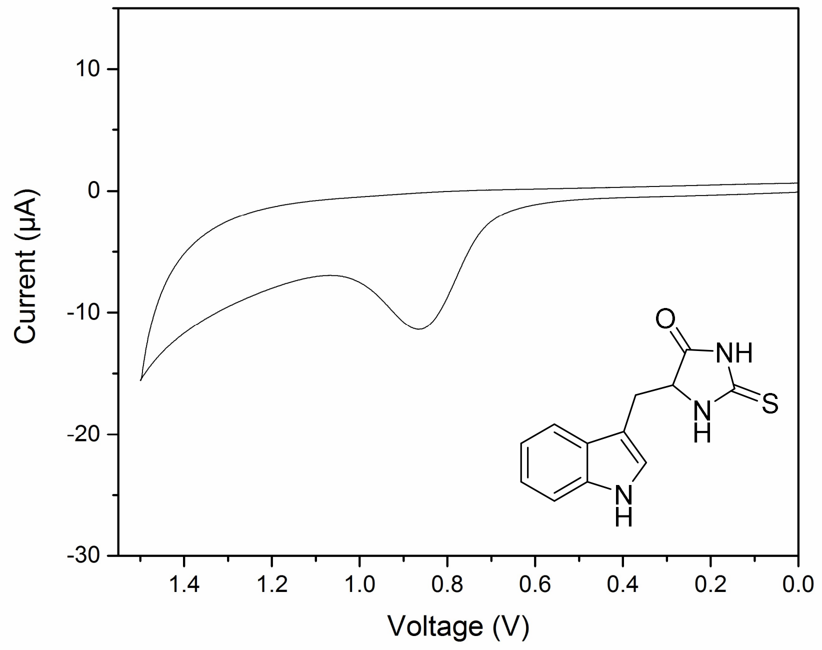

Figure 2.23 CV of Nec-1i vs. Ag/Ag$^+$ in 0.1 M NBu_4PF_6 buffered MeCN solution. E^o = 1.40 V vs. NHE.

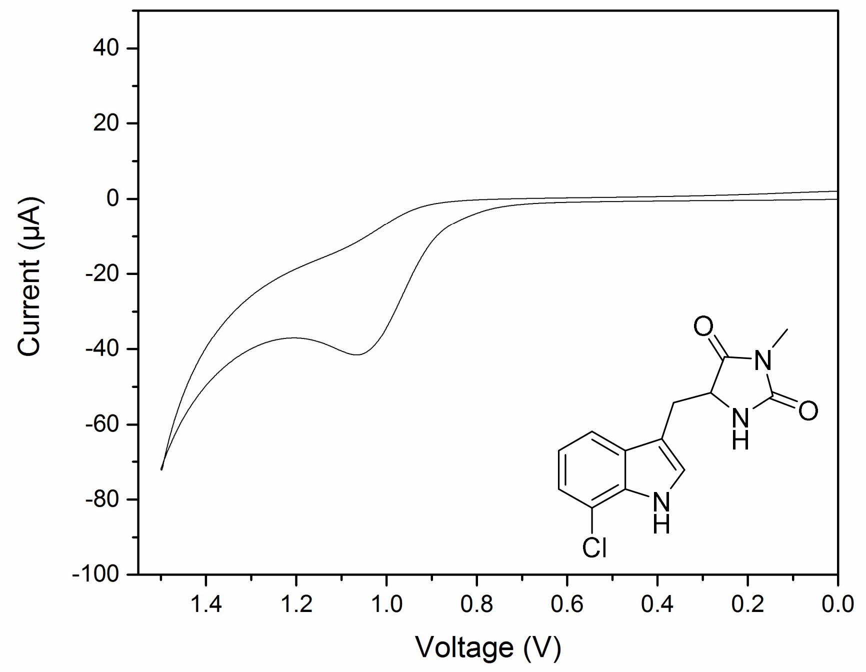

Figure 2.24 CV of Nec-2 vs. Ag/Ag$^+$ in 0.1 M NBu_4PF_6 buffered MeCN solution. E° = 1.60 V vs. NHE.

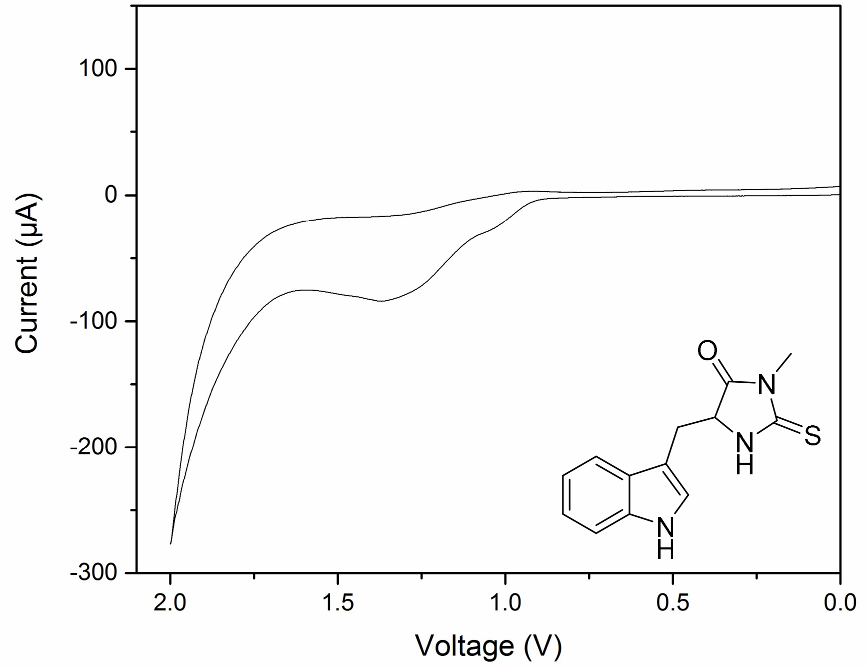

Figure 2.25 CV of Nec-1 vs. Ag/Ag$^+$ in distilled water containing 3 M KCl and 10mM potassium phosphate buffer, pH = 7.4. E° = 1.24 V and 1.53 V vs. NHE.

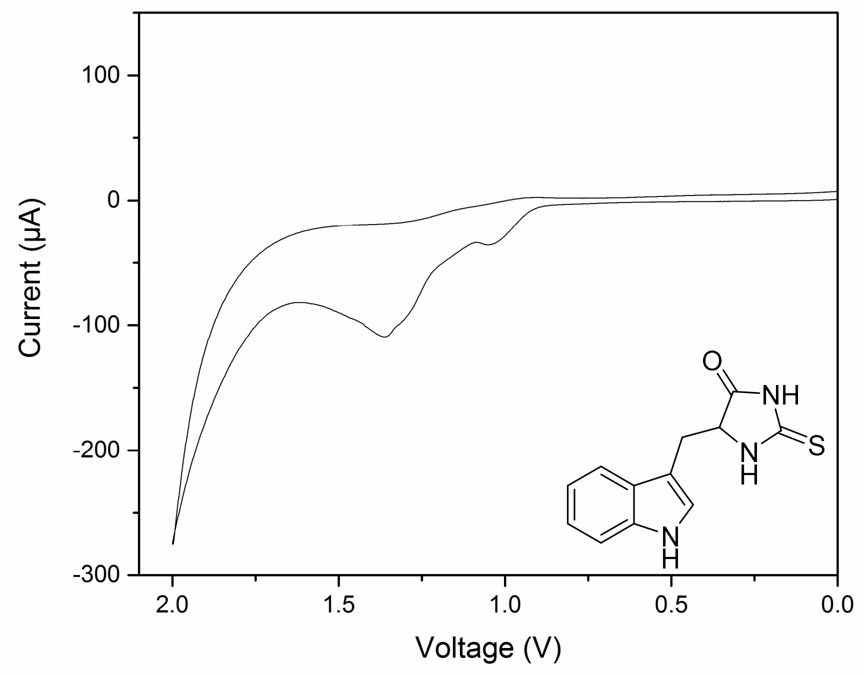

Figure 2.26 CV of Nec-1i vs. Ag/Ag$^+$ in distilled water containing 3 M KCl and 10mM potassium phosphate buffer, pH = 7.4. E° = 1.21 V and 1.52 V vs. NHE.

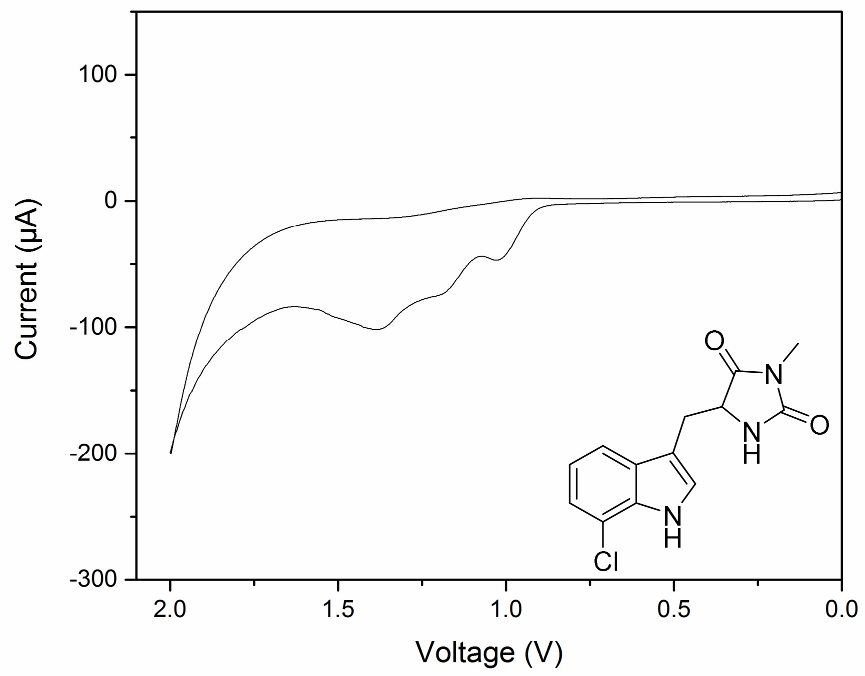

Figure 2.27 CV of Nec-2 vs. Ag/Ag$^+$ in distilled water containing 3 M KCl and 10 mM potassium phosphate buffer, pH = 7.4. E° = 1.19 V, 1.36 V, and 1.54 V vs. NHE.

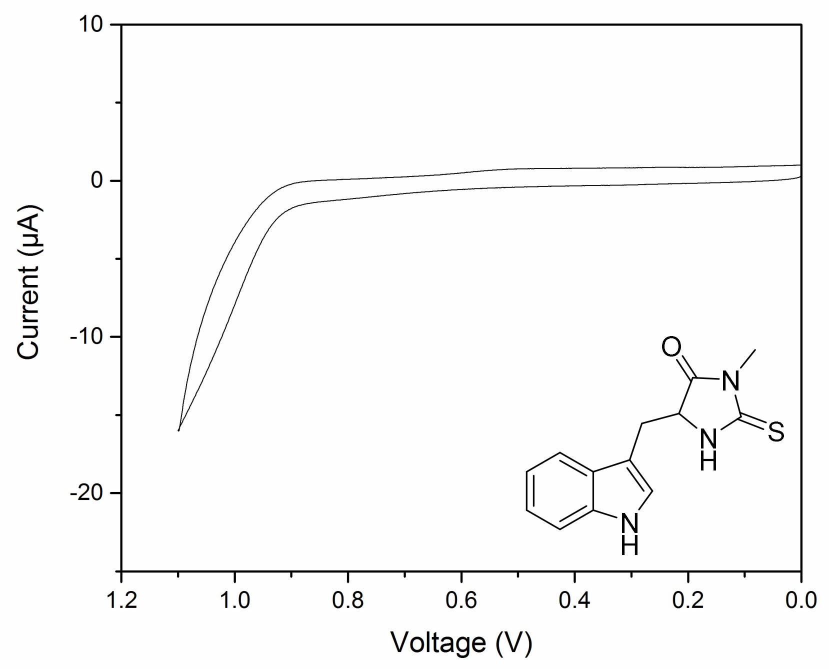

Figure 2.28 CV of Nec-1 vs. Ag/Ag$^+$ in distilled water containing 3 M KCl and 10 mM potassium phosphate buffer, pH = 7.4. Upper bounds set to 1100 mV.

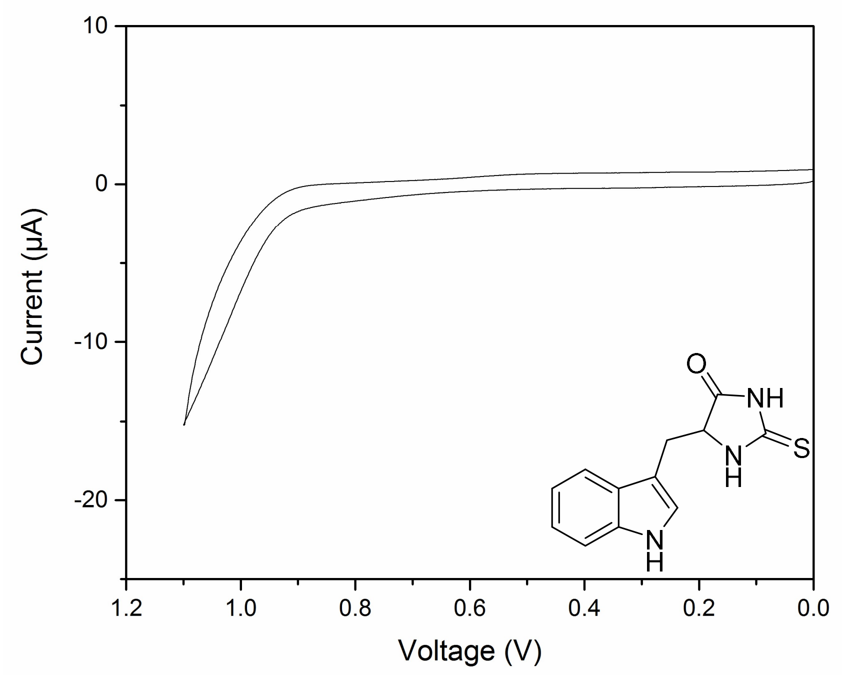

Figure 2.29 CV of Nec-1i vs. Ag/Ag$^+$ in distilled water containing 3 M KCl and 10 mM potassium phosphate buffer, pH = 7.4. Upper bounds set to 1100 mV.

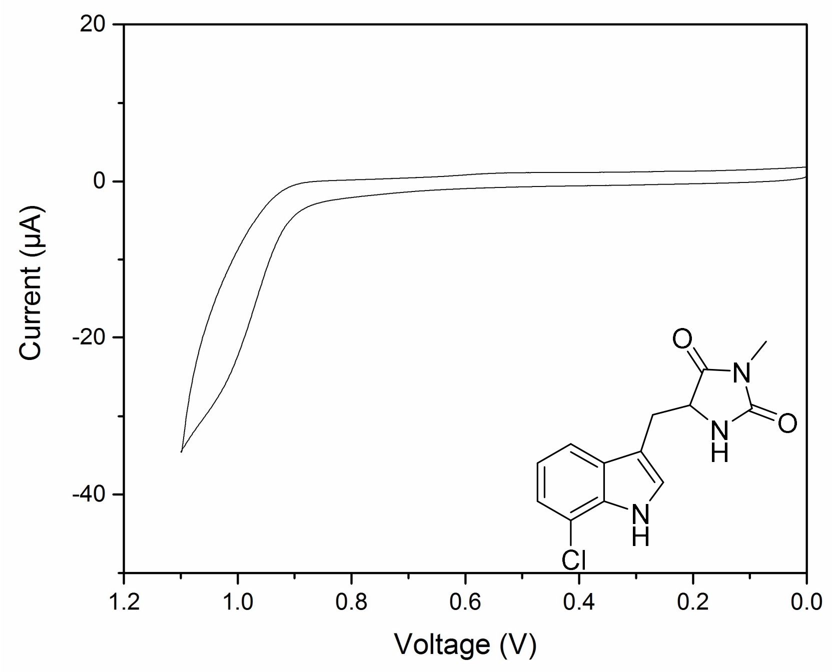

Figure 2.30 CV of Nec-2 vs. Ag/Ag$^+$ in distilled water containing 3 M KCl and 10 mM potassium phosphate buffer, pH = 7.4. Upper bounds set to 1100 mV.

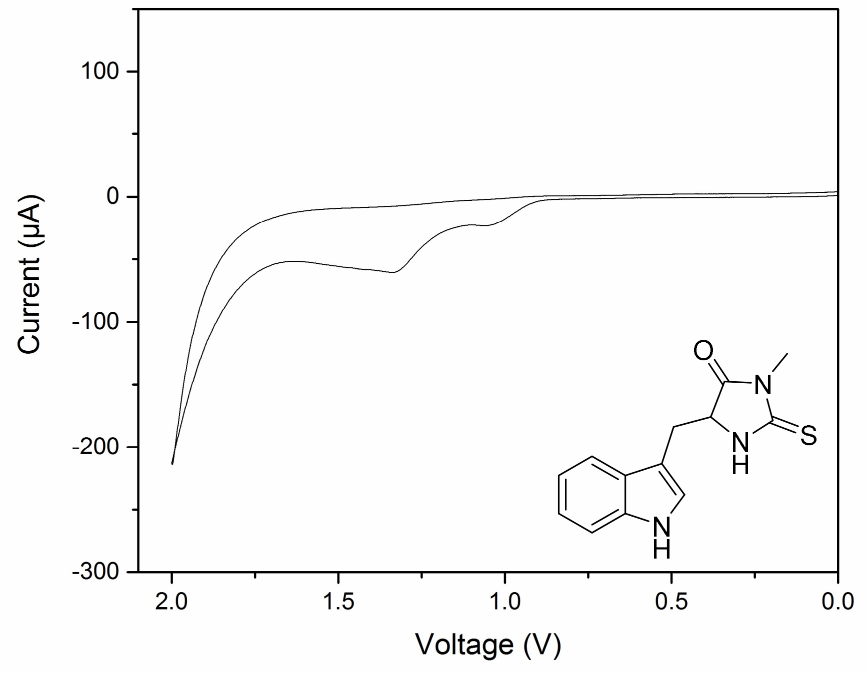

Figure 2.31 CV of Nec-1 vs. Ag/Ag$^+$ in distilled water containing 3 M KCl and 10 mM potassium borate buffer, pH = 8.5. E° = 1.23 V and 1.51 V vs. NHE.

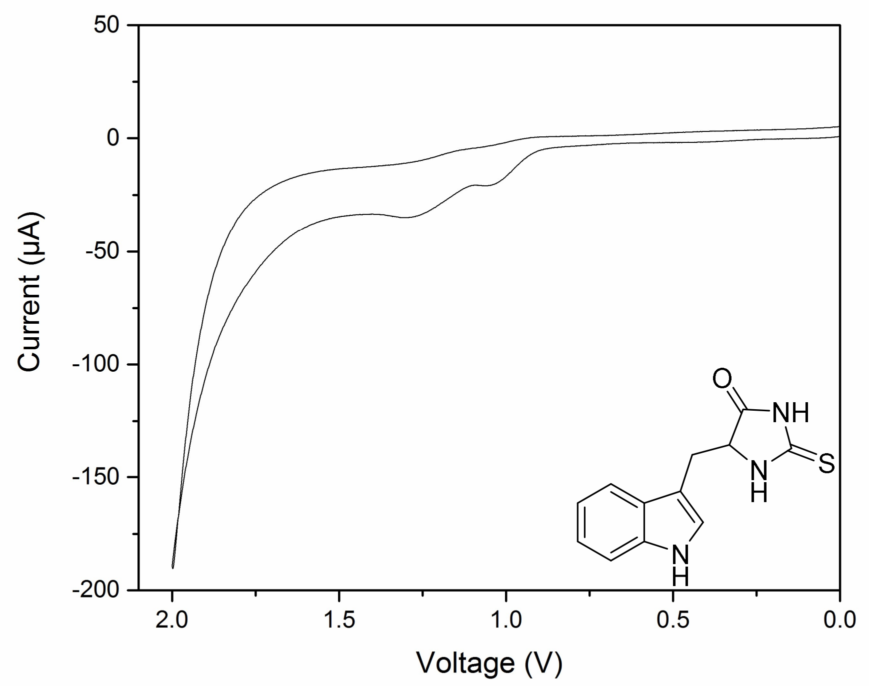

Figure 2.32 CV of Nec-1i vs. Ag/Ag$^+$ in distilled water containing 3 M KCl and 10 mM potassium borate buffer, pH = 8.5. E° = 1.23 V and 1.47 V vs. NHE.

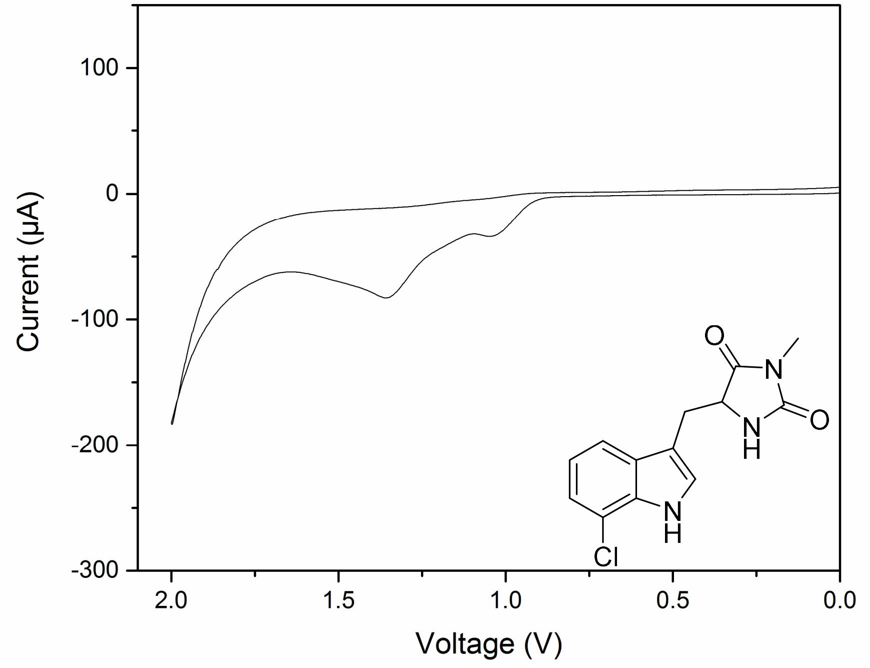

Figure 2.33 CV of Nec-2 vs. Ag/Ag$^+$ in distilled water containing 3 M KCl and 10 mM potassium borate buffer, pH = 8.5. E° = 1.22 V and 1.53 V vs. NHE.

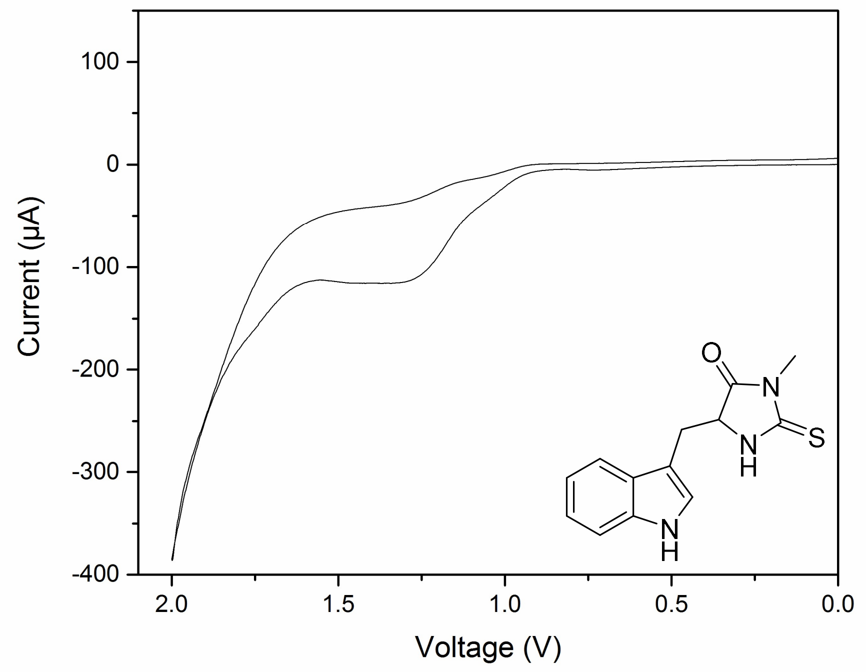

Figure 2.34 CV of Nec-1 vs. Ag/Ag$^+$ in distilled water containing 3 M KCl and 10 mM potassium borate buffer, pH = 10.0. E° = 1.50 V vs. NHE.

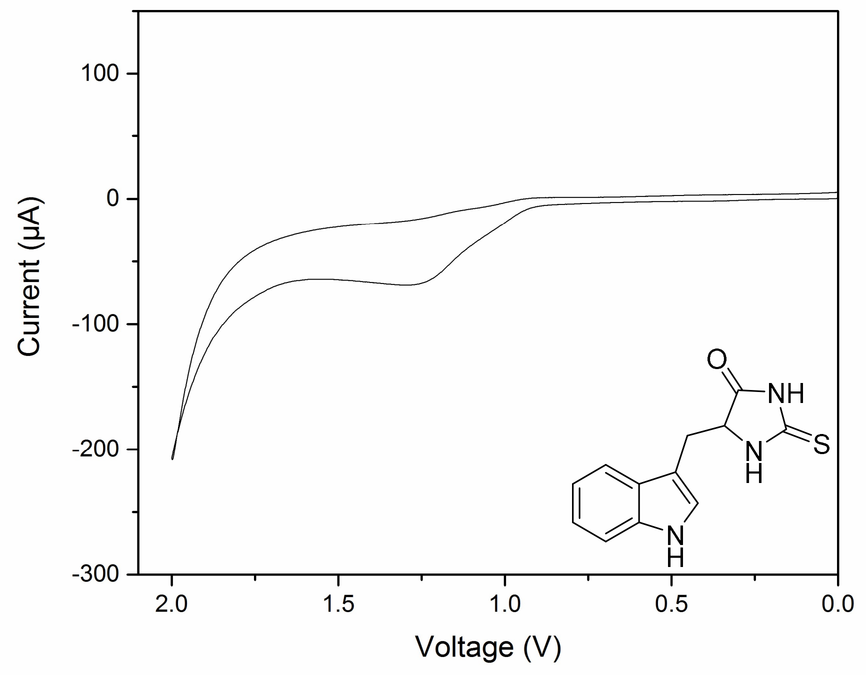

Figure 2.35 CV of Nec-1i vs. Ag/Ag$^+$ in distilled water containing 3 M KCl and 10 mM potassium borate buffer, pH = 10.0. E° = 1.45 V vs. NHE.

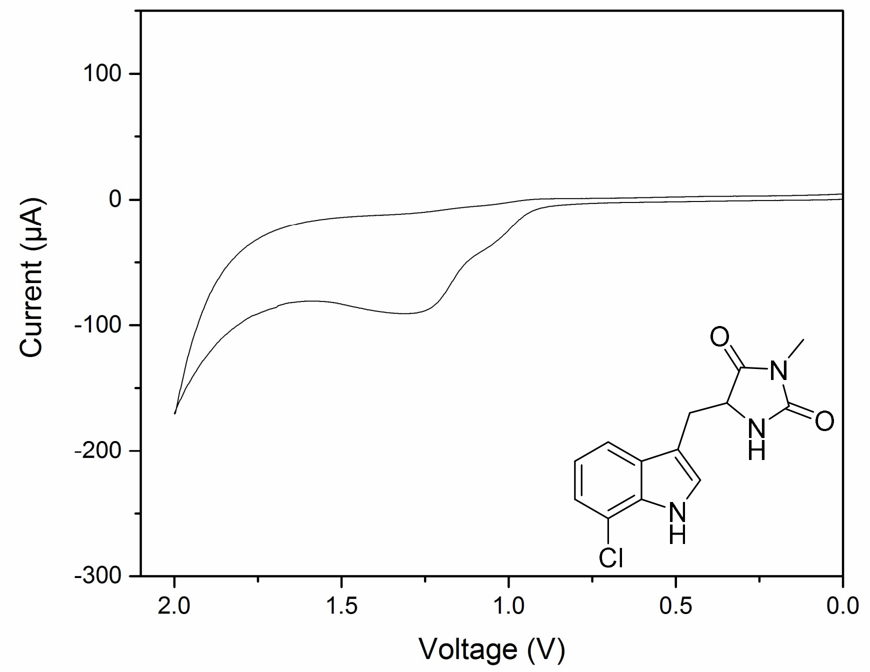

Figure 2.36 CV of Nec-2 vs. Ag/Ag$^+$ in distilled water containing 3 M KCl and 10 mM potassium borate buffer, pH = 10.0. E° = 1.48 V vs. NHE.

CHAPTER 3 On the Mechanism Behind α-Eleostearic Acid Autoxidation

3.1 Introduction

Autoxidation is the result of oxidative stress within cellular environments.[1] Easily oxidizable substrates facilitate efficient propagation of radical chain reactions leading to the accumulation of peroxidic products, which can disrupt normal cell function resulting in cell death (i.e. ferroptosis) and degenerative diseases (e.g. Alzheimer's).[2,3] Within lipid bilayers, polyunsaturated fatty acids (PUFAs) serve as easily oxidizable substrates for propagating radicals and can be differentiated by their homoconjugated or conjugated functionality (**Figure 3.1**). Homoconjugated PUFAs are characterized by bisallylic H-atoms, which are readily abstractable via HAT during autoxidation and also serve as substrates to oxidation-promoting enzymes (e.g. LOX) to produce peroxyl radicals.[1,4] The low BDE of bisallylic C-H bonds and high solubility in cellular membranes confers a pro-ferroptotic effect, observed during supplementation of cell culture media with arachidonic and linoleic acid, which promote the accumulation of lipid hydroperoxides and sensitize cells to RSL3-induced ferroptosis.[5] While the mechanism and role of homoconjugated PUFAs in lipid peroxidation is relatively well understood, conjugated PUFAs have received considerably less attention.

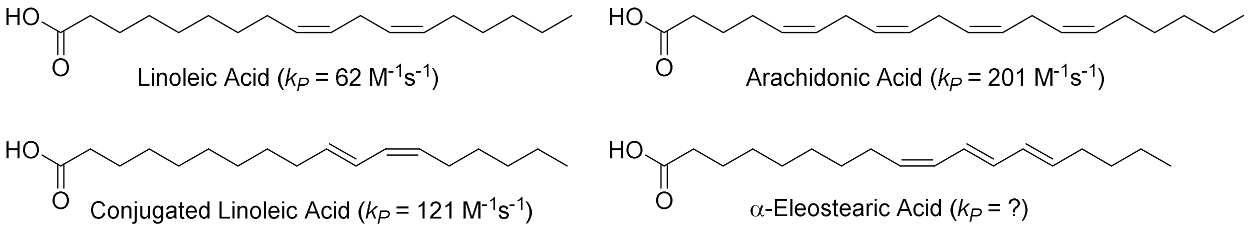

Linoleic Acid (k_P = 62 $M^{-1}s^{-1}$)

Arachidonic Acid (k_P = 201 $M^{-1}s^{-1}$)

Conjugated Linoleic Acid (k_P = 121 $M^{-1}s^{-1}$)

α-Eleostearic Acid (k_P = ?)

Figure 3.1 Chemical structures of homoconjugated (top) and conjugated (bottom) PUFAs. Literature propagation rate constants at 37 °C have been included.[6,7]

α-Eleostearic acid (α-ESA), a fatty acid possessing a conjugated triene functionality, has displayed pro-ferroptotic activity *in vitro* and *in vivo*. α-ESA induces ferroptosis in triple-negative breast cancer (TNBC) cells[8] and has demonstrated anti-tumorigenic effects in mouse xenografts.[9] Most importantly, these studies report α-ESA acting as an initiator of ferroptosis, unlike homoconjugated PUFAs which simply sensitize cells to ferroptotic cell death and still require conventional initiation (e.g. GPX4 inhibition with RSL3). The conjugated trienic unit of α-ESA appears central to its unique ferroptotic-initiative function, an effect unobserved in analogous dienes, initiating ferroptosis by a pathway separate from traditional GSH depletion or GPX4 inhibition.[8] The established sensitivity of PUFAs towards autoxidation suggests α-ESA-induced initiation may affect lipid peroxidation via heightened reactivity or alternatively by a mechanism distinct from homoconjugated PUFAs. Although HAT is feasible at its allylic sites, α-ESA lacks the bisallylic sites at which HAT is most prominently observed (as shown via methyl linoleate (ML) in **Scheme 1.6**). Contrasting the C-H BDE of the terminal methyl of 1,3-pentadiene to the central methylene of 1,4-pentadiene (a difference of 7.1 kcal/mol), suggests conjugated systems are less efficient a substrate for HAT (**Figure 3.2**).[10] In fact, propagation by addition has been observed in conjugated lipid substrates, for example, in the conjugated diene hydroperoxide products of ML.[11] α-ESA presents as highly oxidizable, constituting ~80% of the composition of Tung oil, used industrially in wood finish, paints, and varnish due to its fast-drying properties.[12] Furthermore, α-ESA has been shown to oxidize at a greater rate than that of linoleate, by an autoxidative mechanism not yet confirmed.[13]

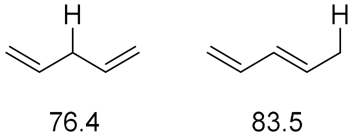

Figure 3.2 C-H bond dissociation energies for 1,4-pentadiene methylene and 1,3-pentadiene methyl groups (in kcal/mol).[10]

HAT is the most common mechanism by which lipid peroxidation is propagated; however, conjugated lipids may also propagate by addition.[1] Preliminary results suggesting dimerization and radical propagation by addition of the *trans*-isomer β-eleostearic acid (β-ESA), an analog of comparable reactivity, were reported in the 1940s.[14] Herein, we propose experiments to investigate the predominant mechanism of propagation for α-ESA under physiologically relevant conditions (**Figure 3.3A**). α-ESA will react with a peroxyl radical by addition to form a dialkylperoxide with a pendant pentadienyl radical, which will rapidly react with molecular oxygen to yield a new peroxyl radical. The peroxyl could then either add to an additional α-ESA molecule, or abstract an H-atom from another PUFA. Propagation by addition may explain the ferroptosis-initiating effect α-ESA possesses over homoconjugated PUFAs. Hydroperoxyl groups are easily reduced to alcohols by the enzyme GPX4, preventing their accumulation; however, dialkylperoxides are not a substrate of GPX4 and would persist (**Figure 3.3B**).[15] Dialkylperoxides may instead be expected to decompose via Fenton-like chemistry, inducing further lipid peroxidation even in the presence of functional GPX4 and an abundance of its reducing co-substrate GSH. Clarifying the mechanism of propagation for α-ESA would provide insight into its pro-ferroptotic activity. Once this is understood, the ability of α-ESA to act as a ferroptosis-initiative agent may enable the design of novel drugs or chemotherapeutics for ferroptosis-related disease.

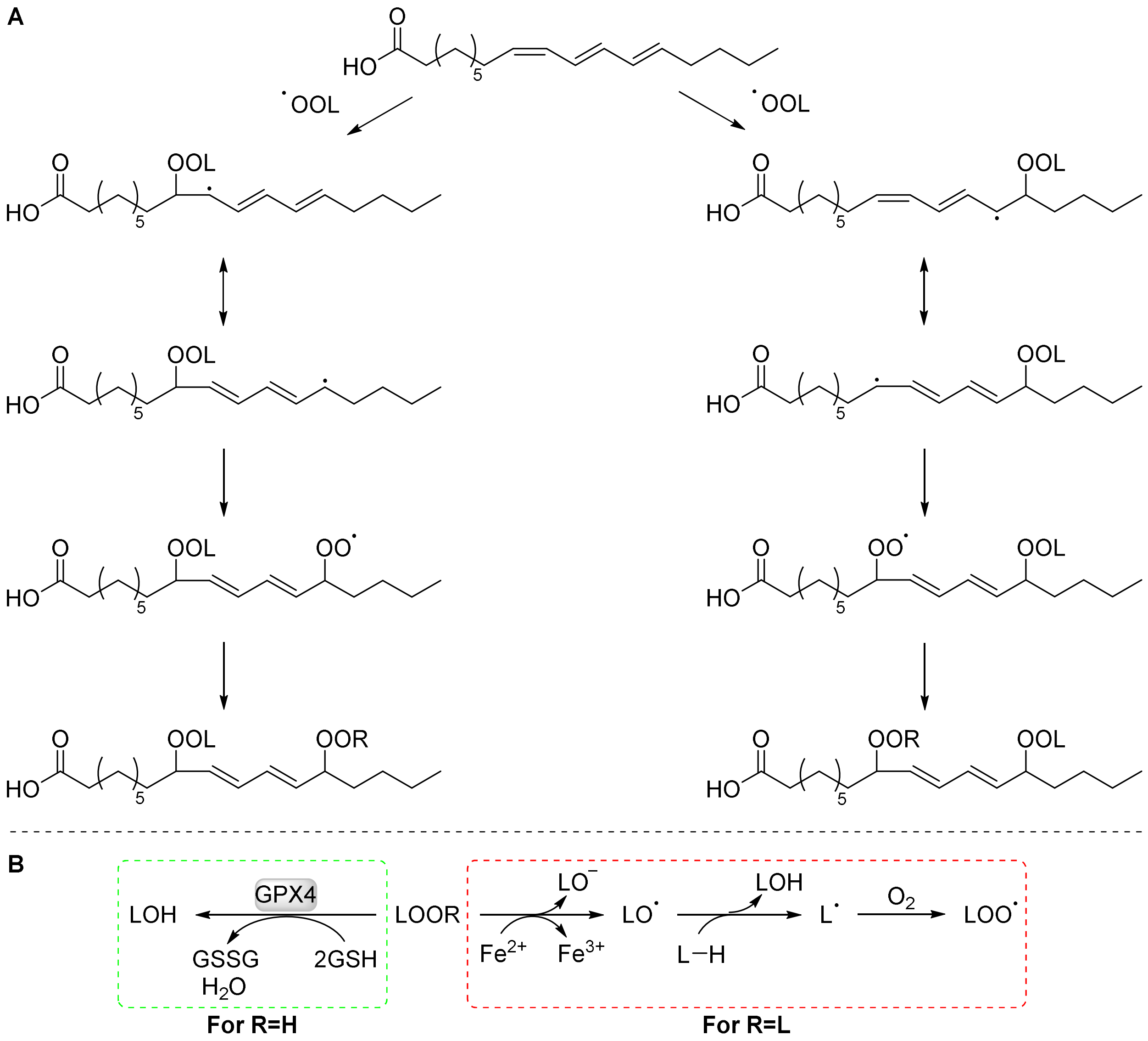

Figure 3.3 Proposed autoxidative pathway for α-ESA by addition (**A**) and resulting enzymatic and non-enzymatic metabolism of products (**B**), where L = PUFA addition product.

A large deuterium kinetic isotope effect (KIE) is observed in the autoxidation of homoconjugated PUFAs deuterated at the methylene functionality, suppressing the rate of HAT by peroxyl radicals.[16] This effect is translatable to the cell environment, and deuteration of homoconjugated PUFAs decreases their pro-ferroptotic potency.[5,17] Since a primary KIE would not be observed for peroxyl radical addition, deuteration of the methylene functionalities flanking the trienic moiety would not significantly impact rate of addition. Thus, in order to establish the primary mechanism of α-ESA autoxidation, we propose to synthesize 8,8,15,15-d_4-α-ESA (d_4-α-ESA), an analogous lipid deuterated at the allylic sites prone to HAT (**Figure 3.4)**. Provided addition is the rate-determining step of α-ESA propagation, we would expect no change in rate of autoxidation or ferroptotic activity between isotopologues.

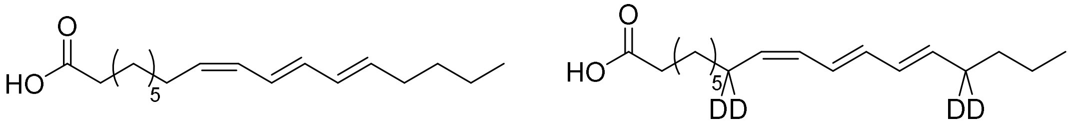

Figure 3.4 Chemical structures of natural α-ESA (left) and 8,8,15,15-d_4-α-ESA possessing deuterium at allylic sites (right) of its characteristic (9*Z*, 11*E*, 13*E*) trienic unit.

The proposed synthesis of d_4-α-ESA is based on a reported synthesis of unlabelled α-ESA.[18] As reported, 1-hexyne undergoes hydroalumination and successive substitution on *trans*-1,2-dichloroethylene to form an (*E*,*E*)-chlorodiene. Subsequent treatment with a terminal alkyne yields a dienyne which can be reduced to the triene for an overall reported 48% yield of the (*E*,*Z*,*Z*) isomer. We sought to prepare appropriately deuterated precursors and carry out the reported synthesis as in **Scheme 3.1**.

Scheme 3.1 Proposed synthesis of 8,8,15,15-d_4-α-ESA.[18]

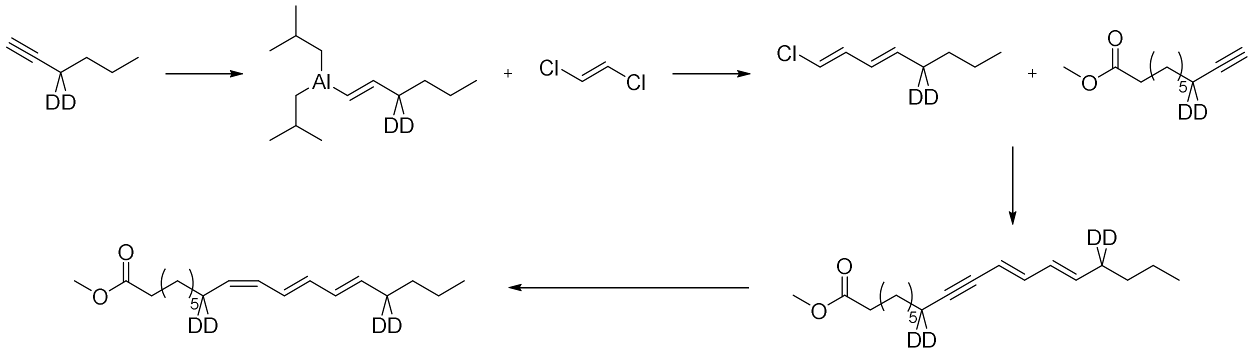

Herein, we report our efforts to date, which include the synthesis of methyl 8,8-d_2-dec-9-ynoate and near-complete synthesis of 3,3-d_2-1-hexyne, the precursors required to carry out d_4-α-ESA synthesis (**Scheme 3.2**). Deuterium-labelled alkynes have been previously prepared by reduction of organic acids to their respective alcohols using $LiAlD_4$ as a reducing and deuterating agent (and subsequent bromination and ethynylation),[19] unfortunately no longer commercially available. Given reports that aldehydic α-carbons can be deuterated in the presence of a weak base,[20] we envisioned that both alkynes could be prepared from respective deuterated-aldehydic precursors by use of the Ohira-Bestmann reagent while leaving the ester group intact. Lastly, methyl 9-oxononanoate could be prepared by Fischer esterification and subsequent ozonolysis of oleic acid.

Scheme 3.2 Retrosynthetic proposal for 3,3-d_2-1-hexyne (**A**) and methyl 8,8-d_2-dec-9-ynoate (**B**).

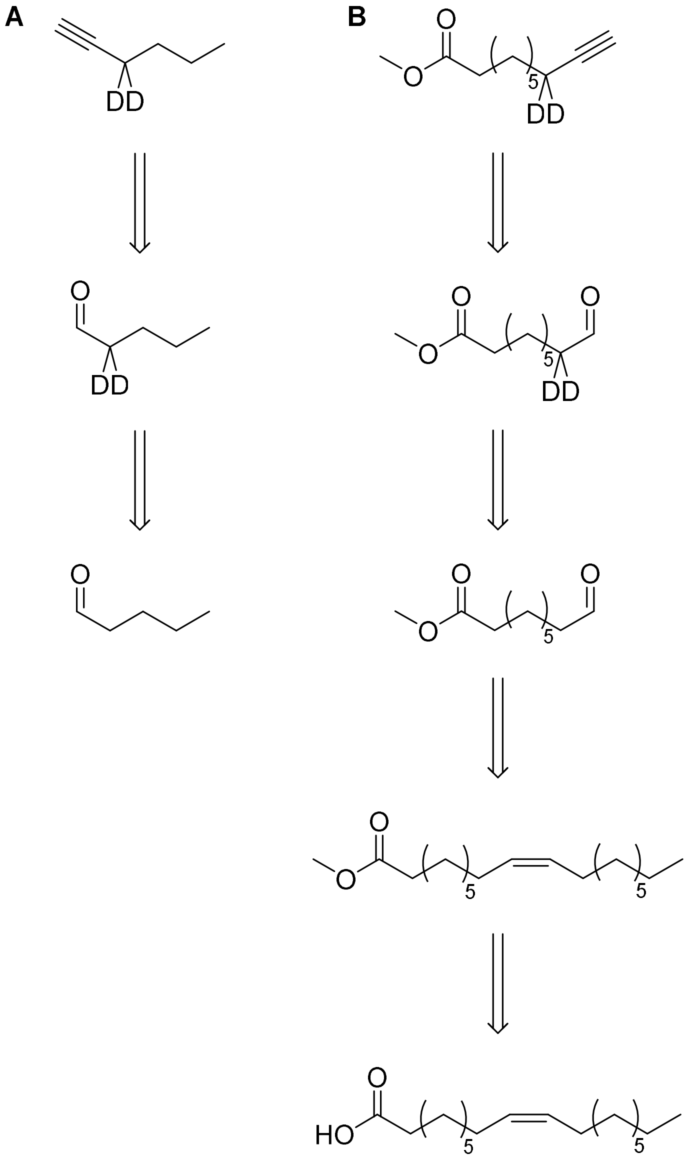

In addition, we describe our initial efforts towards determining propagation rate constants for α-ESA. A review of the literature indicated only minimal kinetic information is available for α-ESA, most of which was reported under non-physiological conditions prior to the 1950s. Herein, we probe the mechanism and rate of autoxidation for α-ESA by implementing ML clocking experiments via HPLC and tracking absorbance via UV-Vis spectrophotometry.

3.2 Results

α-ESA was purified from Tung oil by saponification and recrystallization as described in the Experimental Section (**Section 3.5**).[21] The identity of isolated α-ESA crystals was verified by ^{1}H-NMR (**Figure 3.13**).[22]

3.2.1 Investigations into the Mechanism of α-Eleostearic Acid Autoxidation

A ML peroxyl radical clock experimental method was developed using conditions inspired by the peroxyl radical clocking performed by Xu, et al. (2009) and modified to include α-ESA in conjunction with ML.[6,23] Maintaining a 0.2M total lipid concentration in PhCl, α-ESA was included to constitute 0, 1, 2, 5, and 10% of the total lipid present in the autoxidation. The influence of α-ESA was then monitored by tracking 13-*t,t*, 13-*t,c*, 9-*t,t*, and 9-*t,c* hydroperoxide product ratios via absorbance at 235 nm. Variations between the rate and mechanism of ML and α-ESA autoxidation could then be observed by changes in product quantity and ratio.

Measuring the sum of hydroperoxide products indicates that as α-ESA concentration increases, the total quantity of ML hydroperoxide products decreases (**Figure 3.5B**). At the final measured ratio of 10:90 α-ESA:ML, the products of ML autoxidation decreased to less than a third of that measured in a pure ML autoxidation. Loss of α-ESA was also monitored by absorbance at 270 nm indicated that ~70% of α-ESA was consumed in the first hour and ~90% after two hours (**Figure 3.5C**). In order to observe any competing HAT of α-ESA with ML, product formation ratios were tracked over increasing α-ESA concentration at 60, 80, and 120 minutes (**Figure 3.5D**). No changes in the hydroperoxyl product ratios were observed, indicating ML, whose concentration is constant, is the H-atom donor contributing to product formation. Thus, given the literature value for ML propagation rate constant ($k_{p,ML}$ = 62 $M^{-1}s^{-1}$),[24] an upper bound for the α-ESA HAT rate constant can be predicted ($k_{HAT,\alpha\text{-}ESA} < 5.6 * 10^2$ $M^{-1}s^{-1}$) at 37 °C (**Figure 3.5E**). Expanded results for ML product distribution can be found in the SI (**Figure 3.11)**.

To estimate a propagation rate constant for α-ESA, loss of absorbance can be tracked via spectrophotometry over time. Absorbance can then be converted to concentration via Beer-Lambert law using a previously determined extinction coefficient (ε) for the substrate at a given wavelength. We sought to determine our own extinction coefficient, given that literature values for α-ESA were sparse, and measured under different conditions.[25] Absorbance of α-ESA was measured between 200 and 350 nm at concentrations of 4.0, 8.0, 12.0, 16.0, and 20.0 μM in isooctane (**Figure 3.6A**). The observed absorbance maxima (λ_{max} = 270 nm) were then plotted over concentration of α-ESA and slope was determined by linear regression ($R^2 = 0.9999$) (**Figure 3.6B**). Calculating for the extinction coefficient provided a value of $5.1 * 10^4$ $M^{-1}cm^{-1}$ (**Figure 3.6C**).

With the extinction coefficient in hand, we attempted to estimate the propagation rate constant by tracking loss of the trienic unit (λ_{max} = 270 nm) during an autoxidation reaction. The absorbance of α-ESA was measured at 37 °C in isooctane, initiated using [AIBN] = 6 mM, with $[\alpha\text{-ESA}]_{initial}$ = 4.0, 8.0, 12.0, 16.0, and 20.0 μM over nine hours (SI, **Figure 3.12**). The measured absorbance values were then converted to concentration (M) using the extinction coefficient and plotted against time (**Figure 3.7A**). The slope of each initial rate was then estimated by linear regression, reported as line of best fit in **Figure 3.7B** ($R^2 \geq 0.997$). Prior to calculation of a propagation rate constant (k_p), these rates must be validated by determination of chain length ($v = \frac{R_p}{R_i}$), where R_p is the measured initial rate and R_i is known rate of initiation of AIBN at 37 °C ($R_{i,AIBN} = 1.3 * 10^{-9}$ Ms^{-1}),[26] where $v > 1$. Unfortunately at the measured concentration, chain length was substantially below $v = 1$ in all cases, and the values could not be used to estimate k_p.

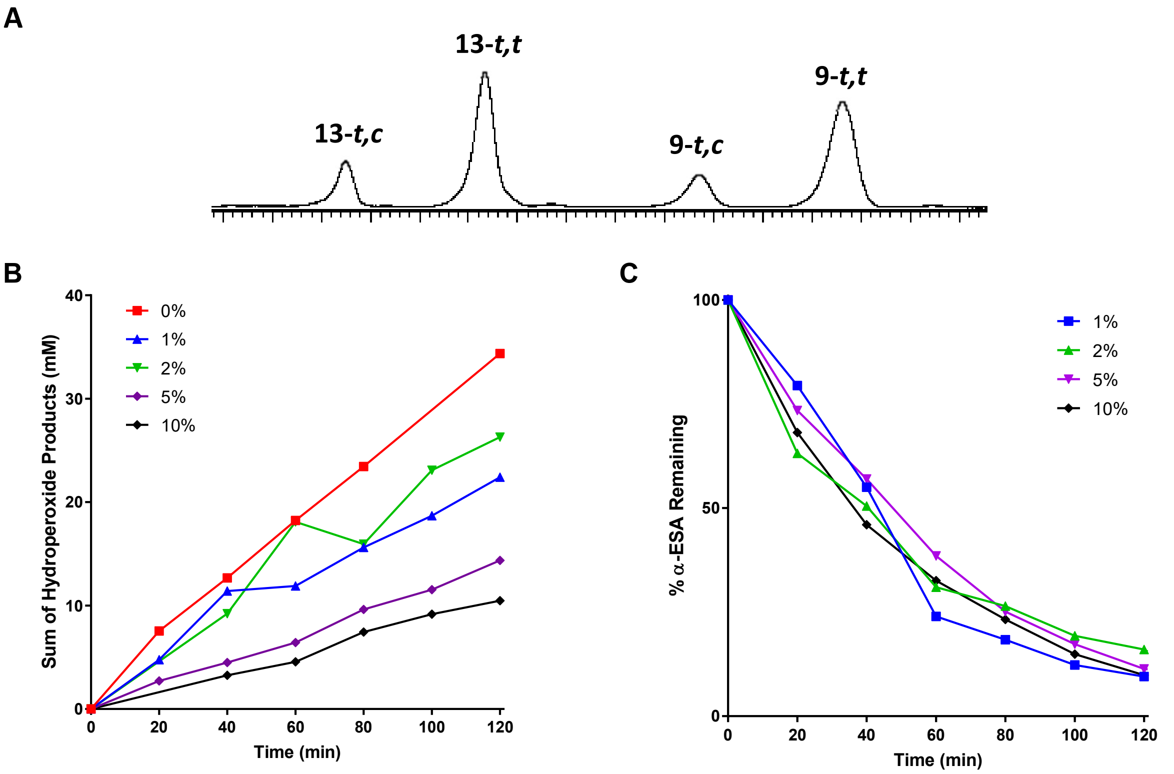

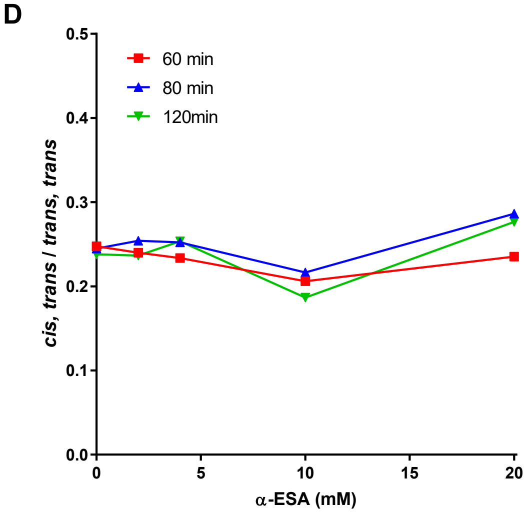

E

$$k_{p,ML} = 62\ \mathrm{M^{-1}s^{-1}}$$

$$k_{p,ML}\ [\mathrm{ML}] > k_{HAT,\alpha\text{-}ESA}\ [\alpha\text{-ESA}]$$
$$(62\ \mathrm{M^{-1}s^{-1}})(0.18\ \mathrm{M}) > k_{HAT,\alpha\text{-}ESA}\ (0.020\ \mathrm{M})$$

$$\therefore k_{HAT,\alpha\text{-}ESA} < 5.6 * 10^{2}\ \mathrm{M^{-1}s^{-1}}$$

Figure 3.5 Results of α-ESA/ML radical clocking experiment performed at 37 °C in PhCl. HPLC chromatogram of ML 13-*t,c*, 13-*t,t*, 9-*t,c*, and 9-*t,t* hydroperoxide products (**A**), sum of ML hydroperoxide products at increasing proportion of α-ESA (**B**), loss of α-ESA over the course of the radical clock (**C**), ratio of *cis,trans* to *trans,trans* products varying by α-ESA concentration (**D**), and upper bound of HAT propagation rate calculation resulting from experiment (**E**).

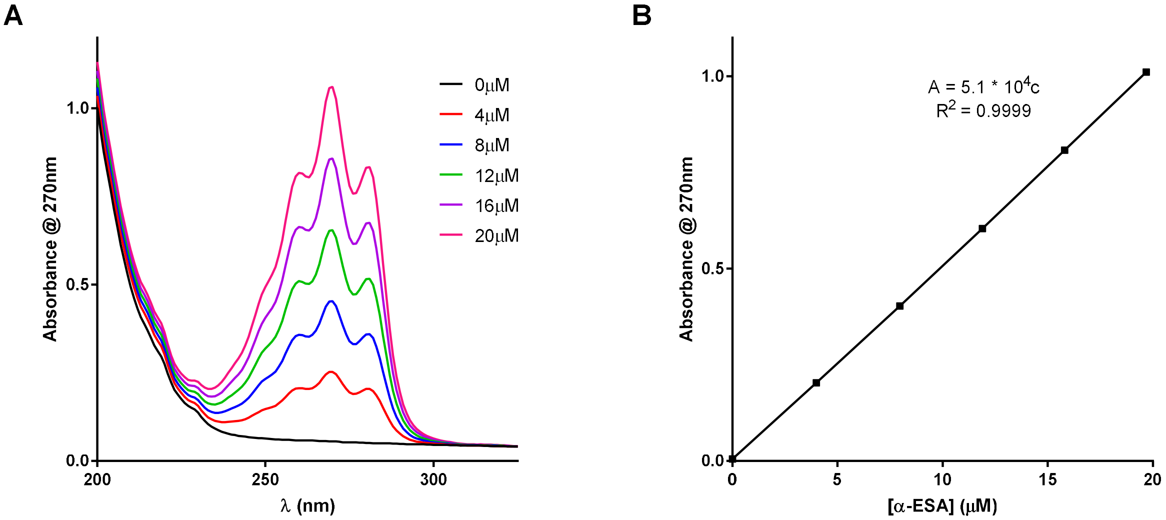

C

$A = \varepsilon bc$

$A = mc$; $m = \varepsilon b$

$\varepsilon = 5.1 * 10^4\ M^{-1}cm^{-1}$

A = absorbance at 270 nm

ε = extinction coefficient ($M^{-1}cm^{-1}$)

b = path length = 1 cm

c = concentration (M)

m = slope of **B** (M^{-1})

Figure 3.6 Absorbance of α-ESA measured at concentrations of 0, 4, 8, 12, 16, and 20 μM; samples scanned between 200 and 350 nm (**A**). Linear regression of α-ESA absorbance at 270 nm, $R^2 = 0.9999$ (**B**), and calculations to determine extinction coefficient at 37 °C in isooctane (**C**).

To correct this discrepancy, we increased [α-ESA] 100-fold to 2 mM to provide a longer chain length (projected from our v at 20 μM). Due to the high absorbance of α-ESA, this experiment could not be followed by continuous UV measurement and was instead completed in a RBF, with aliquots taken periodically, diluted 100-fold, and read via UV-Vis over a period of 3 hours (20 μM α-ESA has an absorbance of ~1 at 270 nm). Transforming the collected data allowed us to determine initial rate of autoxidation, with a projected linear regression of $R^2 = 0.78$ (**Figure 3.7C**). Calculating chain length, we were pleased to find a value of $v = 17$, in the range we had predicted (**Figure 3.7D**). Using the initial rate determined at [α-ESA] = 2.0 mM, and literature values of R_i ($1.3 * 10^{-9}\ Ms^{-1}$) and k_t for ML ($4.4 * 10^6\ M^{-1}s^{-1}$) ,[27] we were able to estimate a propagation rate constant for α-ESA of $k_p = 9.1 * 10^2\ M^{-1}s^{-1}$ at 37 °C, almost two fold greater than the upper bound determined for $k_{HAT,\alpha\text{-}ESA}$.

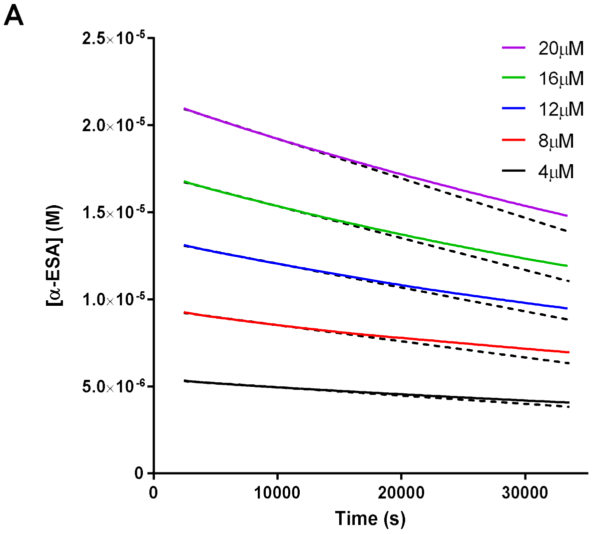

B

[α-ESA] (μM)	Initial Rate Equation	$v = \frac{R_p}{R_i}$
20.0	$y = -2.27 * 10^{-10} x + 2.15 * 10^{-5}$ $R^2 = 0.999$	0.174
16.0	$y = -1.83 * 10^{-10} x + 1.72 * 10^{-5}$ $R^2 = 0.999$	0.141
12.0	$y = -1.37 * 10^{-10} x + 1.34 * 10^{-5}$ $R^2 = 0.999$	0.105
8.0	$y = -9.3 * 10^{-11} x + 9.5 * 10^{-6}$ $R^2 = 0.998$	0.071
4.0	$y = -4.7 * 10^{-11} x + 5.4 * 10^{-6}$ $R^2 = 0.997$	0.036

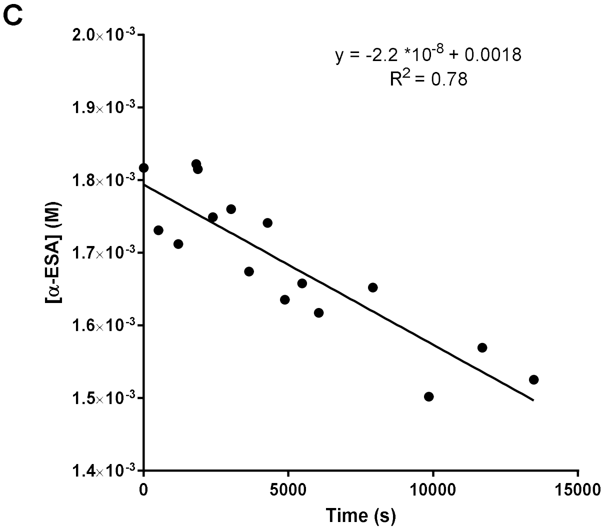

D

$$v = \frac{R_p}{R_i} = \frac{-2.2 * 10^{-8}}{1.3 * 10^{-9}} = 17$$

$$R_{i,AIBN} = 1.3 * 10^{-9}\ Ms^{-1}$$
$$k_t = 4.4 * 10^{6} M^{-1} s^{-1}$$

$$\frac{d[ROOH]}{dt} = 2.2 * 10^{-8}\ Ms^{-1}$$

$$\frac{d[ROOH]}{dt} = \frac{k_p [RH] \sqrt{R_i}}{\sqrt{2k_t}}$$
$$k_p = 9.1 * 10^{2}\ M^{-1} s^{-1}$$

Figure 3.7 Autoxidation of α-ESA at 4, 8, 12, 16, and 20 μM measured by loss of absorbance at 270 nm, converted to (M) using extinction coefficient (**A**), Equations for initial rates calculated by linear regression and chain length (**B**), linear regression of 2 mM α-ESA autoxidation calculated as above (**C**), and calculations to determine chain length and estimation of k_p from 2 mM α-ESA autoxidation at 37 °C in isooctane (**D**).

During our ML radical clocking experiments, the formation of oligomeric side products was anticipated as a result of α-ESA propagation by addition. Furthermore, dialkylperoxide products consisting α-ESA and the much more abundant ML were expected to be favoured over longer chains at low concentrations of α-ESA. By varying the ratio of α-ESA/ML present in the radical clocking experiment, we aimed to find a concentration of α-ESA at which potential dimeric addition products could be observed by HPLC. An example of an α-ESA/ML dialkylperoxide dimer is depicted in **Figure 3.8**.

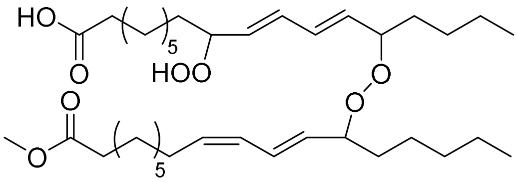

Figure 3.8 Dialkylperoxide dimer; an expected product during α-ESA/ML radical clocking experiments. The dimer consists of an α-ESA (top) and ML (bottom) chain.

Qualitatively screening observable products after experiment completion (120 minutes) indicated the formation of several unknown elutants by HPLC, marked with a red asterisk (*) (**Figure 3.9**). Two of these suspect peaks begin to appear when α-ESA constitutes 1% of the lipid pool, and a third appears after increasing α-ESA to 2%. At 2% α-ESA, additional products appear to have formed in low quantities, but remain discrete and (foreseeably) capable of being isolated for characterization. Although these unknown products would be expected in greater quantities with increased concentration of α-ESA, experiments including α-ESA concentrations greater than 2% have poor separation and distorted baselines, potentially due to a gradual elution of oligomers and lipid polymers of varying chain length.

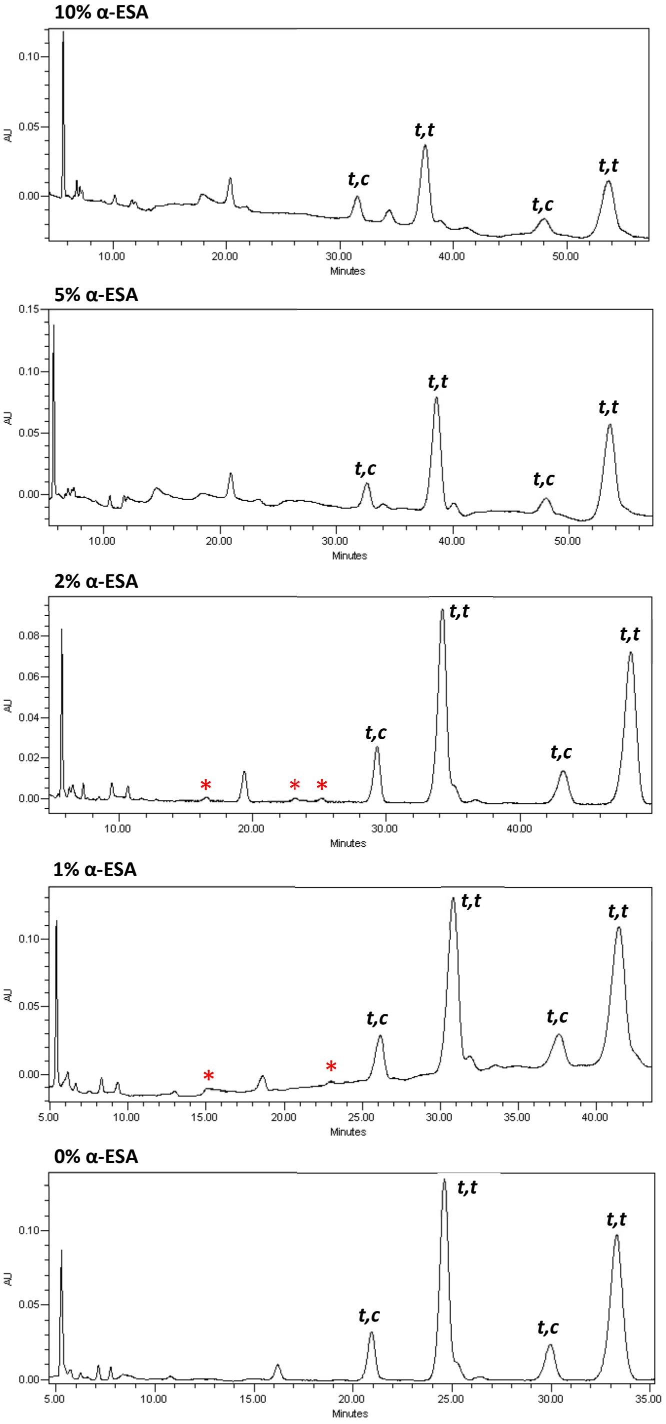

Figure 3.9 HPLC chromatograms for the α-ESA/ML radical clocking experiment described in **Figure 3.5** after 120 minutes with 10, 5, 2, 1, and 0% α-ESA (top to bottom). Peaks identified as potential oligomeric products are marked with a (*) and ML hydroperoxide product peaks are labelled accordingly.

3.2.2 Towards the Synthesis of 8,8,15,15-d_4-α-ESA

Efforts were made to obtain pure deuterated starting materials for the final reported synthesis of α-ESA (**Scheme 3.1**) with considerable success. These efforts can be divided into the fatty acid (ester) end (methyl 8,8-d_2-dec-9-ynoate) and terminal end (3,3-d_2-1-hexyne) of the d_4-α-ESA, which were six and four steps in length, respectively. Given the volatile nature of the terminal end and its precursors, and the similar transformations involved in obtaining each product, the fatty acid end was attempted first.

3.2.2.1 Preparation of methyl 8,8-d_2-dec-9-ynoate

Methyl oleate was prepared from the commercially available free acid via Fischer esterification, providing a cheap and reliable method of preparing material for the subsequent steps (**Scheme 3.3**). The reaction afforded the product in 92% yield with a high degree of purity following workup, without need for chromatographic purification.

Scheme 3.3 Fischer esterification of oleic acid.

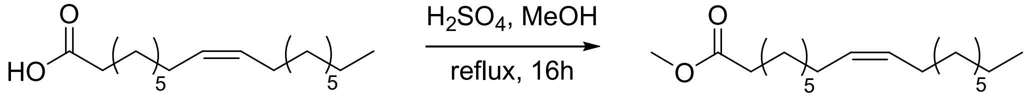

Methyl oleate was then cleaved by ozonolysis to yield methyl 9-oxononanoate and nonanal (**Scheme 3.4**). Methyl 9-oxononanoate was easily separable by TLC, however trituration of PPh_3O in cold hexanes was necessary prior to chromatography to obtain the product in pure form. Without trituration, tailing from the excess PPh_3 eluted with the product, and an additional chromatographic purification was required for isolation of the pure product. Following purification, methyl 9-oxononanoate was obtained in 84% yield.

Scheme 3.4 Ozonolysis of methyl oleate.

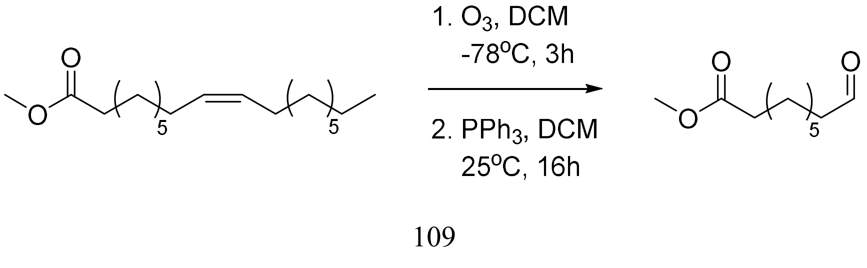

Deuteration of the methylene adjacent to the aldehyde was achieved by refluxing methyl 9-oxononanoate in D_2O in the presence of 4-dimethylaminopyridine (DMAP) enabling keto-enol tautomerization and proton exchange (**Scheme 3.5**). The initial exchanged afforded ~80% deuterium (D)-incorporation, and two subsequent exchanges (including workup) were required to achieve >95% D-incorporation. The resulting compound was sufficiently pure post-workup, affording an 87% yield, and chromatographic purification was not required.

Scheme 3.5 Deuteration of 9-oxononanoate by deuteron/proton exchange.

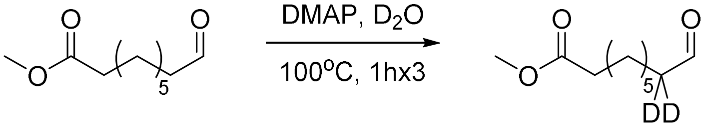

To prepare the respective terminal alkynes from the aldehyde precursors, the Ohira-Bestmann[28] modification of the Seyferth-Gilbert homologation was implemented. To do so required the two step preparation of dimethyl (1-diazo-2-oxopropyl)phosphonate (hereafter, the OB reagent). First, p-toluenesulfonyl azide (tosyl azide) was prepared from tosyl chloride in quantitative yield (**Scheme 3.6**). Post-workup, the azide was carefully dried *in vacuo* as verified by ^{1}H-NMR, given the moisture sensitive nature of the subsequent steps.

Scheme 3.6 Two step synthesis of Ohira-Bestmann reagent.

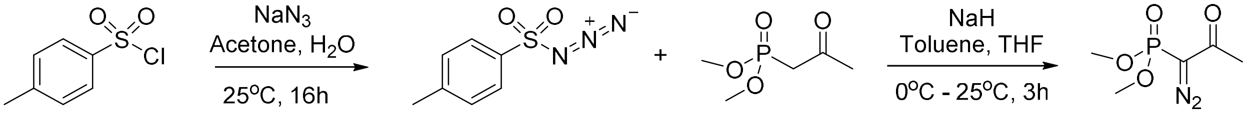

The OB reagent was then prepared using commercially available dimethyl 2-oxopropylphosphonate and tosyl azide (**Scheme 3.6**). Post-workup, the reaction mixture was filtered by silica plug, washing the silica 5-10 times with EtOAc and verifying complete filtration by TLC. The reaction afforded 91% yield, with minor residual toluene. Given the moisture sensitivity of the OB-reagent and the inert nature of the remaining solvent, the product was stored without further purification.

Methyl 8,8-d_2-dec-9-ynoate was then prepared by reaction of 8,8-d_2-9-oxononanoate with OB reagent under mildly basic conditions (**Scheme 3.7**). Initially, MeOH was used as the solvent, however proton-deuterium exchange occurred over the course of the reaction and a substantial amount (>30%) of incorporated deuterium was lost. Subsequent attempts in MeOD eliminated this loss. The use of MeOD also resulted in the deuteration of the terminal alkyne, assessed by peak suppression in the ^{1}H-NMR. Purification of crude product by silica chromatography yielded 42% of pure alkyne.

Scheme 3.7 One-pot conversion of aldehyde functionality to terminal alkyne using OB reagent to form methyl 8,8-d_2-dec-9-ynoate.

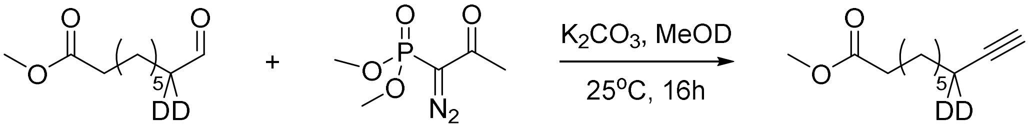

3.2.2.2 Preparation of 3,3-d_2-1-hexyne

Preparation of the terminal end of d_4-α-ESA proved more difficult than anticipated. Initial attempts to deuterate pentanal (**Scheme 3.8**) resulted in poor yields with numerous impurities visible by ^{1}H-NMR. Post-reaction, several aldehydic peaks were observed, most likely the result of self-condensation as reported previously in the literature.[20] Thus, care was taken to heat the reaction for no more than 60 min, at which point the mixture was cooled in an ice bath prior to workup, however several impurities still remained. Although pentanal was reagent grade (>98% purity), we distilled it prior to deuteration and were pleased to find this removed the remaining impurities observed in the crude product. Lastly, given the high volatility of short chain aldehydes, evaporating solvents under reduced pressure was kept to a minimum, compounds were not left *in vacuo*, and residual DCM was carried into subsequent exchanges with a yield of 67%.

Scheme 3.8 Deuteration of pentanal by deuteron/proton exchange.

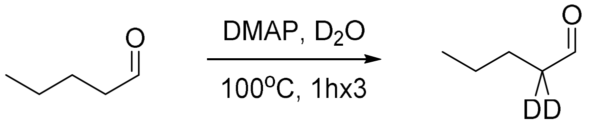

Conversion of deuterated pentanal to 3,3-d_2-1-hexyne by OB reagent (**Scheme 3.9**) progressed similarly to that in the synthesis of the fatty acid end. Deuterium incorporation from MeOD was observed at the terminal alkyne position, and complete loss of the aldehydic peak was observed by ^{1}H-NMR. Unfortunately, due to the highly volatile nature of the product (akin to hexane), isolation and characterization of the product was problematic. Once the reaction was worked up, separation from most traditional organic phase solvents (Et_2O, EtOAc, DCM, etc.) was extremely difficult. In addition, given the limited functionality of 3,3-d_2-1-hexyne, NMR spectral peaks were difficult to distinguish from residual solvent, especially considering the deuterium-suppressed alkyne proton peak. We theorized that extracting with pentane (lit b.p. = 36 °C) would offer a sufficient difference in boiling point to distill solvent from the crude product (hexyne b.p. = 71 °C). Although the distillation was successful, insufficient pentanal could be distilled to clarify the spectra. Difficulties aside, a suppressed C≡C-H peak can be seen at the correct chemical shift (1.9 ppm), complete loss of CH=O is observed, and no unexpected downfield peaks are present. Given the previous success using the OB reagent during long chain synthesis, we can predict the reaction was successful, but further characterization is required.

Scheme 3.9 One-pot conversion of aldehyde functionality to terminal alkyne using OB reagent to form 3,3-d_2-1-hexyne.

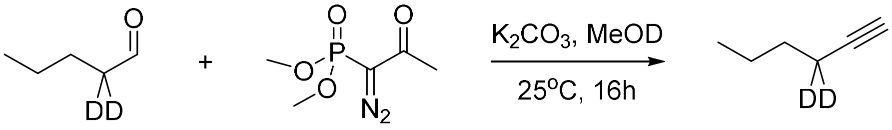

3.3 Discussion

α-ESA is a naturally produced lipid characterized by a highly oxidizable conjugated trienic unit and a ferroptosis-initiating potential unique amongst PUFAs. Even so, α-ESA remains considerably understudied in contrast to homoconjugated PUFAs, whose oxidation rates and mechanisms of propagation have been explored at great length.[1,6,11,23] One of the major challenges of studying α-ESA, which may also explain this discrepancy, is the difficulty associated with its correct isolation and storage. Tung oil is a common wood finishing agent, and as the primary ingredient, α-ESA is highly oxidizable when exposed to air. In early attempts at isolating pure crystals, we found storing sealed α-ESA at -20 ^{o}C resulted in our fine white crystals transforming into a honey-like substance. Loss of α-ESA was confirmed by ^{1}H-NMR (loss of triene functionality) and the resulting product was quite difficult to dissolve. These observations provided an early indication of autoxidation by polymerization (i.e. addition) occurring rapidly upon exposure to even minor quantities of air. In order to circumvent this loss, we found it necessary to dry the crystals under a stream of N_2 for one hour followed by quick transfer to a vial for *in vacuo* drying, after which the vial must be backfilled with N_2 before storage. By ensuring correct N_2 backfilling prior to storage, samples could be opened, used, and re-stored over several months without loss of α-ESA.

Through preliminary kinetic observations, we have begun to discern the mechanism by which α-ESA undergoes autoxidation. During ML radical clocking, hydroperoxide product ratios are maintained as α-ESA concentration and time are varied, which suggests that α-ESA is not significantly contributing to HAT at any point during the autoxidation, favouring addition as the primary method of propagation. Unfortunately our bound calculation ($k_{HAT,\alpha\text{-}ESA} < 5.6 * 10^{2}$ M^{-1}s^{-1} at 37 ^{o}C) is limited by the concentration of α-ESA, which remains dominated by ML as the reference substrate. Although increasing α-ESA concentration past 10% would continue to narrow the upper bound, this experimentally becomes unrealistic as an increasing the concentration of α-ESA is correlated to a substantial decrease in ML hydroperoxide products. Although the $k_{HAT,\alpha\text{-}ESA}$ upper bound fails to narrow down a precise value for the HAT rate constant, it can be used as a point of comparison for our experimentation involving determination of k_p.

Since α-ESA only has one functional group capable of autoxidation, there is no concern of intramolecular competition when measuring loss of absorbance and thus, we can make confident conclusions regarding the trienic unit and its propagation mechanisms. Unfortunately, a degree of error was introduced when measuring α-ESA at a concentration (2.0 mM) capable of generating a valid chain length. This error is attributable to experimental design, as 100-fold dilutions of 25 μL are difficult to consistently measure by hand, and absorbance experiments are best completed with a vial remaining zeroed and fixed within the spectrophotometer. Error aside, the initial data collected from the autoxidation remains visually acceptable, with no significant outliers or non-linear trends (**Figure 3.7C**). Although by itself, the 2 mM autoxidation data would be flimsy evidence for determination of a rate constant, the accuracy and precision of the corroborative results collected at 4 to 20 μM provides a strong support that this data is reliable. Thus, we report an estimated propagation rate constant of $9.1 * 10^2$ $M^{-1}s^{-1}$ at 37 °C (**Figure 3.10**). To further validate this claim, the large scale autoxidation should be reported for at least four additional concentrations over an extended period of time, in triplicate, to determine d[ROOH]/dt by linear regression (as was intended at the lower concentration range implemented) and recalculate k_p. One caveat to these calculations is the use of the k_t for ML in order to calculate k_p. Although permissible for the preliminary calculations performed herein, kinetic studies to determine a termination constant for α-ESA must be performed in order to validate a true k_p.

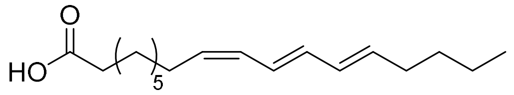

$k_p = 9.1 * 10^2\ M^{-1}s^{-1}$; $k_{HAT} < 5.6 * 10^2\ M^{-1}s^{-1}$

$\therefore k_{add} > 3.5 * 10^2\ M^{-1}s^{-1}$

Figure 3.10 Estimated rate constants and bound for propagation, HAT, and addition of α-ESA at 37 °C.

Given the large difference in magnitude between our upper bound for the HAT rate constant and the estimated chain propagation rate constant, we can infer that addition is the predominant path by which α-ESA autoxidizes. Based on our determined values for k_p and k_{HAT}, we calculate that α-ESA propagates by addition at a rate of at least $3.5 * 10^2$ $M^{-1}s^{-1}$. Admittedly, this value is less than that of the HAT upper bound, but as previously mentioned, HAT is likely much lower than this value, meaning k_{add} would proportionally be that much greater. Although limited by our experimental methods, these observations provide evidence that addition plays a substantial role in propagation of α-ESA autoxidation, the extent to which remains to be determined (**Figure 3.11**).

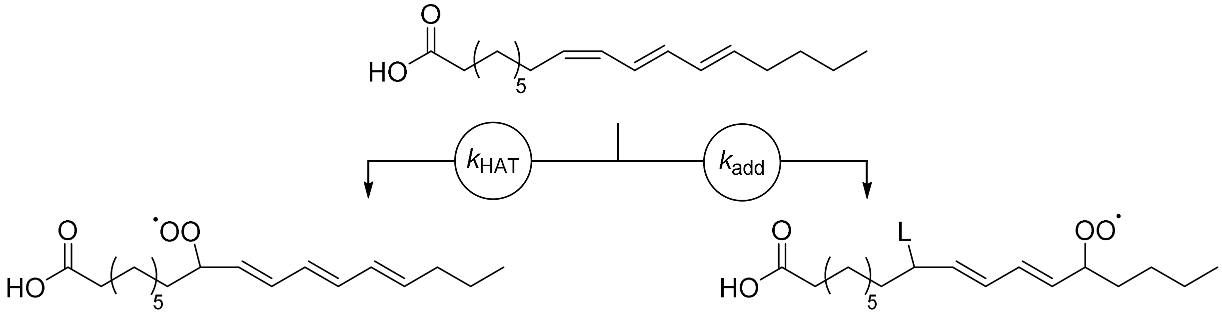

Figure 3.11 α-ESA can propagate by either addition or HAT to generate peroxyl products, the distribution of which still remains in question.

Soon following our preliminary findings on α-ESA, we were pleased to learn of a newly accepted methodology for ML radical clocks from Do, et al. (2020), specifically designed to simultaneously measure both k_{HAT} and k_{add}.[7] The new method involves quenching a portion of the reaction mixture with the strong reducing agent $LiAlH_4$, reducing both hydroperoxides HAT products as well as dialkylperoxides stemming from addition. This portion is analyzed alongside an unreduced portion and the total peroxyl products (via strong reductant) are contrasted to newly characterized HAT products (prior to reduction) to determine a more robust k_p, as well as k_{HAT}, and k_{add}.[7] Among the natural products screened was *trans*-stereoisomer β-ESA (here referred to as conjugated linolenic acid), reported to possess $k_{HAT} = 363$ +/- 121 $M^{-1}s^{-1}$ and k_{add} = 872 +/- 121 $M^{-1}s^{-1}$.[7] Given the clear structural similarities, we would anticipate similar values for α-ESA, which fall well within our current predicted range. By implementing this new methodology for α-ESA, we would easily be able to confirm the all-but-measured rate constants for addition and HAT.

Our efforts to synthesize an α-ESA analog deuterated at the allylic C8 and C15 positions have progressed well, overcoming several difficulties, with only a few (previously reported[18]) steps remaining. We are pleased to report a successfully synthesized and purified long chain intermediate, methyl 8,8-d_2-dec-9-ynoate. The intermediate was prepared in four steps with a total yield of 28.3% from the cheap and commercially available oleic acid. Up to this point, the chemistry has remained mild, requiring relatively simple conditions and purification techniques. The Ohira-Bestmann reagent, prepared in two steps, proved quite effective at limiting the number of steps required after deuterium incorporation. As such, the incorporated deuterium atoms have limited opportunity for exchange over additional steps or purifications, and are well protected after the alkyne group is installed. Although minor deuterium is lost during the final step, this can be attributed to the propensity for methanol to take on atmospheric water, as the reaction was performed without a glovebox. This would provide the opportunity for some exchange to occur between H_2O and substrate as the reaction progressed.

Completion of the short chain synthesis to yield the intermediate 3,3-d_2-1-hexyne proved more difficult than the former. Although optimistic about our results, we were unfortunately unable to definitively identify the final product from residual solvent. The product is quite difficult to isolate given its high vapour pressure and will evaporate in a matter of seconds *in vacuo* (as the structure might suggest). Examining the crude product by ^{1}H-NMR indicates the presence of predominantly pentane (from extraction) and toluene (residual from OB reagent) distorting product identification. However, isolation from both these solvents could be achieved provided a more thorough methodology. Toluene often remains present during OB reagent preparation due to the highly reactive nature of the product, as evaporating solvent over long periods at higher temperatures can result in degradation. However, ensuring toluene removal through longer evaporation, although not ideal for OB reagent yield, would reduce solvent presence in the subsequent reaction. In addition, more extensive distillation of pentane from crude product would allow more time for product evaporation/loss but would also increase product purity. In sum, extended solvent removal pre- and post-reaction may negatively impact product yield, but may be inevitable for improved identification. The other major difficulty in identifying 3,3-d_2-1-hexyne is that the one truly distinct C≡C-H proton peak, at 1.9 ppm, is largely suppressed by deuterium incorporation making the peak even less visible amongst residual solvent. Post-reaction, a strong base such as KO^{t}Bu could be used to exchange protons between the terminal alkyne and H_2O.[29] Although such a method would not be ideal for the bulk product, an aliquot could be taken for test to identify if the terminal alkyne peak returns to its expected size. Were the peak to return, sufficient evidence would exist to attempt the next synthetic steps, forming a larger, more stable intermediate capable of complete characterization and effectively verifying the success of the previous step. The subsequent hydroalumination and diene synthesis would be performed in organic solvent, and neither pentane nor toluene would provide undesirable reactivity or conditions for the reaction.

3.3 Conclusions & Future Work

α-ESA is a conjugated lipid with chemical and biological properties which remain largely unknown, but indicate great potential for future pharmacological use. Although preliminary studies identify α-ESA as anti-tumorigenic and a ferroptosis-inducing agent, understanding its mechanism of action is critical to be able to meaningfully build upon these observations. We are pleased to report preliminary results towards establishing an autoxidation mechanism and associated rate constants at physiological conditions, which suggest addition as the primary mechanism of action. We have observed an estimated propagation rate constant of $9.1 * 10^2$ $M^{-1}s^{-1}$ with an upper bound on α-ESA HAT ($k_{HAT} < 5.6 * 10^2$ $M^{-1}s^{-1}$). These values do not suggest a significant rate of HAT, but instead provide a clear evidence that a substantial portion of propagation may be attributed to addition, the extent of which is still unknown. Radical clocking with ML further supports this conclusion, as addition of increasing α-ESA concentrations does not affect product distribution, suggesting ML ($k_{HAT} = 62$ $M^{-1}s^{-1}$) dominates α-ESA in rate of HAT. Moving forward, the newly reported ML radical clocking approach should be implemented as a means to determine k_{HAT} and k_{add} in a more direct manner, verifying the trends reported in similar trienes.[7]

Our efforts to clarify the mechanism would be further bolstered by repeating the outlined experimental methods with a deuterated 8,8,15,15-d_4-α-ESA analog. Were HAT to play a significant role in propagation a 1° KIE would be observed, as deuterium would slow the rate of HAT from allylic sites on d_4-α-ESA. Of course, synthesis of the deuterated analog must be completed before these kinetic experiments can be carried out. Following confirmation of the presence of 3,3-d_2-hexyne, the previously reported three step synthesis of α-ESA[18] should be carried out, the first step of which is alkyne hydroalumination and subsequent diene synthesis with *trans*-1,2-dichloroethylene, detailed procedures of which are reported in the literature.[30,31]

In addition to these efforts, further analysis of the α-ESA/ML clocking experiment products should be completed to identify and isolate oligomeric products resulting from α-ESA addition (**Figure 3.12)**. The magnitude of oligomerization would be controlled by substrate availability, and at lower concentrations of α-ESA, a greater presence of α-ESA/ML dialkylperoxide dimers would be expected (as opposed to longer chains). The clean baseline present at 2% α-ESA (**Figure 3.9**) indicates that isolation and characterization of dialkylperoxide products should be first attempted under these conditions. Not only would isolation of these products support our previous mechanistic work, but also provide a substrate to study the cytotoxicity of α-ESA autoxidative products. α-ESA appears to initiate lipid peroxidation and induce ferroptosis in mammalian cells; however, these effects may be attributable to the dialkylperoxide products resulting from its presence. Although hydroperoxides would be reduced to their respective alcohols prior to isolation, the dialkylperoxide functionalities would remain intact and could be studied. After dialkylperoxides are characterized, a large-scale autoxidation of the same α-ESA/ML ratio could be performed, followed by isolation of dialkylperoxide products via preparative chromatography. The ability of these dialkylperoxides to initiate lipid peroxidation and evade reduction by GPX4 could then be investigated first *vide infra*. If activity is established, further experiments could be completed in liposomes and cells, similar to the experimental procedures outlined in Chapter 2.

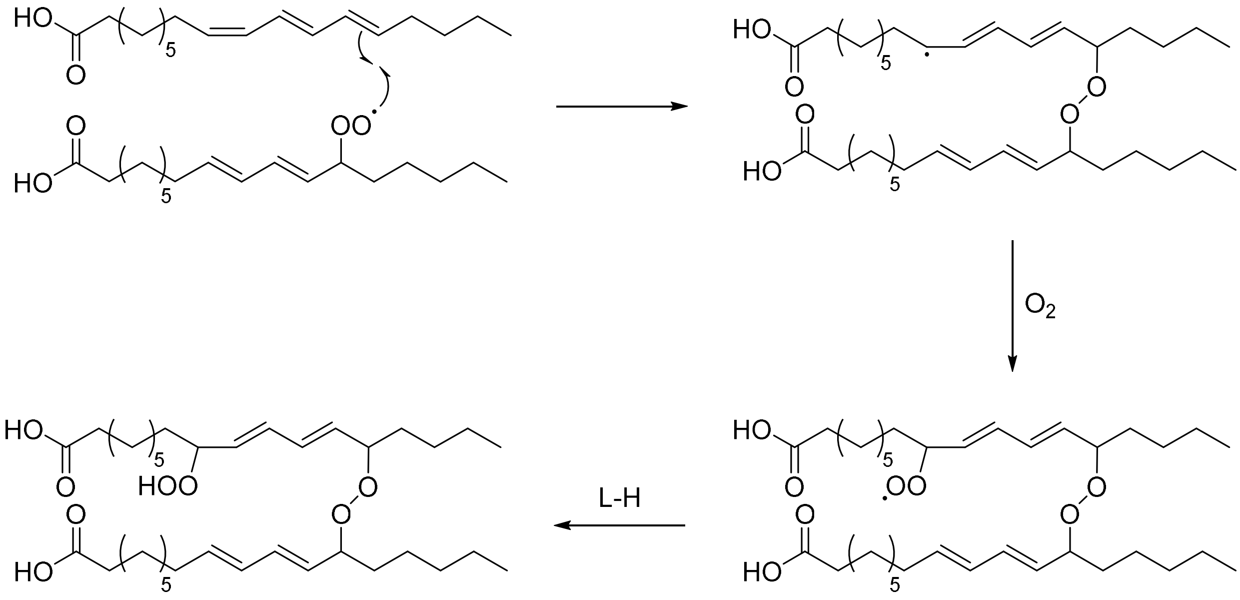

Figure 3.12 Mechanism for the formation of proposed peroxidic heterodimer between α-ESA and linoleic acid.

3.5 Experimental

Solvents, chemicals, and reagents were purchased from commercial sources and used as received. Any α-ESA used experimentally was isolated from Tung oil as described below, purity verified by ^{1}H-NMR. ^{1}H and ^{13}C NMR were recorded on Bruker AVANCE^{TM} II 300 and 400 MHz instruments.

Purification of α-ESA: Tung oil (5.0 g) was combined with KOH (1.5 g), H_2O (1.25 mL), and ethanol (12.5 mL) were combined and stirred under refluxing conditions overnight. HCl (2N, 18 mL) and ethanol (25 mL) were then combined with mixture in separatory funnel, and aqueous layer was drained off. Lipid products were then decanted into an Erlenmeyer flask and dissolved by heating into ethanol (25 mL). After returning to room temperature flask was sealed and recrystallized overnight at -20 °C. The supernatant, now a dark yellow, was drained off of crystals and replaced v/v with fresh ethanol, heated, and recrystallized as before overnight. This process was repeated a second time (the supernatant now colourless), after which the room temperature solution was recrystallized at -20 °C in a glass tube with a frit fitting at the base (positive $N_{2(g)}$ pressure was applied to prevent EtOH drainage during recrystallization) using an immersion cooler (FTS Systems, FC100A01). Upon crystal formation, $N_{2(g)}$ pressure was used to drain ethanol through the frit and dried under stream of $N_{2(g)}$ for one hour. Fine, white crystals of α-ESA (verified by ^{1}H-NMR) were quickly removed, dried on hivac for an additional 30 min, backfilled with $N_{2(g)}$, and stored at -2 0°C.

α-ESA and methyl linoleate radical clock experiment: 1.0 M MeLin and 100 mM α-ESA stock solutions were added in 100:0, 99:1, 98:2, 95:5, and 90:10 (v/v) ratios to for a total of 0.2 M of lipid in 1.5 mL PhCl (including initiator volume). 150 µL of 100 mM MeOAMVN stock solution, dissolved in PhCl, was then added and solution was stirred at 37 °C for three hours. Every 20 minutes, 100 µL aliquots were taken and quenched with 900 µL of hexane solution containing 55.56 mM PPh_3 and BHT as well as 11.11 mM BnOH as a reference compound for HPLC analysis. The experiment was performed using HPLC grade solvents.

HPLC Analysis: Samples were injected in 10 µL aliquots and separated through a Waters^{TM} Sunfire silica column (100Å, 5 µm, 4.6 mm x 250mm) at 0.5% IPA in hexanes, 1.0 mL/min. Elutants were analyzed via PDA detection at 235 nm, except α-ESA which was measured at 270 nm. All samples were analyzed using a HPLC Waters 2996 separations module. Results were adjusted for comparison using the 10 mM BnOH reference peak (~ 6 min elution).

Measuring α-ESA absorbance by spectrophotometry: 2.490 mL of isooctane was added to a cuvette, placed in a Cary 100 Bio UV-Vis spectrophotometer (Agilent Technologies, Inc.), and warmed to 37 °C for fifteen minutes. 10 µL of 1 mM α-ESA stock, dissolved in isooctane, was then added and absorbance was measured from 200 to 350 nm. This process was repeated until a maximum of 50 µL (of 1 mM α-ESA) was added, in increments of 10 µL. The experiment was performed in triplicate using HPLC grade solvents.

Tracking loss of α-ESA trienic unit: To a cuvette, a volume of isooctane (necessary to achieve 2.5 mL total volume) was added, placed in a Cary 100 Bio UV-Vis spectrophotometer (Agilent Technologies, Inc.), and warmed to 37 °C for fifteen minutes. 10-50 µL of 1 mM α-ESA stock (dissolved in isooctane) and 50 µL of 6 mM AIBN stock (dissolved in isooctane:dioxane 1:1 (v/v)) were then added, in that order. Absorbance was then measured from 200 to 350nm for 9 hours. The experiment was performed using HPLC grade solvents.

Tracking loss of α-ESA trienic unit (large scale): To a RBF, 9.60 mL of isooctane was added and stirred at 37 °C. 200 µL of 100 mM α-ESA stock (in isooctane) and 200 µL of 300 mM AIBN stock (dissolved in isooctane:dioxane 1:1 (v/v)) were then added, to yield initial concentrations of 2 mM and 6 mM, respectively. 25µL aliquots were then removed and diluted in a cuvette with isooctane 100-fold (to 2.5 mL) before reading absorbance between 200 and 350 nm by UV-Vis. Aliquots were taken every 10 minutes for the first two hours and every 30 minutes thereafter. The experiment was performed using HPLC grade solvents.

Synthesis of methyl oleate: Oleic acid (20.0 g, 70.8 mmol) was dissolved in methanol (80 mL) in a RBF and set to stir. To the solution, concentrated H_2SO_4 (1.0 mL, 18.4 mmol) was added dropwise after which the solution was heated to reflux and stirred overnight. Upon completion of the reaction, as indicated by TLC, Na_2CO_3 was added until the acid was neutralized. The organic layer was extracted twice using Et_2O and an excess of H_2O, dried over $MgSO_4$, and concentrated *in vacuo*. Clear-yellow oil; 92% yield. ^{1}H-NMR (400 MHz, $CDCl_3$): δ 5.42 – 5.23 (m, 2H), 3.66 (s, 3H), 2.30 (t, *J* = 7.6 Hz, 2H), 2.01 (m, 4H), 1.62 (p, *J* = 7.3 Hz, 2H), 1.38 – 1.21 (m, 20H), 0.88 (t, *J* = 7.1 Hz, 3H). ^{13}C-NMR (101 MHz, $CDCl_3$): δ 174.5, 130.2, 130.0, 51.6, 34.3, 32.1, 30.0, 29.9, 29.7, 29.5, 29.4, 29.3, 29.3, 27.4, 27.4, 25.1, 22.9, 14.3.

Synthesis of methyl 9-oxonanononate: Methyl oleate (20.0 g, 67.4 mmol) was dissolved in DCM, added to a RBF, set to stir, and cooled to -78 °C. O_3 was then bubbled through using an OL80W Ozone Generator (OzoneLab^{TM} Instruments) until the solution turned a light blue. PPh_3 (36.5 g, 139.2 mmol) dissolved in DCM was added dropwise, and reaction was warmed to room temperature, stirring overnight. Solution was then concentrated *in vacuo* and the bulk PPh_3 was removed by trituration with cold hexanes. Crude product was purified by silica gel flash chromatography (10% EtOAc in hexanes to remove remaining PPh_3 and then 25% EtOAc).[32] Colourless oil; 84% yield. ^{1}H-NMR (400 MHz, $CDCl_3$): δ 9.76 (t, *J* = 1.8 Hz, 1H), 3.66 (s, 3H), 2.42 (td, *J* = 7.3, 1.8 Hz, 2H), 2.30 (t, *J* = 7.5 Hz, 2H), 1.68 – 1.55 (m, 4H), 1.38 – 1.22 (m, 6H). ^{13}C-NMR (101 MHz, $CDCl_3$): δ 203.0, 174.4, 51.7, 44.0, 34.2, 29.2, 29.1, 29.1, 25.0, 22.2. HRMS (EI): calculated for $C_9H_{17}O_3^-$ (loss of $^+$H from $C_9H_{18}O_3$) 185.1172, found 185.1149.

Synthesis of 8,8-d_2-methyl 9-oxononanoate: To a RBF, methyl-9-oxononanoate (14.0 g, 75.2 mmol), DMAP (0.92 g, 7.53 mmol) and 15 mL of D_2O were stirred at reflux for one hour. The flask was briefly cooled in an ice bath and extracted using DCM. Organic layer was then washed using 1N HCl, $NaHCO_{3(sat.)}$, and brine, dried over $MgSO_4$, and concentrated *in vacuo*. This procedure was repeated twice more until >95% deuterium incorporation was observed at the aldehyde α-carbon, verified by ^{1}H-NMR.[20] Clear-yellow oil; 87% yield. ^{1}H-NMR (400 MHz, $CDCl_3$): δ 9.76 (s, 1H), 3.66 (s, 3H), 2.30 (t, *J* = 7.5 Hz, 2H), 1.68 – 1.53 (m, 4H), 1.38 – 1.26 (m, 6H). ^{13}C-NMR (101 MHz, $CDCl_3$): δ 203.2, 174.4, 51.7, 34.2, 29.2, 29.1, 25.0, 22.0. HRMS (EI): calculated for $C_9H_{13}D_2O_3^-$ (loss of $^+CH_3$ from $C_{10}H_{16}D_2O_3$) 173.1152, found 173.1164.

Synthesis of tosyl azide: In a RBF, NaN_3 (5.0g, 76.9 mmol) was dissolved in a solution of 80 mL H_2O and 20 mL acetone. TsCl (13.3g, 69.7 mmol) was dissolved in 28 mL acetone, added dropwise by syringe, and rinsed using an additional 4 mL acetone, after which the reaction was stirred at room temperature overnight. Upon completion of the reaction, as indicated by TLC, acetone was removed *in vacuo* and the remaining mixture was extracted using DCM. The organic layer was washed three times with H_2O, dried over $MgSO_4$, and concentrated *in vacuo*.[33] Colourless oil; 98% yield. ^{1}H-NMR (400 MHz, $CDCl_3$): δ 7.83 (td, 2H), 7.39 (d, *J* = 8.0 Hz, 2H), 2.47 (s, 3H). ^{13}C-NMR (101 MHz, $CDCl_3$): δ 146.4, 135.7, 130.5, 127.7, 22.0.

Synthesis of dimethyl (1-diazo-2-oxopropyl)phosphonate: In a RBF, sodium hydride in 60% mineral oil (1.7g, 69.2 mmol) was dissolved portionwise in a stirring solution of 250 mL toluene and 50 mL THF under N_2 atm at 0 °C. Dimethyl 2-oxopropylphosphonate (9.6 mL, 69.5 mmol) was then added dropwise and mixture was stirred for 90 min. Tosyl azide (12.4g, 62.9 mmol), dissolved in 16 mL toluene, was added dropwise and reaction was warmed to room temperature and stirred for an additional one hour. Upon consumption of TsN_3, as indicated by TLC, mixture was filtered through silica plug and residue was washed with EtOAc until product was not visible in filtered solvent (by TLC). Resulting filtrate was concentrated *in vacuo*.[34] Yellow oil; 91% yield. ^{1}H-NMR (400 MHz, $CDCl_3$): δ 3.87 (s, 3H), 3.84 (s, 3H), 2.27 (s, 3H).

Synthesis of 8,8-d_2-methyl dec-9-ynoate: In a RBF, K_2CO_3 (4.4 g, 31.9 mmol) was added to 20 mL MeOD and set to stir. Dimethyl (1-diazo-2-oxopropyl)phosphonate (3.7 g, 19.1 mmol) and 8,8-d_2-methyl 9-oxononanoate (3.0 g, 15.9 mmol) were the added slowly, in succession, and stirred at room temperature overnight. Upon consumption of nonanoate, as indicated by TLC, reaction was diluted with 30 mL diethyl ether, and washed with 30 mL $NaHCO_{3(sat.)}$:$H_2O_{(d)}$ 1:1 (v/v). Aqueous layer was then extracted with diethyl ether twice more, and organic layers were combined, dried using $MgSO_4$, concentrated *in vacuo*, and purified by silica gel flash chromatography (10% EtOAc in hexanes).[28] Clear-yellow oil; 42% yield. ^{1}H-NMR (400 MHz, $CDCl_3$): δ 3.66 (s, 3H), 2.30 (t, J = 7.5 Hz, 2H), 1.67 – 1.55 (m, 2H), 1.54 – 1.46 (m, 2H), 1.44 – 1.21 (m, 6H). ^{13}C-NMR (101 MHz, $CDCl_3$): δ 174.5, 51.7, 34.3, 31.8, 29.2, 29.0, 28.7, 28.4, 25.1, 22.9, 14.3. HRMS (EI): calculated for $C_{10}H_{13}D_2O^+$ (loss of $^-OCH_3$ from $C_{11}H_{16}D_2O_2$) 153.1243, found 153.1226.

Synthesis of 2,2-d_2-pentanal: To a RBF, distilled pentanal (8.0 mL, 75.2 mmol), DMAP (0.92 g, 7.53 mmol) and 8 mL of D_2O were stirred at reflux for one hour. The flask was briefly cooled in an ice bath and extracted using DCM. Organic layer was then washed using 1N HCl, $NaHCO_{3(sat.)}$, and brine, dried over $MgSO_4$, and concentrated *in vacuo*. This procedure was repeated twice more until >95% deuterium incorporation was observed at the α-carbon, verified by ^{1}H-NMR.[20] Colourless oil; 67% yield. ^{1}H-NMR (300 MHz, $CDCl_3$): δ 9.77 (s, 1H), 1.66 – 1.54 (m, 2H), 1.43 – 1.29 (m, 2H), 0.93 (t, J = 7.3 Hz, 3H). ^{13}C-NMR (101 MHz, $CDCl_3$): δ 203.3, 24.2, 22.4, 14.0.

Synthesis of 3,3-d_2-hex-1-yne: In a RBF, K_2CO_3 (6.6 g, 47.8 mmol) was added to 25 mL MeOD and set to stir. Dimethyl (1-diazo-2-oxopropyl)phosphonate (5.5 g, 28.7 mmol) and 2,2-*d_2-pentanal* (2.1 g, 23.9 mmol) were the added slowly, in succession, and stirred at room temperature overnight. Upon consumption of pentanal, as indicated by ^{1}H-NMR, reaction was diluted with 15 mL pentane, washed with 20 mL $NaHCO_{3(sat.)}$:$H_2O_{(d)}$ 1:1 (v/v), and dried using $MgSO_4$. Pentane was distilled from organic layer between 45 and 60 ºC. Dark-yellow oil (crude);

3.6 References

1. Yin, H., Xu, L. & Porter, N. A. Free radical lipid peroxidation: Mechanisms and analysis. Chem. Rev. 111, 5944–5972 (2011).
2. Conrad, M. & Pratt, D. A. The chemical basis of ferroptosis. Nat. Chem. Biol. 15, 1137–1147 (2019).
3. Montine, T. J. et al. F 2 -Isoprostanes in Alzheimer and Other Neurodegenerative Diseases. Antioxid. Redox Signal. 7, 269–275 (2005).
4. Kuhn, H., Banthiya, S. & Van Leyen, K. Mammalian lipoxygenases and their biological relevance. Biochim. Biophys. Acta - Mol. Cell Biol. Lipids 1851, 308–330 (2015).
5. Yang, W. S. et al. Peroxidation of polyunsaturated fatty acids by lipoxygenases drives ferroptosis. Proc. Natl. Acad. Sci. U. S. A. 113, E4966–E4975 (2016).
6. Xu, L., Davis, T. A. & Porter, N. A. Rate constants for peroxidation of polyunsaturated fatty acids and sterols in solution and in liposomes. J. Am. Chem. Soc. 131, 13037–13044 (2009).
7. Do, Q. et al. Development and Application of a Peroxyl Radical Clock for Measuring Both Hydrogen-Atom Transfer and Peroxyl- The Development and Application of a Peroxyl Radical Clock for Measuring Both Hydrogen-Atom Transfer and Peroxyl-Radical Addition Rate Constants. J. Org. Chem. Submitted, (2020).
8. Beatty, A. et al. Conjugated linolenic fatty acids trigger ferroptosis in triple-negative breast cancer. bioRxiv (2019). doi:10.1101/556084
9. Tsuzuki, T., Tokuyama, Y., Igarashi, M. & Miyazawa, T. Tumor growth suppression by α-eleostearic acid, a linolenic acid isomer with a conjugated triene system, via lipid peroxidation. Carcinogenesis 25, 1417–1425 (2004).
10. Pratt, D. A., Mills, J. H. & Porter, N. A. Theoretical calculations of carbon-oxygen bond dissociation enthalpies of peroxyl radicals formed in the autoxidation of lipids. J. Am. Chem. Soc. 125, 5801–5810 (2003).
11. Miyashita, K., Hara, N. & Fujimoto, K. Dimers Formed in Oxygenated Methyl Linoleate Hydroperoxides. 20, 578–587 (1985).
12. Dhar Dubey, K. K., Sharma, G. & Kumar, A. Conjugated Linolenic Acids: Implication in Cancer. J. Agric. Food Chem. 67, 6091–6101 (2019).
13. Tsuzuki, T. et al. Oxidation rate of conjugated linoleic acid and conjugated linolenic acid is slowed by triacylglycerol esterification and α-tocopherol. Lipids 39, 475–480 (2004).
14. Brauer, R. W. & Steadman, L. T. The Autoxidation of β-Eleostearic Acid. The Application of the Spectrophotometer to the Study of the Course and the Kinetics of the Reaction. J. Am. Chem. Soc. 66, 563–569 (1944).

15. Brigelius-Flohé, R. & Maiorino, M. Glutathione peroxidases. Biochim. Biophys. Acta - Gen. Subj. 1830, 3289–3303 (2013).

16. Lamberson, C. R. et al. Unusual Kinetic Isotope Effects of Deuterium Reinforced Polyunsaturated Fatty Acids in Tocopherol-Mediated Free Radical Chain Oxidations. J. Am. Chem. Soc. 136, 838–841 (2014).

17. Shah, R., Shchepinov, M. S. & Pratt, D. A. Resolving the Role of Lipoxygenases in the Initiation and Execution of Ferroptosis. ACS Cent. Sci. 4, 387–396 (2018).

18. Ratovelomanana, V. and Linstrumelle, G. Stereoselective Preparation of 1-Chloro-(E,E)-1,3-Dienes. Application to the Synthesis of Methyl Eleostearate. Tetrahedron Lett. 25, 6001–6004 (1984).

19. Bernassau, J. M., Bertranne, M., Collongues, C. & Fetizon, M. Center of mass displacement and relaxation times of linear alkynes. Tetrahedron 41, 3063–3069 (1985).

20. Ariza, X. et al. Preparation of α-labeled aldehydes by base-catalyzed exchange reactions. J. Label. Compd. Radiopharm. 53, 556–558 (2010).

21. Hoffmann, J. S., O'Connor, R. T., Heinzelman, D. C. & Bickford, W. G. A simplified method for the preparation of α- and β-eleostearic acids and a revised spectrophotometric procedure for their determination. J. Am. Oil Chem. Soc. 34, 338–342 (1957).

22. Cao, Y. et al. Re-characterization of three conjugated linolenic acid isomers by GC-MS and NMR. Chem. Phys. Lipids 145, 128–133 (2007).

23. Roschek, B. et al. Peroxyl radical clocks. J. Org. Chem. 71, 3527–3532 (2006).

24. Zielinski, Z. A. M. & Pratt, D. A. Lipid Peroxidation: Kinetics, Mechanisms, and Products. J. Org. Chem. 82, 2817–2825 (2017).

25. Connor, O., Heinzelman, D., Freeman, A. & Pack, F. Spectrophotometric Determination of Alpha-Eleostearic Acid in Freshly Extracted Tung Oil. Ind. Eng. Chem. 17, 467–470 (1945).

26. Chauvin, J. P. R., Griesser, M. & Pratt, D. A. The antioxidant activity of polysulfides: It's radical! Chem. Sci. 10, 4999–5010 (2019).

27. Howard, J. A. & Ingold, K. U. Absolute rate constants for hydrocarbon autoxidation. VI. Alkyl aromatic and olefinic hydrocarbons. Can. J. Chem. 45, 793–802 (1967).

28. Müller, S., Liepold, B., Roth, G. J. & Bestmann, H. J. An Improved One-pot Procedure for the Synthesis of Alkynes from Aldehydes. Synlett 1996, 521–522 (1996).

29. Chatterjee, B. & Gunanathan, C. The ruthenium-catalysed selective synthesis of mono-deuterated terminal alkynes. Chem. Commun. 52, 4509–4512 (2016).

30. Zweifel, G. & Miller, R. L. A Novel Stereoselective Synthesis of 1,3-Dienes from Alkynes via the Addition of Cuprous Chloride to Vinylalanes. J. Am. Chem. Soc. 92, 6678–6679 (1970).

31. Alami, M., Gueugnot, S., Domingues, E. & Linstrumelle, G. An efficient synthesis of 1,3(E),5(Z), 1,3(E),5(E) and 1,3(Z),5(Z)-trienes: Application to the synthesis of galbanolenes and (9Z,11E)-9,11,13-tetradecatrien-1-yl acetate. Tetrahedron 51, 1209–1220 (1995).

32. Willand-Charnley, R., Fisher, T. J., Johnson, B. M. & Dussault, P. H. Pyridine is an organocatalyst for the reductive ozonolysis of alkenes. Org. Lett. 14, 2242–2245 (2012).

33. Curphey, T. J. Preparation of p-toluenesulfonyl azide. A cautionary note. Org. Prep. Proced. Int. 13, 112–115 (1981).

34. Ohira, S. Methanolysis of Dimethyl (1-Diazo-2-oxopropyl)Phosphonate: Generation of Dimethyl (Diazomethyl)Phosphonate and Reaction with Carbonyl Compounds. Synth. Commun. 19, 561–564 (1989).

3.7 Appendix

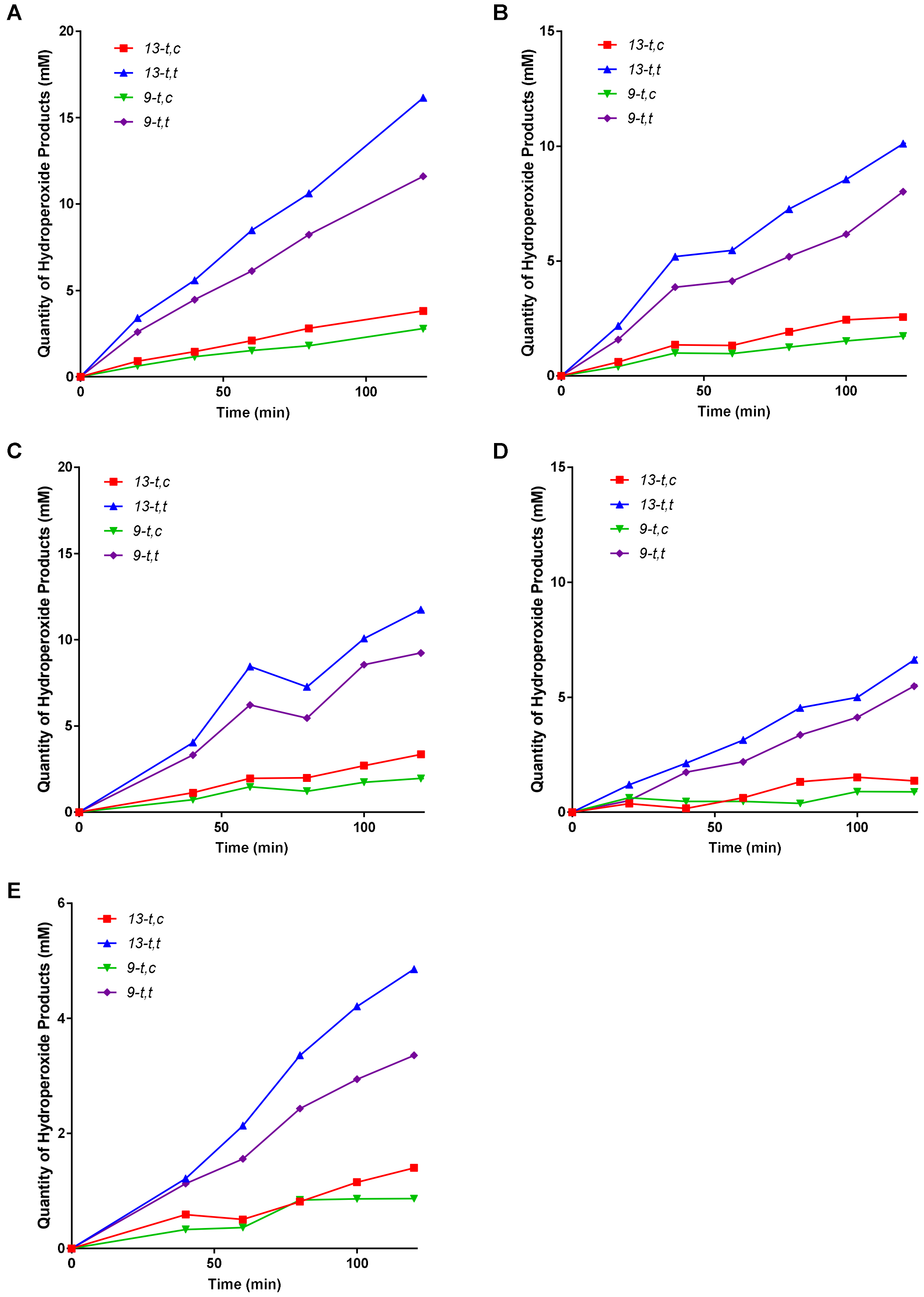

Figure 3.13 Relative quantities of ML hydroperoxide products from α-ESA/ML radical clocking experiment at 0% (**A**), 1% (**B**), 2% (**C**), 5% (**D**), and 10% (**E**) α-ESA. Conditions as described in **Figure 3.5** and in experimental procedure.

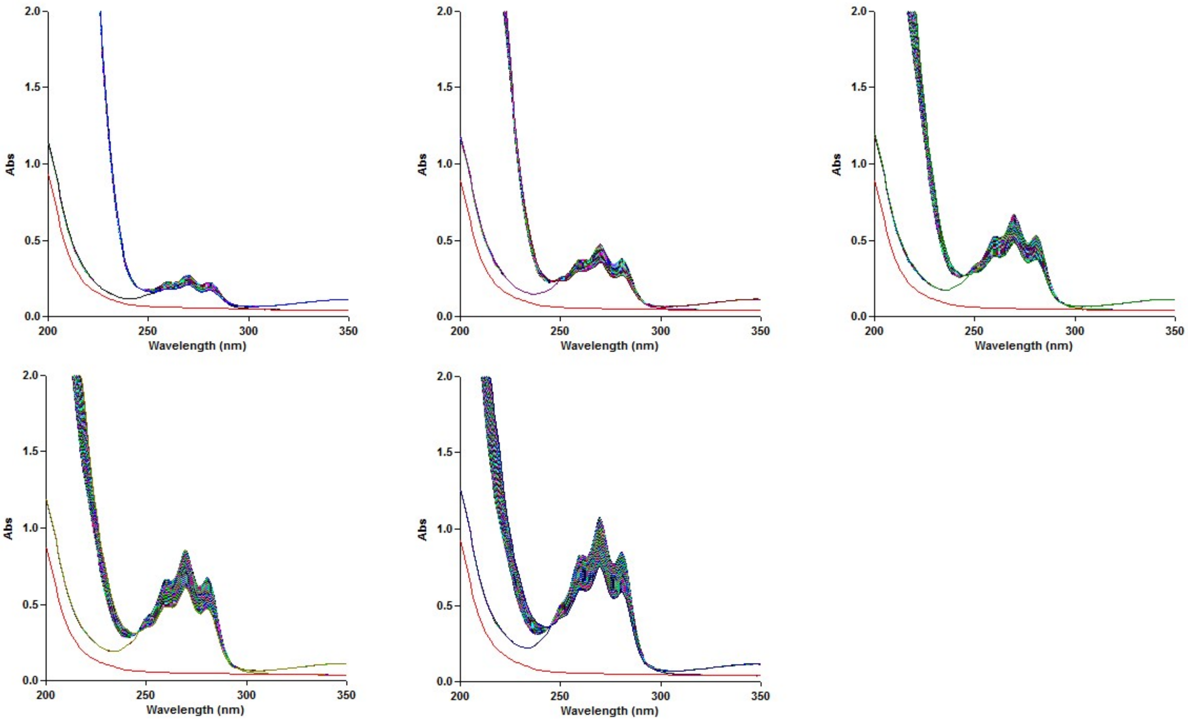

Figure 3.14 Raw data from α-ESA autoxidation in isooctane at 37 ºC, initiated by AIBN, as described in **Figure 3.7** and in experimental. Images depict loss of triene measured over approximately nine hours at [α-ESA] = 4, 8, 12, 16, and 20 μM (left to right).

^{1}H-NMR (400 MHz, $CDCl_3$)

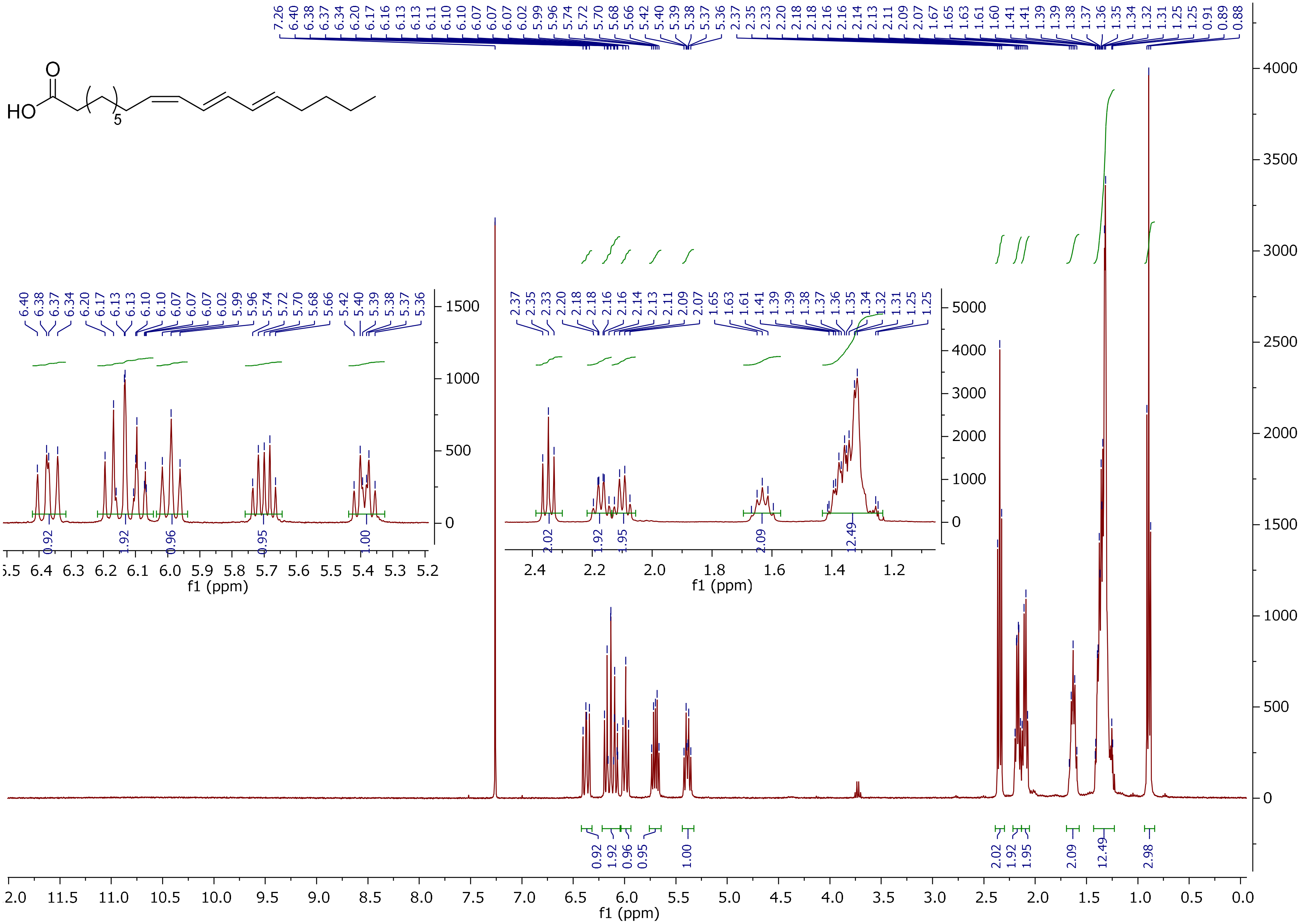

Figure 3.15 ^{1}H-NMR spectrum of α-ESA recrystallized from Tung oil.

^{1}H-NMR (400 MHz, CDCl$_3$)

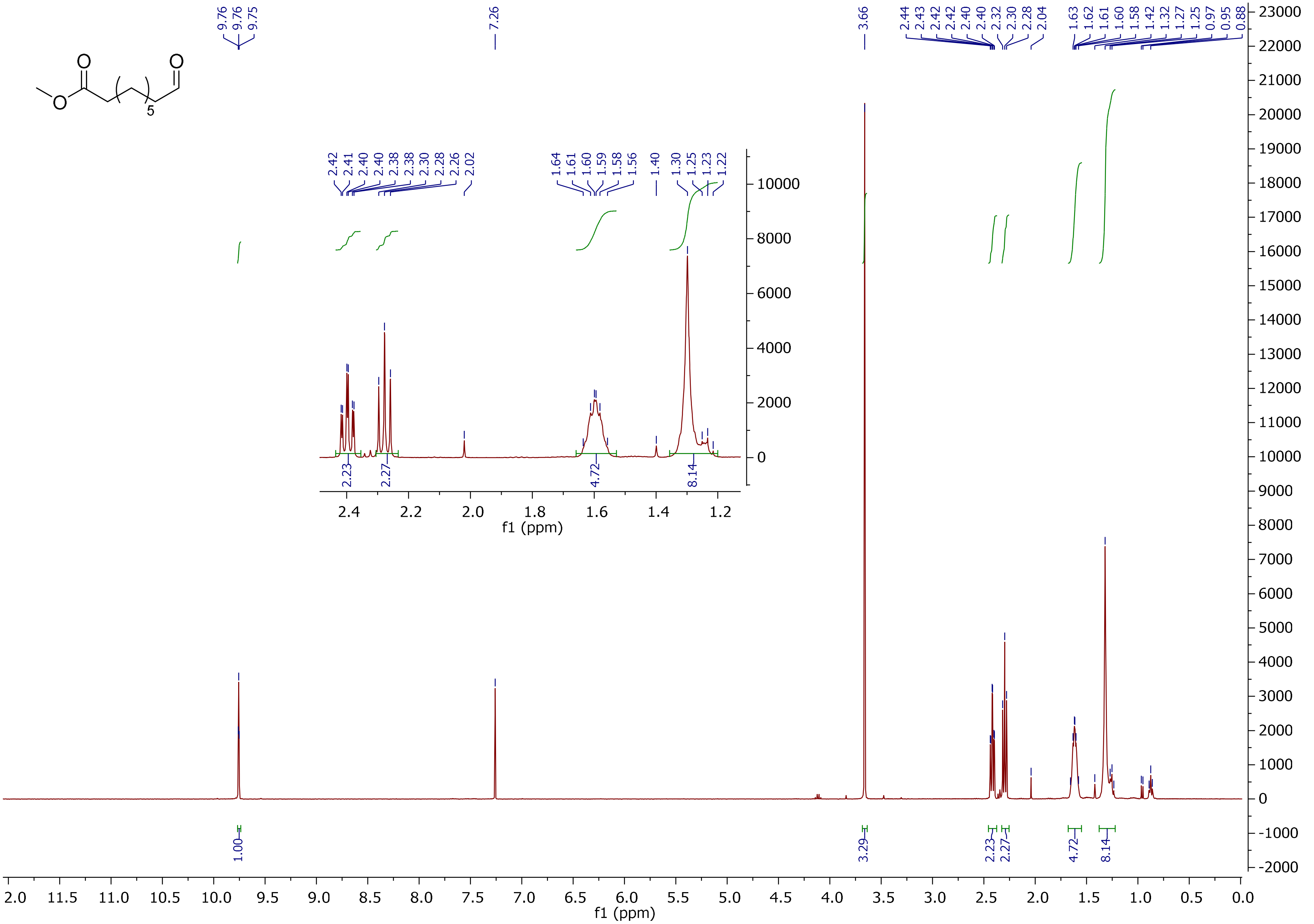

Figure 3.16 ^{1}H-NMR spectrum of methyl 9-oxononanoate.

^{13}C NMR (101 MHz, CDCl$_3$)

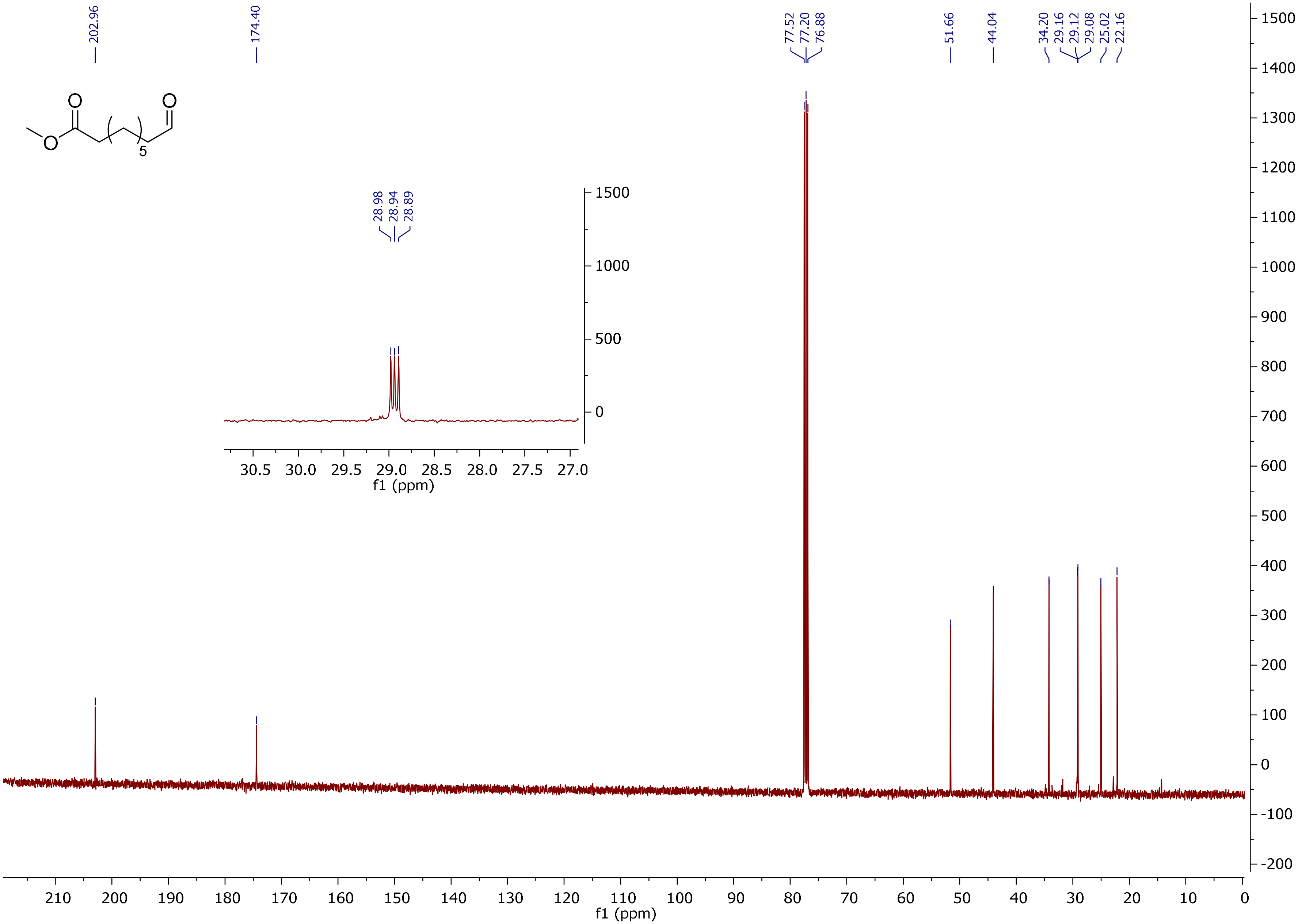

Figure 3.17 ^{13}C-NMR spectrum of methyl 9-oxononanoate.

^{1}H-NMR (400 MHz, $CDCl_3$)

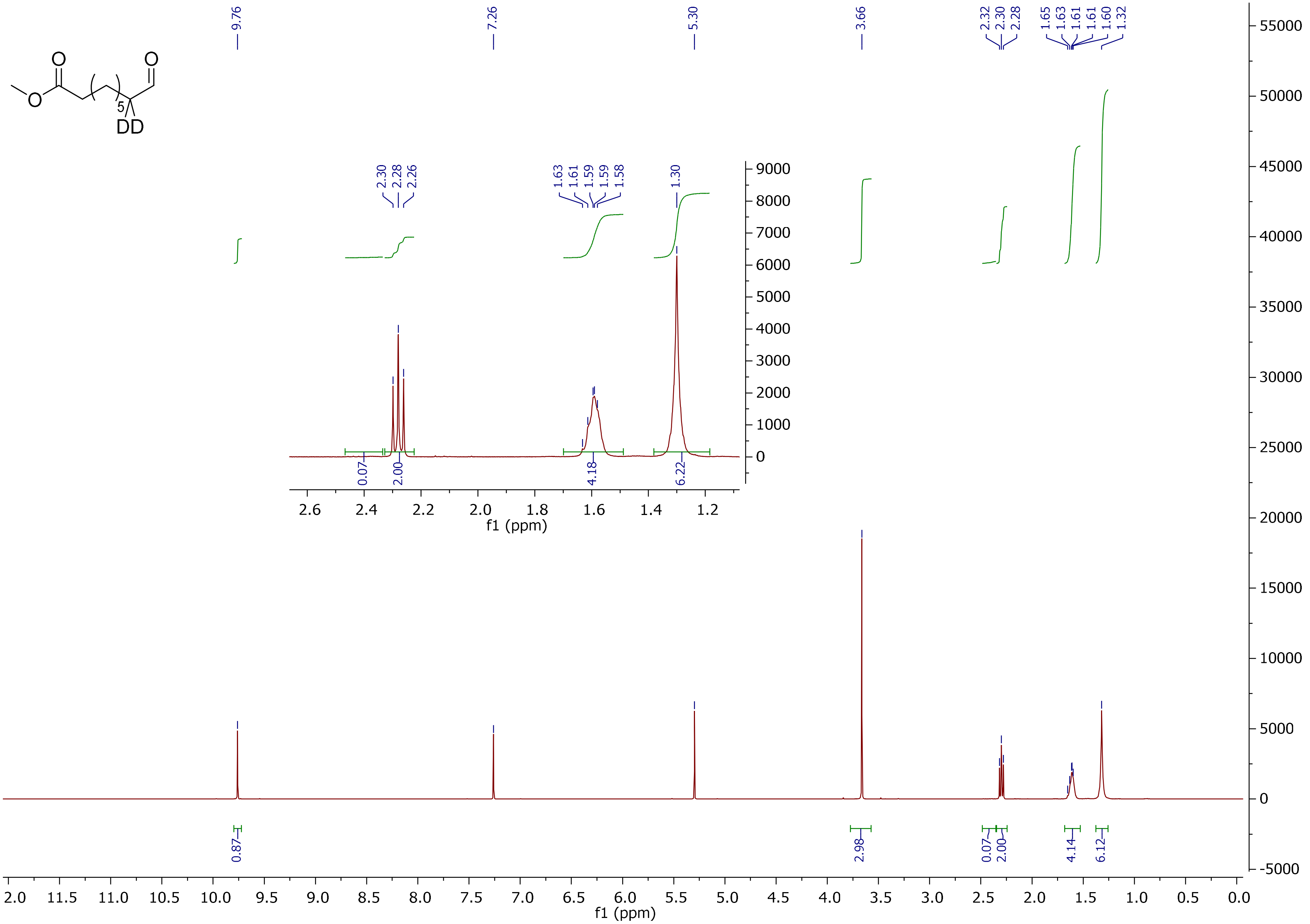

Figure 3.18 ^{1}H-NMR spectrum of 8,8-d_2-methyl-9-oxononanoate.

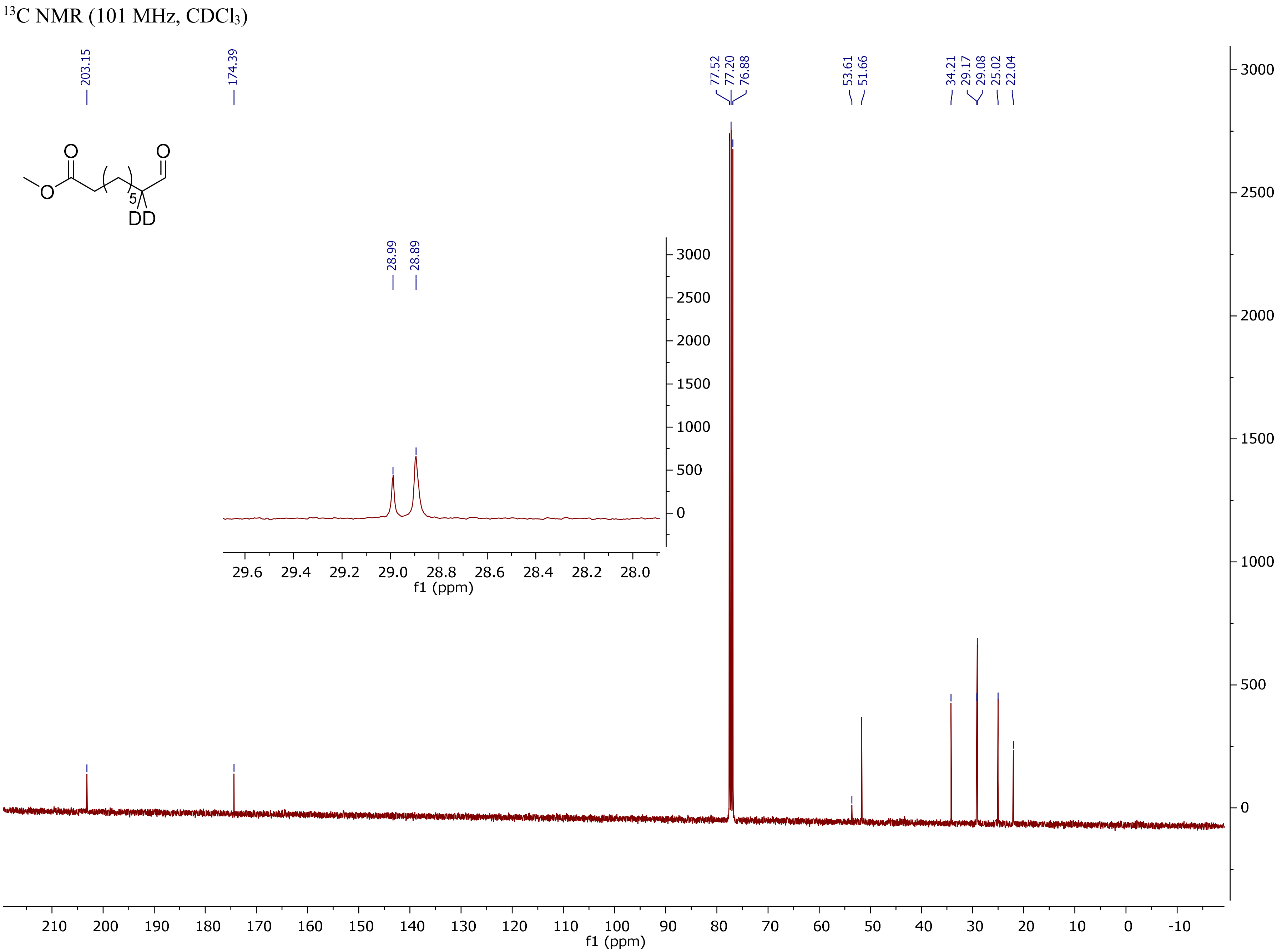

Figure 3.19 ^{13}C-NMR spectrum of 8,8-*d*$_2$-methyl-9-oxononanoate.

^{1}H-NMR (400 MHz, $CDCl_3$)

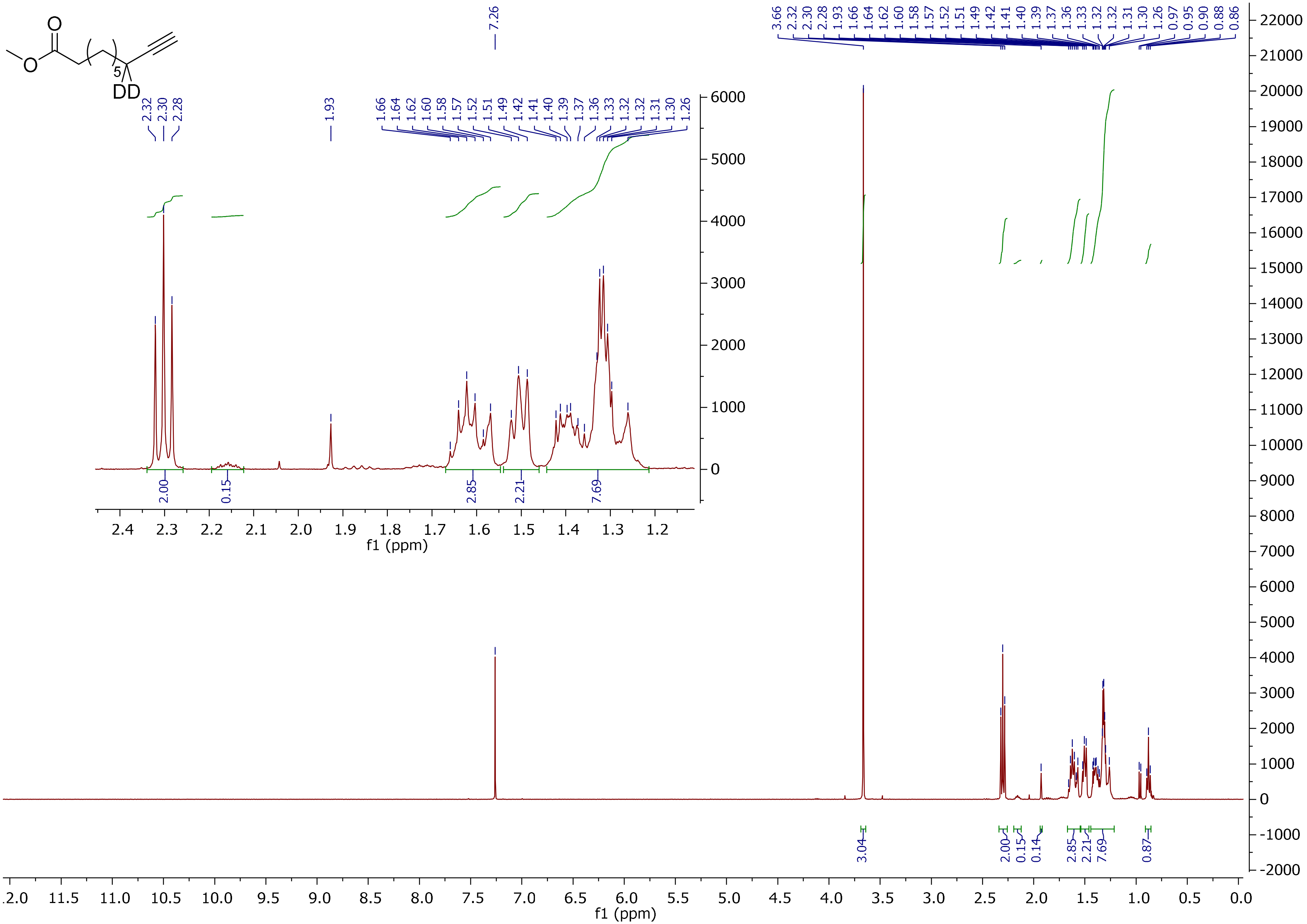

Figure 3.20 ^{1}H-NMR spectrum of 8,8-d_2-methyl-dec-9-ynoate.

^{13}C NMR (101 MHz, $CDCl_3$)

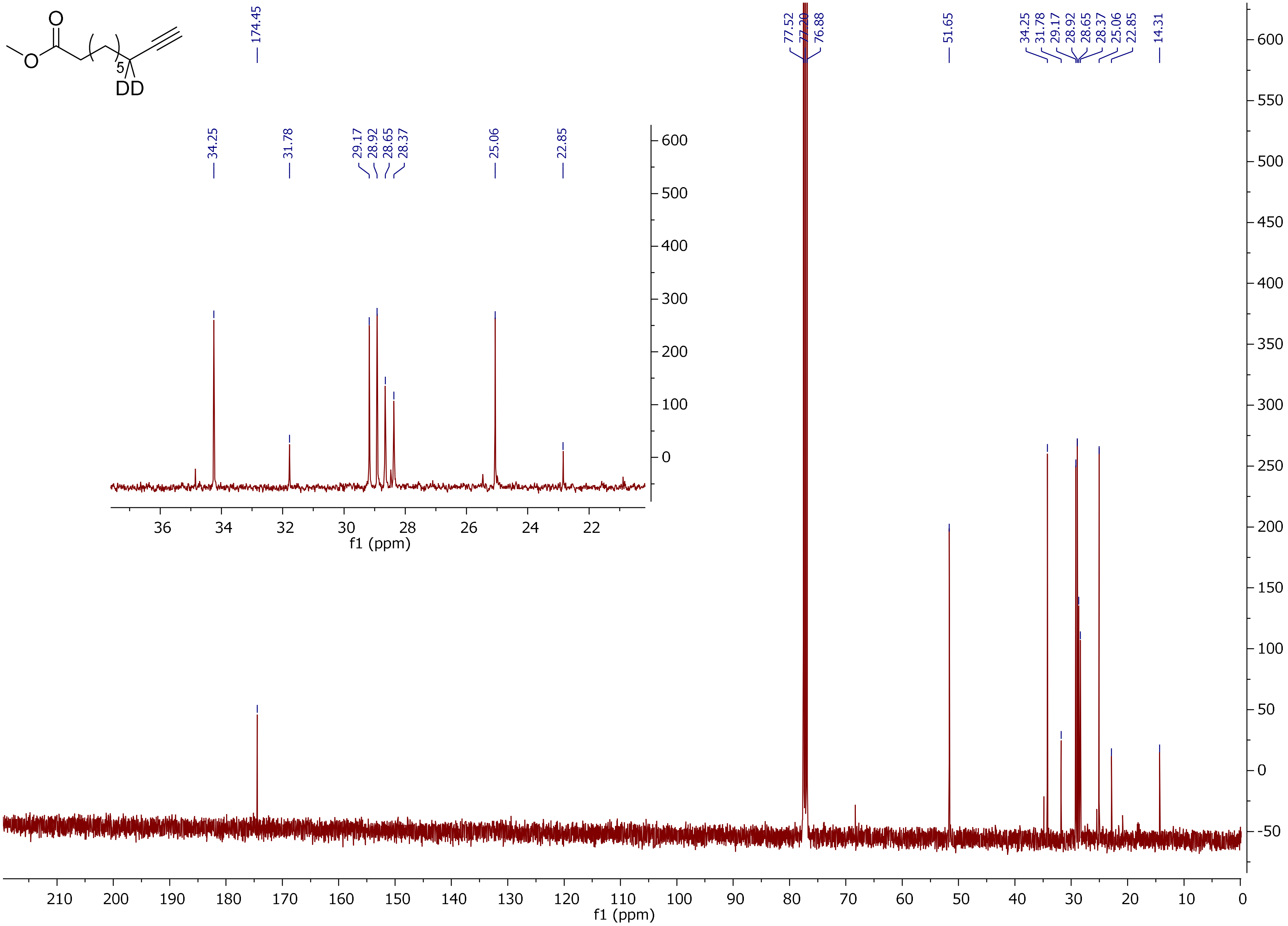

Figure 3.21 ^{13}C-NMR spectrum of 8,8-d_2-methyl-dec-9-ynoate.

^{1}H-NMR (300 MHz, $CDCl_3$)

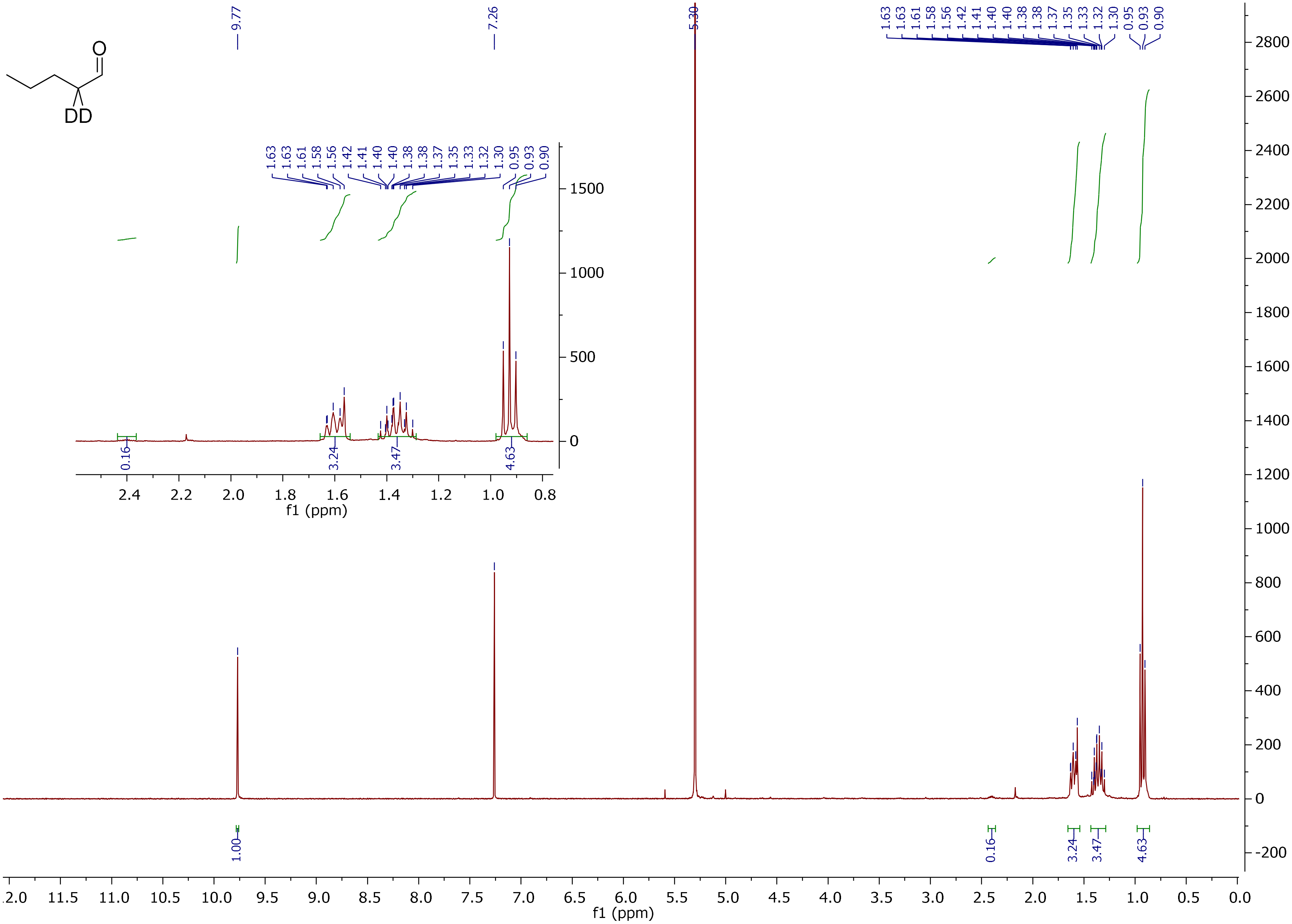

Figure 3.22 ^{1}H-NMR spectrum of 2,2-d_2-pentane.

^{13}C NMR (101 MHz, CDCl$_3$)

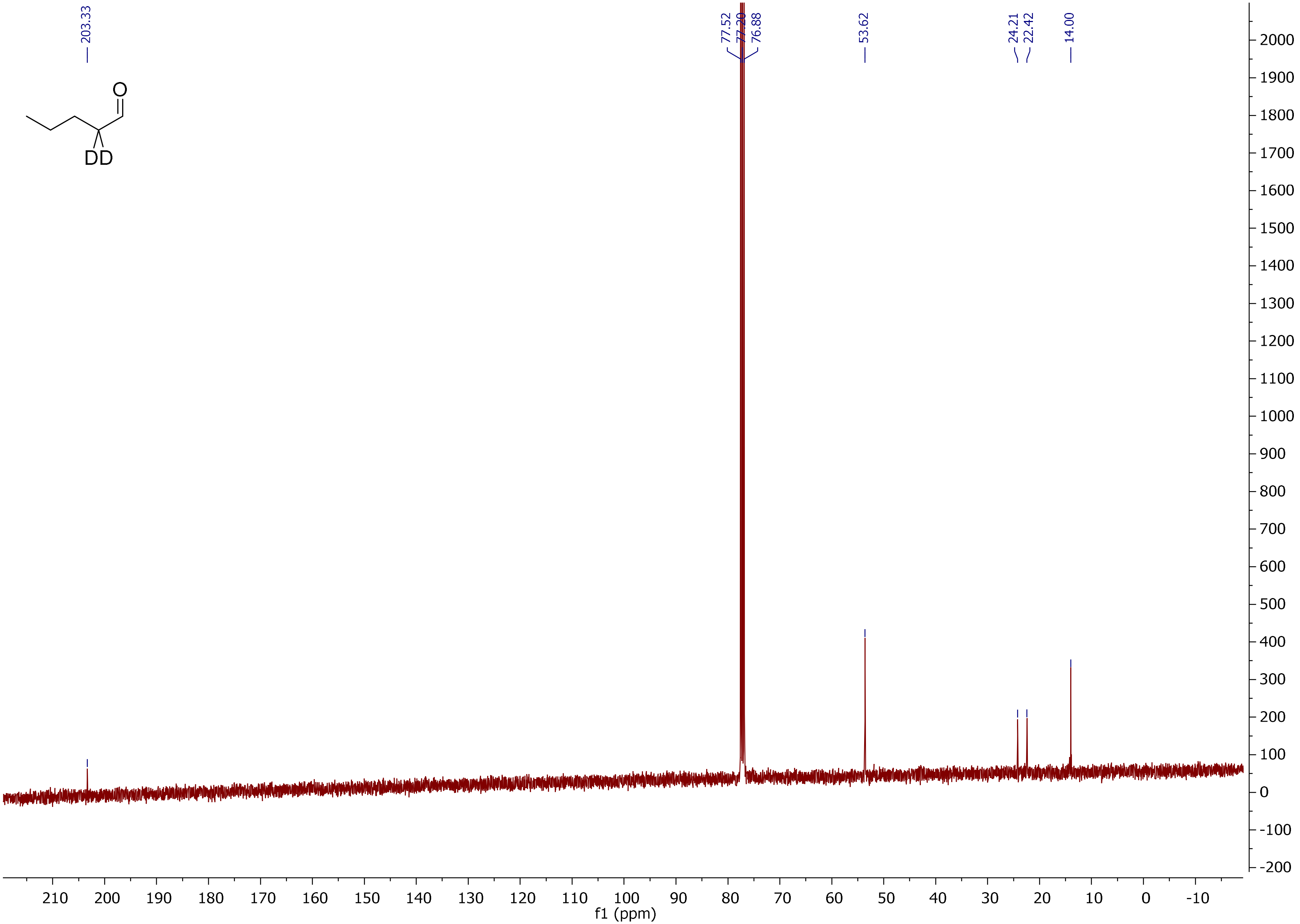

Figure 3.23 ^{13}C-NMR spectrum of 2,2-d_2-pentane.

^{1}H-NMR (400 MHz, CDCl$_3$)

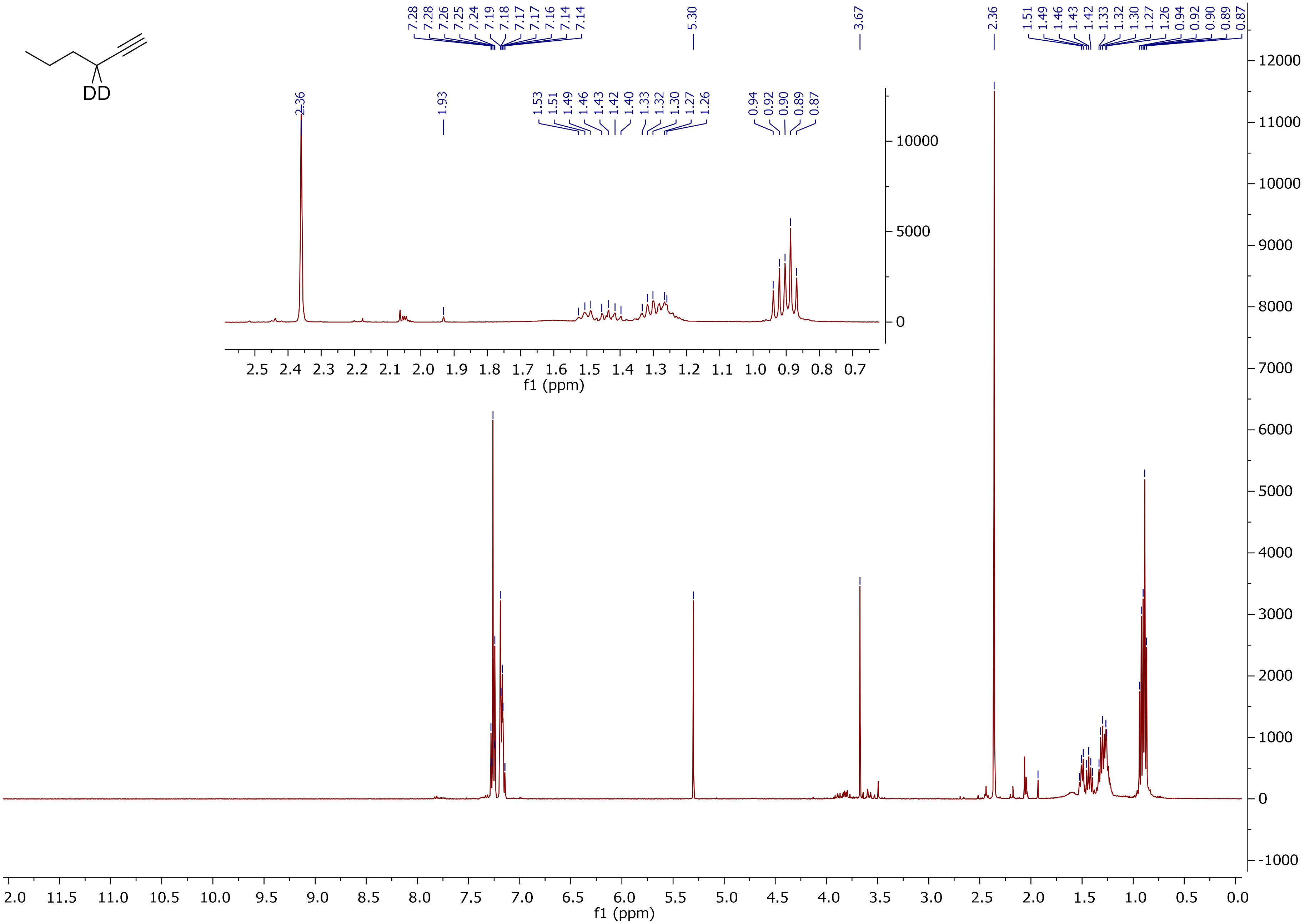

Figure 3.24 ^{1}H-NMR spectrum of 3,3-*d*$_2$-1-hexyne (proposed).